DTIC FILE COPY

(4)

Marine Physical Laboratory

AD-A225 298

MPL's RESEARCH PROGRAM IN NAVY RELATED TECHNOLOGIES

Kenneth M. Watson and Victor C. Anderson
(Principal Investigators)

Final Report to Office of Naval Research Contract N00014-87-C-0127 and N00024-82-C-6400 for the Period 12-01-82 thru 09-28-89

DTIC
ELECTE
JUL 09 1990
S B D

MPL-U-3/90
January 1990

Approved for public release; distribution unlimited.

University of California, San Diego
Scripps Institution of Oceanography

90 07 9 107

Marine Physical Laboratory

MPL's RESEARCH PROGRAM IN NAVY RELATED TECHNOLOGIES

Kenneth M. Watson and Victor C. Anderson
(Principal Investigators)

Final Report to Office of Naval Research Contract N00014-87-C-0127 and N00024-82-C-6400 for the Period 12-01-82 thru 09-28-89

MPL-U-3/90
January 1990

UNCLASSIFIED

SECURITY CLASSIFICATION OF THIS PAGE

REPORT DOCUMENTATION PAGE

Form Approved OMB No. 0704-0188

1a. REPORT SECURITY CLASSIFICATION
UNCLASSIFIED

1b. RESTRICTIVE MARKINGS

2a. SECURITY CLASSIFICATION AUTHORITY

2b. DECLASSIFICATION / DOWNGRADING SCHEDULE

3. DISTRIBUTION / AVAILABILITY OF REPORT
Approved for public release; distribution unlimited.

4. PERFORMING ORGANIZATION REPORT NUMBER(S)
MPL-U-3/90

5. MONITORING ORGANIZATION REPORT NUMBER(S)

6a. NAME OF PERFORMING ORGANIZATION
University of California, San Diego

6b. OFFICE SYMBOL *(If applicable)*
MPL

7a. NAME OF MONITORING ORGANIZATION
Office of Naval Research
Department of the Navy

6c. ADDRESS *(City, State, and ZIP Code)*
Marine Physical Laboratory
Scripps Institution of Oceanography
San Diego, California 92152

7b. ADDRESS *(City, State, and ZIP Code)*
800 North Quincy Street
Arlington, VA 22217-5000

8a. NAME OF FUNDING / SPONSORING ORGANIZATION
Office of Naval Research

8b. OFFICE SYMBOL *(If applicable)*
ONR

9. PROCUREMENT INSTRUMENT IDENTIFICATION NUMBER
N00014-87-C-0127; N00024-82-C-6400

8c. ADDRESS *(City, State, and ZIP Code)*
800 North Quincy Street
Arlington, VA 22217-5000

10. SOURCE OF FUNDING NUMBERS

PROGRAM ELEMENT NO.	PROJECT NO.	TASK NO	WORK UNIT ACCESSION NO.

11. TITLE *(Include Security Classification)*
MPL's RESEARCH PROGRAM IN NAVY RELATED TECHNOLOGIES

12. PERSONAL AUTHOR(S)
Kenneth M. Watson and Victor C. Anderson (Principal Investigators)

13a. TYPE OF REPORT	13b. TIME COVERED	14. DATE OF REPORT *(Year, Month, Day)*	15. PAGE COUNT
final report	FROM _____ TO _____	January 1990	105

16. SUPPLEMENTARY NOTATION

17. COSATI CODES		
FIELD	GROUP	SUB-GROUP

18. SUBJECT TERMS *(Continue on reverse if necessary and identify by block number)*
exploratory research and development, underwater acoustics, signal processing, optics, hydrophone arrays

19. ABSTRACT *(Continue on reverse if necessary and identify by block number)*

Under these contracts, MPL was engaged in a wide variety of Navy related activities which are grouped/categorized as follows:

1. Augmented Exploratory Research and Development: Expansion or acceleration of ongoing efforts, principally in underwater acoustics, signal processing, hydrophone arrays. Also, in optics with the folding in of Visibility Laboratory activities within MPL, enhanced Deep Tow capabilities.
2. Support of Research and Development: FLIP/ORB support, stable platform related issues.
3. Support of MPL Sponsor related needs:

   Operating CNR tower, Equipping of USS DOLPHIN with research gear, Surface Effect Ship (SES), SUBDEVGRP ONE, modifications of existing equipment or equipment orders for MPL or MPL sponsor related needs, i.e., NAVOCEANO, NAVAIR.
4. Special Projects: Quick response MPL support of NAVY mission related needs, meaning use of MPL assets such as Deep Tow to meet unforseen requirements.

20. DISTRIBUTION / AVAILABILITY OF ABSTRACT
☐ UNCLASSIFIED/UNLIMITED ☒ SAME AS RPT. ☐ DTIC USERS

21. ABSTRACT SECURITY CLASSIFICATION
UNCLASSIFIED

22a. NAME OF RESPONSIBLE INDIVIDUAL
K. M. Watson / V. C. Anderson

22b. TELEPHONE *(Include Area Code)*
(619) 534-1802

22c. OFFICE SYMBOL
MPL

DD Form 1473, JUN 86 *Previous editions are obsolete*

SECURITY CLASSIFICATION OF THIS PAGE
UNCLASSIFIED

19. Abstract (continued)

5 Exploratory and Advisory: Directly funded participation of MPL scientific, engineering, and other personnel in various Navy panels and committees, etc. This is for participation beyond the normal Ex&Ad in connection with the overall MPL program.

These activities are within the framework of our Navy mission which is:

To investigate and apply knowledge about the ocean, its boundaries and their surrounding media to the solution of the Navy's problems in anti-submarine and pro-submarine warfare;

To provide research training of students in areas of oceanography and ocean technology which have application to Navy requirements.

To maintain certain special ocean engineering, research and develop- ment capabilities which are essential to the Navy.

Categories 1 and 2 are the most important from the standpoint of developing the research skills and facilities with which to pursue research goals within the context of the University and our Navy mission. Capabilities developed as a result of the above have led to many instances of being asked by the Navy for quick response efforts which are in Categories 3 and 5. Similarly, the skills and experience acquired as a result of activities in Categories 1 and 2 lead to requests by the Navy to serve on panels, committees on a sustained, funded basis; that is Category 5, which is above and beyond our usual Exploratory and Advisory activities.

Accession For	
NTIS GRA&I	☑
DTIC TAB	☐
Unannounced	☐
Justification	
By	
Distribution/	
Availability Codes	
Dist	Avail and/or Special
A-1	

TABLE OF CONTENTS

MPL's Research Program in Navy Related Technologies

Final Report to
Office of Naval Research
Contract N00014-87-C-C127
and N00024-82-C-6400
For the Period
12-01-82 - 09-28-89

Kenneth M. Watson and Victor C. Anderson
(Principal Investigators)

INTRODUCTION

Under these contracts, MPL was engaged in a wide variety of Navy related activities which are grouped/categorized as follows:

1. Augmented Exploratory Research and Development: Expansion or acceleration of ongoing efforts, principally in underwater acoustics, signal processing, hydrophone arrays. Also, in optics with the folding of Visibility Laboratory, activities within MPL, enhanced Deep Tow capabilities,

2. Support of Research and Development: FLIP/ORB support and stable platform related issues,

3. Support of MPL Sponsor related needs:

   Operating CNR tower, Equipping of USS DOLPHIN with research gear, Surface Effect Ship (SES), SUBDEVGRPONE, modifications of existing equipment or equipment orders for MPL or MPL sponsor related needs (i.e., NAVOCEANO, NAVAIR).

4. Special Projects: Quick response MPL support of NAVY mission related needs. This would be utilizing MPL assets such as Deep Tow to meet unforseen requirements.

5. Exploratory and Advisory: Directly funded participation of MPL scientific, engineering, and other personnel in various Navy panels and committees, etc. This is for participation beyond the normal Exploratory and Advisory in connection with the overall MPL program.

These activities are within the framework of our Navy mission which is:

To investigate and apply knowledge about the ocean, its boundaries and their surrounding media to the solution of the Navy's problems in anti-submarine and pro-submarine warfare;

To provide research training of students in areas of oceanography and ocean technology which have application to Navy requirements.

To maintain certain special ocean engineering, research and development capabilities which are essential to the Navy.

Categories 1 and 2 are the most important from the standpoint of developing the research skills and facilities with which to pursue research goals within the context of the University and our Navy mission. Capabilities developed as a result of the above have led to many instances of being asked by the Navy for quick response efforts which are in Categories 3 and 5. Similarly, the skills and experience acquired as a result of activities in Categories 1 and 2 led to requests by the Navy to serve on panels and committees on a sustained, funded basis; that is Category 5, which is above and beyond our usual Exploratory and Advisory activities.

SUMMARY OF ACTIVITIES

A brief description of these activities is included below along with a detailed program summary listing by categories. A bibliography of reports regarding these activities is also included in Appendix A:

Category 1

It is appropriate to summarize activities where there is a common thread.

One of MPL's major research efforts directly related to our mission is in the area of understanding and exploiting ambient noise and sound propagation in the ocean. The work of Hodgkiss, Hildebrand and Fisher was concerned with the development and deployment of hydrophone arrays, and water column measurements of ambient noise and signals in various experiments. This included joint experiments with various Navy Centers, NRL and NORDA, as well as contractors. Dr. Hodgkiss's work with signal processing and array processing is directly related to this area. At lower frequencies, the work of Drs. Anderson, Webb, Dorman, Hildebrand and Hodgkiss made use of different sensors that are bottom mounted to study ambient noise and sound propagation.

For acoustic measurements in the water column, two major experiments were successfully completed in which unique new measurements of the vertical directionality of the ambient noise field were made from FLIP: one, a study of the effect of distance from coastal shipping and local wind on the vertical distribution of ambient noise in the 75-300 Hz region (Broadband CUARP); and, two, the first high resolution measurements of the vertical directionality of signal and noise in the 50-200 Hz region (ONT High Gain Initiative SVLA experiment). A third major effort in this area was preparation for the DVLA experiment which was a follow-on to the SVLA experiment. Whereas the SVLA experiment made use of a 900 meter vertical array originally designed for horizontal deployment, its center frequency was 100 Hz, too high for the goals of the DVLA experiment scheduled for July, 1989. Construction of a 3000 meter, 200 element (50 Hz) vertical array was completed in time for the DVLA experiment and it was successfully operated for the duration of the experiment. The 900 and 3000 meter arrays produce 12 bit digital data from each hydrophone and make use of acoustic navigation for array element location to make beamforming and matched field processing possible.

In conjunction with the above efforts, freely drifting Swallow float arrays with 3 axis geophones were deployed by Dr. Hodgkiss to obtain ambient noise and

signal data uncontaminated by flow noise to compare with data obtained with arrays deployed from FLIP. The Swallow floats have also been the key assets in pursuing Slack Line array concepts, sea-floor measurements, and led to the need for an acoustic modem so that data at a high rate (9600 baud) can be transmitted to a surface vessel from various Swallow float arrays. These Swallow floats can be deployed in vertical or horizontal configurations and have an array element location capability built into them so data from them can be used in post-cruise beamforming.

Array research with the MPL 200 meter array was concerned with the vertical distribution of ambient noise in the 100-400 Hz region and received support from NAVAIR in conjunction with the Broadband CUARP.

In all the above research, data processing and analysis are a key to monitoring experiments in progress and interpreting the results. MPL has been involved with developing the computer and recording systems for our own research and, in so doing, we have also been tasked to build high speed data acquisition systems for other uses by our sponsors, notably the ACSAS system, as well as applying the dynamic beamformer (built for the STRAPP experiment) to towed arrays.

Doppler sonars mounted on FLIP were used by R. Pinkel to study upper ocean dynamics in about a cubic kilometer. These sonars have been used to measure currents down to 1 cm/sec relative to FLIP and have revealed Langmuir cells, and surface slope distributions in addition to delineating internal waves and directions of energy flux.

Multispectral imaging of the marginal ice zone and whole sky imaging with respect to cloud cover (E/O System 5 units) are parts of an overall program to build a database from which R. Johnson and his colleagues can implement autonomous pattern recognition algorithms for quantitative remote sensing of cloud cover and visibility.[1]

[1] Upon dissolution of the Visibility Laboratory of the Scripps Institution of Oceanography, a part of the "Whole Sky Imagery" program (Richard Johnson/Principal Investigator) came under the Marine Physical Laboratory.

Category 2

Facilities support for FLIP and ORB (6.5) from NAVSEA 05R12 includes support for personnel crewing these platforms and regular maintenance and inspection such as periodic drydocking. For example, with respect to FLIP, whereas it was originally designed for a twenty-year life based on marine corrosion allowances, excellent corrosion protection has allowed us to continue operating FLIP with a more intense maintenance program with respect to monitoring fatigue cracking. Strain gage recordings during sea operations and towing provide a quantitative measurement of stress cycling. After the equivalent of a normal years exposure to cyclic stresses, FLIP is drydocked for inspection and maintenance. These platforms have been used in a wide variety of tasks, mostly generated within MPL; several outside users have also used these platforms on mostly Navy related programs.

Results of a workshop conducted by MPL led to studies of advanced research platforms, including a larger, more capable version of FLIP and the conversion of an existing large offshore oil exploration semi-submersible platform for multi-disciplinary research programs. The new FLIP has been proposed for FY-92 support, and the semisubmersible has been acquired by the Department of Defense for use in the drug enforcement program, with opportunities for research support.

Category 3

In this category is included a wide range of activities in which MPL has participated directly in supporting Navy needs or has acted as cognizant monitor of various Navy projects within Navy activities or at contractor companies.

Several tasks were assigned to MPL under this contract in order to make special talents and capabilities at MPL available to Navy sponsors, particularly with regard to advanced capability platforms. These included the successful rehabilitation and operation of an offshore oceanographic research tower for the Chief of Naval Research, until it was destroyed in a major storm in January 1988. The research submarine USS DOLPHIN (AGSS-555) was equipped with two major research systems, one involving an off-board acoustic and optical sensor system and the other involving the installation of a precision photo-optical system for seafloor investigations. Also included in this category were a number of tasks devoted to increasing the capability of Navy deep submergence assets to support research and survey programs, both at Submarine Development Group ONE and at the Naval Oceanographic Command. Investigations of advanced capability platforms included studies of the producibility of high-technology surface effect ships under contracts with several major shipyards (SES Hullform), and tests and evaluation of a new closed-cycle-diesel propelled submarine for potential diver lock-out capability.

Category 4: Quick Response

The loss of a high priority space vehicle initiated an urgent Navy request for MPL to conduct a prompt and detailed search of a seafloor area in the East Pacific Ocean. This was accomplished using SEABEAM sonar survey data to delineate the most probable search areas for MPL's Deep Tow instrument system, and for the coordinated search by Navy deep submergence assets.

Several times in the past, urgent Navy needs have required the services of MPL in operations at sea. During the period of this contract, F. Spiess and P. Lonsdale participated in sea-floor search activities with the MPL Deep Tow system.

Category 5: Exploratory and Advisory

Normally, MPL principal investigators participate in various workshops and advisory panels as part of their regular activities. For sustained efforts along these lines, particularly when a lot of travel is involved, funding in this category is provided.

CONTRACT PROGRAM SUMMARY

TABLE I

Category 1: Augmented Exploratory Research and Development (Array Deployments, Deep Tow Research)

Date of Modification	Sponsor	Program Title	Principal Investigator
Mod 00	NAVSEA 63D	Appl. of Dynamic Beamf. to Towed Line Arrays	Hodgkiss
Mod 01	NAVSEA63R	(VIM) Vibration Isolation Module	Andrews
Mod 03	NAVSEA63R14	Adaptive Signal Processing	Hodgkiss
Mod 04	NAVSEA63R	Reverberation Dynamics	Hodgkiss
Mod 04	NAVSEA63R	(VIM) Vibration Isolation Module	Andrews
Mod 05	NAVSEA63D1	Appl. Dynamic Beamforming to Towed Line Arrays	Hodgkiss
Mod 05	NAVSEA63R	Vibration Isolation Module	Andrews
Mod 05	NOSC 7213	Active Acoustic Cancellation	Abarbanel
Mod 07	NAVSEA63R14	Adaptive Array Processing	Hodgkiss
Mod 07	NAVSEA63R12	Devel. & Eval. Vibration Isolation Module	Andrews
Mod 08	NAVSEA63R12	Devel. & Eval. Vibration Isolation Module	Andrews
Mod 13	NOSC743	Intelligent Beamformer	Hodgkis
Mod 13	NOSC512	Range-extended Sonar Targets	Altes
Mod 13	NOSC541	SEA SNAKE Surveillance System	Hodgkiss
Mod 14	PMS395	Modularized Towed Deep Sea Vehicle	Spiess
Mod 16	ONR112	Marginal Ice Zone Investigations	Maynard
Mod 19	NAVAIR	Ambient Noise Vert. Directionality	Hodgkiss
Mod 19	ONR112	Spectral-Properties at Marginal Ice Zones	Maynard
Mod 19	NOSC522	Planktonic Growth on Ph Seawater	Dickson
Mod 19	NAVAIR633	Vertical Correlation Measurements	Fisher
Mod 23	ONR112	Spec. Properties Marginal Ice Zones	Maynard
Mod 28	NAVAIR633	Vertical Correlation Measurements	Fisher
Mod 30	ONR/AF	Multi-Station WSI Stations	Johnson
Mod 30	NOSC	SEA SNAKE Surveillance	Hodgkiss
Mod 30	NUSC	VLF Acoustic Experiment	Hodgkiss
Mod 31	ONT	High Gain, High Resolution Program	Fisher/Hildebrand
Mod 32	ONR/AF	Multi-Station WSI Network	Johnson
Mod 32	NOSC	SEA SNAKE Surveillance	Hodgkiss
Mod 32	NOSC	Reverberation Simulation	Hodgkiss
Mod 32	ONR/AF	Multi-Station WSI Station	Johnson
Mod 32	NOSC	SEA SNAKE Surveillance	Hodgkiss
Mod 33	NUSC	Parametric Sonar Support	Hodgkiss
Mod 33	NOSC634	Effects of Monomolecular Films	Anderson

Date of Modification	Sponsor	Program Title	Principal Investigator
Mod 35	ONT/Booth	Vertical Line Array Measurements of Ambient Noise	Fisher/Hodgkiss
Mod 35	ONR	Upper Ocean Effects	Pinkel
Mod 35	ONT/NRL	Program in Marine Physics	Watson
Mod 36	ONR/NRL	Program in Marine Physics	Watson
Mod 36	ONT/Booth	MPL Digital Array Design Studies	Hildebrand/Fisher
Mod 37	ONT/Booth	MPL Digital Acoustic Array for the DVLA Experiment	Hildebrand/Fisher
Mod 38	ONR/NRL	Program in Marine Physics	Watson
Mod 38	White Sands	E/O System 5 Camera Spare Parts	Johnson
Mod 39	ONR	Upper Ocean Effects	Pinkel
Mod 39	NRL/SPAWAR	Certical Sea Test	Fisher/Hodgkiss
Mod 41	ONT/NRL	Program in Marine Physics	Watson
Mod 41	AF	E/O System 5	Johnson
Mod 42	DARPA	ACSAS Program	Hodgkiss
Mod 42	Army	E/O System 5	Johnson
Mod 43	ONR/SDI	E/O System 5	Johnson
Mod 45	ONT/230	Vertical Array-Hi Gain	Hildebrand/Fisher
Mod 45	ONT/230	Vertical Array Data Analysis	Hodgkiss/Hildebrand
Mod 46	SDI/Army	E/O Sys5 Unit #3	Johnson
Mod 46	SDI/Army	Night-Time Prototype	Johnson
Mod 48	ONT	Array Analysis	Hodgkiss

TABLE II

Category 2: Support of Research & Development - Facilities Support

Date of Modification	Sponsor	Program Title	Principal Investigator
Mod 02	NAVSEA05R	R/P FLIP and ORB	Bishop
Mod 04	NAVSEA05R	R/P FLIP and ORB	Bishop
Mod 07	NAVSEA05R	R/P FLIP and ORB	Bishop
Mod 10	NNAVSEA05R12	R/P FLIP & ORB Support	Bishop
Mod 24	NAVSEA05R	R/P FLIP and ORB	Bishop
Mod 35	NAVSEA05R	R/P FLIP and ORB	Bishop
Mod 42	NAVSEA05R	ORB Thruster	Beck
Mod 46	NAVSEA05R	FLIP/ORB Support	Beck
Mod 48	NAVSEA05N	FLIP/ORB	Beck

TABLE III

Category 3: Various MPL Sponsor Research Activities

Date of Modification	Sponsor	Program Title	Principal Investigator
Mod 03	NAVOCEANO	Crane Support	Bishop
Mod 05,08, 13	PMS395	Techn. Support for USN Deep Subm. Systems	Bishop
Mod 05	NAVOCEANO	Techn. Support for USN Deep Subm. Tow	Boegeman
Mod 05	NAVOCEANO	Transmissometer Repair & Maintenance	Edwards
Mod 05	NOSC1603	ACSASS Calibration & Analysis Support	Vislab/Austin
Mod 06	NAVOCEANO	Slack Tensions Inspection/Repair	Bishop
Mod 09	NOSC943	Sample Recovery Basket	Bishop
Mod 09	NOSC844	NOSC Radiometric Facility	Austin
Mod 10	NAVAIR	Pacific Bathymetry	Spiess
Mod 13, 16, 25	NAVSEA05R12	Wide-Area Imaging System	Bishop/Ballard
Mod 14	NAVO7210	Multi-Spectral Optical Probe	Austin
Mod 14	NAVO7111	Transmissometer Modifications	Austin
Mod 19	NAVSEA0133	Passive Sonar Improvements	Maynard
Mod 19, 32, 35, 48	PMS395	Eval. Acoustic & Optical Sensor Systems	Bishop
Mod 19	NOSC641	Support for USS DOLPHIN	Bishop
Mod 19	PMS395	Seacliff Support	Bishop/Ballard
Mod 26	NAVSEA05R12	Uplooking Imaging System (Seacliff)	Bishop/Ballard
Mod 27	NAVOCEANO7111	Repair & Modification of Transmissometer	Edwards
Mod 29	NAVSEA05R	SES Hullform Technology	Bishop
Mod 30	NAVOCEANO	Camera Spares-NAVOCEANO	Johnson
Mod 31, 32	NWC	NWC Use of Tower	Bishop
Mod 33	NAVSEA05R47	Floating Platform Study	Bishop/Fisher
Mod 33	NAVSEA05R47	SES Supplment	Bishop
Mod 33	NAVAIR933	Broadband 88 (Sonobuoys)	Fisher
Mod 33	NOSC/NRL	Undersea Equipment Support	Watson
Mod 34	NAVOCEANO	MERT Support	Austin
Mod 34	ONR1112D	Tower Support	Bishop

TABLE III (cont)

Category 3a: Various MPL Sponsor Research Activities

Date of Modification	Sponsor	Program Title	Principal Investigator
Mod 35, 40. 48	PMS395	Evaluation of Diver-Lockout Subm.	Bishop
Mod 35	PMS395	Eval. of Acoust. & Optical Sensor Systm.	Bishop
Mod 36	NAVOCEANO	Deep Towed Vehicle Cable Tensioning System	Bishop
Mod 38	PMS395	Wide-Area Wide Area Imaging System	Bishop
Mod 38	NAVOCEANO	MERT Calibration	Nolten
Mod 39	NADC	Mod of AN/SSQ-538 Sonobuoys	Fisher
Mod 40	ONR1112D	Tower Add On-Saxon	Watson
Mod 40	PMS395	Wide-Area Wide Imaging System	Watson
Mod 43	NOSC	FLIP Use	Beck
Mod 44	ONR/PMS395	AOS-Hydroproducts	Bishop
Mod 44	DARPA	CM/CCM	Anderson
Mod 45	ONR/112D	Saxon Support	Beck
Mod 46	NAVSEA/DTRC	SCAT Prototype Comp.	Beck
Mod 48	DARPA	CM/CCM	Anderson
Mod 48	NADC	Mod of AN/SSQ Sonobuoy	Fisher
Mod 48	DTRC	SCAT Prototype Com.	Beck
Mod 48	PMS385	AOS Evaluation	Bishop
Mod 48	NEL	AOS Evaluation	Bishop
Mod 49	NADC	Mod. of AN/SSQ Sonobuoys	Fisher
Mod 49	DARPA	SCAT	Beck
Mod 50	NAVSEA	SCAT	Beck
Mod 51	NAVOCEANO	MERT Calibration/Software	Nolten
Mod 51	NAVOCEANO	Diver Lockout	Bishop

TABLE IV

Category 4: MPL Quick Response Special Projects

Date of Modification	Sponsor	Program Title	Principal Investigator
Mod 10	NAVSEA00c	Seafloor Search & Survey	Lonsdale/Spiess
Mod 13	NAVSEA00c	Seafloor Search & Survey	Lonsdale/Spiess
Mod 15	NAVSEA00c	Seafloor Search & Survey	Lonsdale/Spiess
Mod 17	NAVSEA00C	Seafloor Search & Survey	Lonsdale/Spiess
Mod 18	NAVSEA00c	Seafloor Search & Survey	Lonsdale/Spiess

TABLE V

Category 5: Exploratory & Advisory

Date of Modification	Sponsor	Program Title	Principal Investigator
Mod 04	NAVSEA63R	MOST Support	Anderson
Mod 04	NOSC	Design Study - Night-time K System	Vislab/Austin
Mod 05	NAVSEA63R	Expl. & Dev. Undersea Warefare Techn. Contrib. Study	Andrews
Mod 33	DARPA	Mid-Frequency Array Study	Anderson
Mod 36	NOSC	FDS Review Panel	Hodgkiss
Mod 38	DARPA	Very Large Mid-Frequency Array	Anderson
Mod 51	NORDA	Deep Tow Consult/Shop Services	Spiess

APPENDIX A

Bibliography

BIBLIOGRAPHY

Final Report to
Office of Naval Research
Contract N00014-87-C-0127
and
N00014-82-C-6400

Abstracts

1. P. Lonsdale, "Kula plate not kula," EOS, Trans. Amer. Geophys. Union **67**, 1199 (1986).

2. B. J. Sotirin, "In-situ acoustic calibration for a large aperture array," J. Acoust. Soc. Am. **84**, S17 (1988).

3. G. L. D'Spain and W. S. Hodgkiss, "Energetics of the infrasonic ambient ocean sound field," EOS, Trans. Am. Geophys. Union (submitted).

4. B. J. Sotirin, "Acoustic navigation for a large aperture array," J. Acoust. Soc. Am. **86**, S89 (1989).

5. B. J. Sotirin and W. S. Hodgkiss, "Vertical directionality of low frequency wind-induced noise," J. Acoust. Soc. Am. **86**, S117 (1989).

Journals

1. W. S. Hodgkiss and D. Alexandrou, "Applications of adaptive array processing," in *Adaptive Methods in Underwater Acoustics*, edited by Heintz G. Urban (NATO Advanced Study Institute (Boston: D. Reidel, 1985), Luneburg, Germany, 1984), pp. 447-460.

2. W. S. Hodgkiss and D. Alexandrou, "Under-ice reverberation rejection," IEEE Intl. Conf. on Acoust., Speech, Signal Process., 823-825 (1985).

3. W. S. Hodgkiss and D. Alexandrou, "An adaptive algorithm for array processing," IEEE Trans. Ant. Prop. **AP-34**, 454-458 (1986).

4. Dimitri Alexandrou, "Boundary reverberation rejection via constrained adaptive beamforming," J. Acoust. Soc. Am. **82**, 1274-1290 (1987).

5. D. Alexandrou, "Signal recovery in a reverberation-limited environment," IEEE J. Ocean. Engr. **OE-12** (1987).

6. R. W. Johnson and W. S. Hering, "Automated cloud cover measurements with a solid-state imaging system," Proceedings of the Fifth Tri-Service Clouds Modeling Workshop (1987).

7. W. S. Hodgkiss, "Source ship contamination removal in a broadband vertical array experiment," Oceans '88, 310-314 (1988).

8. W. S. Hodgkiss and F. H. Fisher, "Vertical directionality of ambient noise at 32°N as a function of longitude and wind speed," in *Underwater Acoustic Data Processing*, edited by Y. T. Chan ((Kluwer Publishers, 1989), Kingston, Canada, (1988), 1989), pp. 99-104. Proceedings of the NATO Advanced Study Institute on Underwater Acoustic and Data Processing

9. B. J. Sotirin and J. A. Hildebrand, "Large aperture digital acoustic array," J. Ocean Eng. (in press).

10. B. J. Sotirin and J. A. Hildebrand, "Acoustic navigation of a large aperture array," J. Acoust. Soc. Am. (in press).

11. W. S. Hodgkiss and V. C. Anderson, "The effects of element-level amplitude quantization on broadband beamforming in the presence of sinusoidal interference," Oceans '89, 1105-1110 (1989).

12. B. J. Sotirin and W. S. Hodgkiss, "Fine-scale measurements of the vertical ambient noise field," J. Acoust. Soc. Am. (submitted).

13. F. H. Fisher, "FLIP II concept," Oceans '89, 1520-1523 (1989).

14. B. J. Sotirin and W. S. Hodgkiss, "On array performance: an evaluation methodology using in-situ data," IEEE J. Oceanic Eng. (submitted).

15. W. S. Hodgkiss, "Shape determination of a shallow-water bottomed array," Oceans '89, 1199-1204 (1989).

Scripps Institution of Oceanography Reference Series

1. D. Alexandrou, "Selective reverberation cancellation via adaptive beamforming," SIO Reference 85-23, Scripps Institution of Oceanography, San Diego, CA, 154 pgs. (1985). Ph.D. Dissertation.

2. E. D. Bronson and L. R. Glosten, "FLIP - FLoating Instrument Platform," SIO Reference 85-21, Marine Physical Laboratory, Scripps Institution of Oceanography, San Diego, CA (1985). Revision of Previous SIO Reference 73-30 by Charles B. Bishop and Dewitt O. Efird.

Technical and Miscellaneous Reports

1. W. S. Hodgkiss, "Adaptive Signal Processing," Quarterly Progress Report for N00024-82-C-6400 for the Period 1 January 1983 - 31 March 1983, Marine Physical Laboratory, Scripps Institution of Oceanography, San Diego, CA (1983).

2. W. S. Hodgkiss, "Adaptive Signal Processing," Quarterly Progress Report for Contract N00024-82-C-6400 for the Period 1 July - 30 September 1983, (1983).

3. W. S. Hodgkiss, "Adaptive Signal Processing," Quarterly Progress Report for N00024-82-C-6400 for the Period 1 April 1983 - 30 June 1983, Marine Physical Laboratory, Scripps Institution of Oceanography, San Diego, CA (1983).

4. B. J. Sotirin, "Trip Report - ONR Contract N00014-87-C-0127," MPL-U-45/88, Marine Physical Laboratory, Scripps Institution of Oceanography, San Diego, CA (1988).

5. Andreas B. Rechnitzer, "The scientific research support potential of the submersible *MARITALIA 3GST9*," Final Subcontract Report for "Evaluation of Diver-Lockout Submersible" , Marine Physical Laboratory, Scripps Institution of Oceanography, San Diego, CA (1989).

Technical Memorandums

1. R. A. Harriss and C. B. Bishop, "SEACI IFF scientific users manual," MPL TM-370, Marine Physical Laboratory, Scripps Institution of Oceanography, San Diego, CA (1986).

2. R. W. Johnson and W. S. Hering, "An automated visible spectrum imaging system for atmospheric measurement and analysis," Atmospheric Visibility Technical Note 202, Visibility Laboratory, Scripps Institution of Oceanography, San Diego, CA (1986).

3. and W. S. Hering, "Automated visibility and cloud cover measurements with a solid-state imaging system," Atmospheric Visibility Technical Note 203, Visibility Laboratory, Scripps Institution of Oceanography, San Diego, CA (1986).

4. W. S. Hodgkiss and F. H. Fisher, "BAMBINO I," MPL TM-392, Marine Physical Laboratory, Scripps Institution of Oceanography, San Diego, CA, 32 pgs. (1987).

5. G. L. D'Spain, R. L. Culver, W. S. Hodgkiss, and G. L. Edmonds, "Freely drifting Swallow float array: August 1988 trip report," MPL TM-407, Marine Physical Laboratory, Scripps Institution of Oceanography, San Diego, CA (1988).

6. W. S. Hodgkiss and F. H. Fisher, "Vertical signal arrival structure," MPL TM-399, Marine Physical Laboratory, Scripps Institution of Oceanography, San Diego, CA (1988).

7. W. S. Hodgkiss and F. H. Fisher, "Vertical directionality of ambient noise at 32°N as a function of longitude - Tape #85010," MPL TM-387-B, Marine Physical Laboratory, Scripps Institution of Oceanography, San Diego, CA (1988).

8. W. S. Hodgkiss and F. H. Fisher, "Vertical directionality of ambient noise at 32°N as a function of longitude - Tape #86060," MPL TM-387-C, Marine Physical Laboratory, Scripps Institution of Oceanography, San Diego, CA (1988).

9. W. S. Hodgkiss and F. H. Fisher, "Vertical directionality of ambient noise at 32°N as a function of longitude - Tape #86247," MPL TM-387-D, Marine Physical Laboratory, Scripps Institution of Oceanography, San Diego, CA (1988).

10. W. S. Hodgkiss and F. H. Fisher, "Vertical directionality of ambient noise at 32°N as a function of longitude - Tape #86180," MPL TM-387-E, Marine Physical Laboratory, Scripps Institution of Oceanography, San Diego, CA (1988).

11. W. S. Hodgkiss and F. H. Fisher, "Vertical directionality of ambient noise at 32°N as a function of longitude," MPL TM-387-A, Marine Physical Laboratory, Scripps Institution of Oceanography, San Diego, CA (1988).

12. W. S. Hering, "Sky cover modeling concepts: An analysis," Atmospheric Visibility Technical Note 208, Visibility Laboratory, Scripps Institution of Oceanography, San Diego, CA (1988).

13. R. W. Johnson and W. S. Hering, "Automated visibility and cloud cover measurements with a solid-state imaging system (The as-built first generation)," Atmospheric Visibility Technical Note 207-A, Visibility Laboratory, Scripps Institution of Oceanography, San Diego, CA (1988).

14. R. W. Johnson T. L. Koehler and J. E. Shields, "A multi-station set of whole sky imagers and a preliminary assessment of the emerging database," Atmospheric Visibility Technical Note 210, Visibility Laboratory, Scripps Institution of Oceanography, San Diego, CA (1988).

15. Jean-Marie Tran, "Broadband spectral estimation using the multiple window method: A comparison with classical techniques," MPL TM-403, Marine Physical Laboratory, Scripps Institution of Oceanography, San Diego, CA (1988).

16. Jean-Marie Tran, "Parabolic equation model," MPL TM-401, Marine Physical Laboratory, San Diego, CA (1988).

17. G. L. D'Spain, R. L. Culver, W. S. Hodgkiss, and G. L. Edmonds, "Freely drifting Swallow float array: August 1988 trip report," MPL TM-407, Marine Physical Laboratory, Scripps Institution of Oceanography, San Diego, CA (1989).

18. B. J. Sotirin and W. S. Hodgkiss, "Navigation software for the MPL vertical line array," MPL TM-409, Marine Physical Laboratory, Scripps Institution of Oceanography, San Diego, CA (1989).

19. B. J. Sotirin and W. S. Hodgkiss, "On array performance: A methodology of system calibration and noise identification," MPL TM-410, Marine Physical Laboratory, Scripps Institution of Oceanography, San Diego, CA (1989).

20. B. J. Sotirin and W. S. Hodgkiss, "Large aperture array measurements of the vertical ambient noise field," MPL TM-411, Marine Physical Laboratory, Scripps Institution of Oceanography, San Diego, CA (1989).

21. B. J. Sotirin and W. S. Hodgkiss, "Vertical directionality measurements of ambient noise in the NE Pacific," MPL TM-412, Marine Physical Laboratory, Scripps Institution of Oceanography, San Diego, CA (1989).

22. G. L. D'Spain, W. S. Hodgkiss, and G. L. Edmonds, "Freely drifting Swallow float array: September 1987 trip report," MPL TM-413, Marine Physical Laboratory, Scripps Institution of Oceanography, San Diego, CA (1989).

APPENDIX B

Research Articles

"The Effects of Array Shape Perturbation on Beamforming and Passive Ranging" by William S. Hodgkiss (Appears In: IEEE Journal of Oceanic Engineering, Vol. OE-8, No. 8, 1983).

"Applications of Adaptive Array Processing" by W. S. Hodgkiss and D. Alexandrou. (Appears In: Adaptive Methods in Underwater Acoustics, Heinz G. Urban (Editor), (Boston: D. Reidel Publishing Co., 1985), pp. 447-460).

"Boundary Reverberation Rejection via Constrained Adaptive Beamforming" by Dimitri Alexandrou. (Appears In: J. Acoust. Soc. Am., Vol. 82, No. 4, pp. 1274-129, 1987).

"Large Aperture Digital Acoustic Array" by Barbara J. Sotirin and John A. Hildebrand (Appears In: IEEE Journal of Oceanic Engineering, Vol. 13, No. 4, pp. 271-281, 1988).

"Acoustic Navigation of a Large-Aperture Array" by Barbara J. Sotirin and John A. Hildebrand. (Appears In: J. Acoust. Soc. Am., Vol. 87, No. 1, pp. 154-167, 1990).

"FLIP II" by Frederick H. Fisher (Appears In: IEEE Journal of Oceanic Engineering, Vol. 13, No. 4, 1988).

The Effects of Array Shape Perturbation on Beamforming and Passive Ranging

WILLIAM S. HODGKISS, JR., MEMBER, IEEE

(Invited Paper)

Abstract—**The problem of beam formation from a towed line array whose shape has been distorted is considered. Emphasis is placed on the beam broadening and range estimation effects of array shape perturbations and how the resulting losses can be regained if the actual element positions are known. Specific illustrations are provided for various levels of shape distortion. For example, a 15-m bow in a 232.5-m-long array broadens the beamwidth by a factor of 3 at 50 Hz. As another example, a 6-m bow in an 800-m-long array leads to a 20-percent range underestimation at 10 km for a 100–500-Hz broadband source.**

I. INTRODUCTION

TOWED LINE ARRAYS provide a means of physically separating acoustic sensors from the relatively high noise environment of the towing platform and the aperture size limitations imposed by the length of the platform. Against these advantages are the disadvantages inherent to an array processing situation where the sensor locations vary dynamically due to various hydrodynamic forces and towing platform maneuvers.

The subject of this paper is the problem of beam formation from a towed line array whose shape has been distorted. In Section II, plane wave beamforming will be considered. Correspondingly, Section III will discuss curved wavefront or focused beamforming. In both sections, the emphasis is on the effects of array shape perturbation and how the resulting losses can be regained if the actual array element positions are known. Towed arrays have been the subject of considerable attention over the past decade, although much of the literature is not readily accessible. Articles which can be found in the open literature in the areas of beamforming and both bearing and range estimation include references [1]-[13].

II. BEAMFORMING

The advent of long towed arrays has improved significantly the ability to detect and track distant sources A line array has a fundamental limitation in that it exhibits a right–left ambiguity. One method of resolving this ambiguity is for the towing platform to undergo a maneuver thus altering the relative spatial orientation of the source and platform.

Manuscript received January 17, 1983; revised May 9, 1983. This work was supported by the Office of Naval Research under Contract N00014-80-C-0220. The paper is a contribution of the Scripps Institution of Oceanography, new series.

The author is with the Marine Physical Laboratory, Scripps Institution of Oceanography, San Diego, CA 92152.

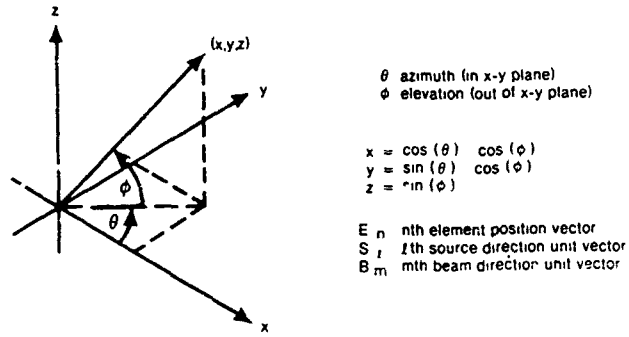

Fig. 1. Coordinate system definition and vector notation.

The major difficulty with this approach is that conventional beamformers can not continue accurate beamforming during the maneuver due to array deformation. A certain amount of time must elapse (from several minutes to tens of minutes depending on the array length and platform speed) for the array to straighten out. Since the source track most likely will have been lost during this period, it must be reacquired at the completion of the maneuver.

The mathematics of beamforming is developed below along with several examples, illustrating the influence of severe array distortion on conventional beamformer output. Related literature includes [1]-[3].

A. Plane Wave Beamforming

Consider a coordinate system defined as in Fig. 1. The beamforming task consists of generating the waveform $b_m(t)$ for each desired steered beam direction $\boldsymbol{B}_m$. Each $b_m(t)$ consists of the sum of suitably time delayed replicas of the individual element signals $e_n(t)$. The time delays compensate for the assumed differential travel-time differences between sensors for a signal from the desired beam direction.

Let the output of an element located at the origin of coordinate due to the lth source by $s_l(t)$. Under the assumption of plane wave propagation, a source from direction $\boldsymbol{S}_l$ produces the following sensor outputs

$$e_n(t) = s_l\left(t + \frac{\boldsymbol{E}_n' \cdot \boldsymbol{S}_l}{c}\right) \tag{1}$$

where c is the (constant) speed of propagation (independent of location) and $\boldsymbol{E}_n'$ indicates the true nth element position

0364-9059/83/0700-0120$01.00 © 1983 IEEE

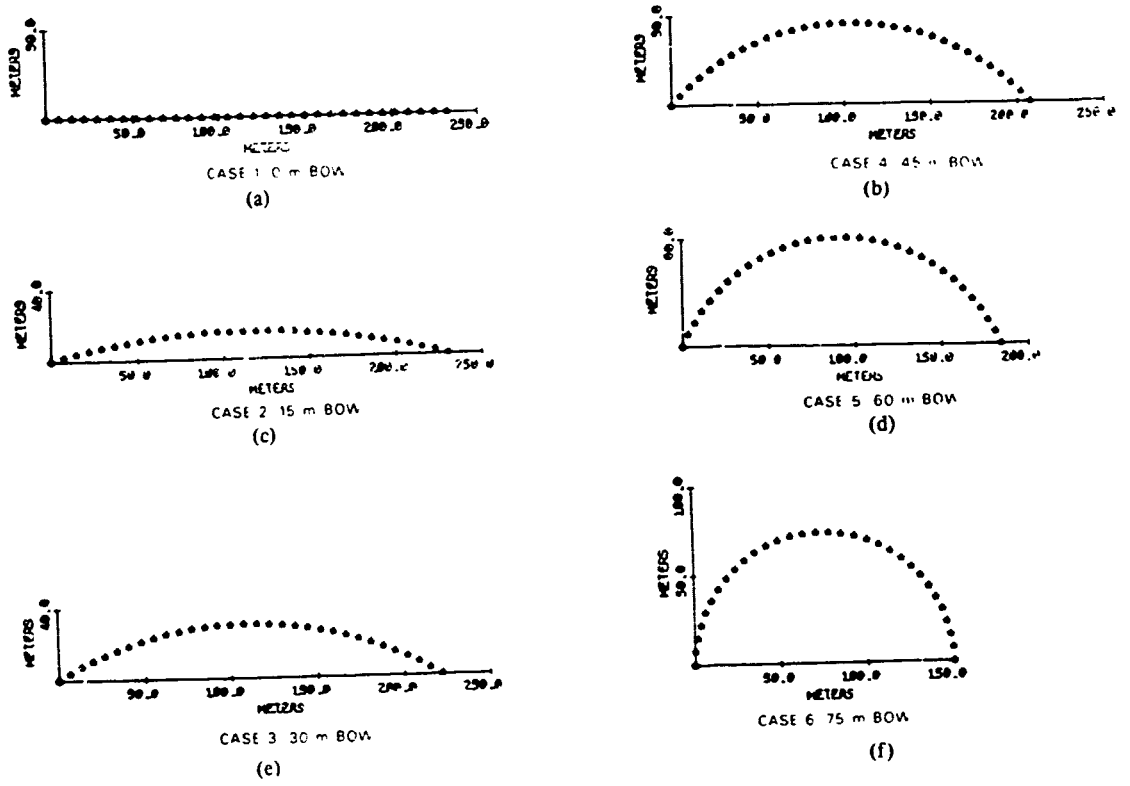

Fig 2. Array geometries: 32 elements, 7.5-m spacing.

which may differ from the assumed location E_n. Appropriately delaying the individual element signals to point a beam in the direction B_m yields the beamformer output

$$b_m(t) = \sum_{n=1}^{N} w_n e_n \left(t - \frac{E_n \cdot B_m}{c} \right) \tag{2}$$

$$= \sum_{n=1}^{N} w_n s_1 \left(t + \frac{E_n' \cdot S_i - E_n \cdot B_m}{c} \right) \tag{3}$$

where the w_n are weights which have been applied to each element signal.

B. Examples

Beamforming for the six array geometries depicted in Fig. 2 will be used in examples to supplement the foregoing mathematical derivation. Each array has 32 elements with a constant interelement spacing of 7.5 m thus yielding a total array length of 232.5 m. The cases considered form a progression of increasing array bow, starting with an exactly straight array and continuing in 15-m increments up to 75-m bow, which corresponds roughly to a half-circle geometry. These shapes have been chosen for the sake of simplicity and are not intended to represent any particular operational scenario. For the 50-Hz analysis frequency considered and an assumed sound speed at 1500 m/s, $\lambda = 30$ m and the array has an interelement spacing of $\lambda/4$, total length of 7 3/4 λ, and bow increments of $\lambda/2$ from 0 λ (case 1) to 2 1/2 λ (case 6).

The remaining figures illustrate four source direction situations: $\theta = 90°, \phi = 0°$ (Fig. 3); $\theta = 45°, \phi = 0°$ (Fig. 4); $\theta = 135°, \phi = 0°$ (Fig. 5); and both $\theta = 45°$ and $\theta = 90°, \phi = 0°$ (Fig. 6). Each figure investigates all six cases of array bow. Two bearing response plots are provided for each case: 1) assumed element positions same as actual element positions ($E_n = E_m'$) and 2) assumed element positions always those of case 1 (straight array). The two bearing response plots correspond to (3) where $w_n = 1$, $s_1(t) = \exp(j\omega t)$, and the set $\{B_m\}$ consists of 128 beam vectors uniformly spaced in spatial angle from $\theta = 0°$ through $\theta = 180°$. All of the plots have been normalized by their own individual maximum response value versus bearing.

Figs. 3–5 investigate situations involving a single source. In all six cases for each figure, the first bearing response plot is that for a beamformer which knows the array element positions exactly. As expected for uniform weighting of the element signals, the first sidelobe is at −13 dB for case 1 (straight array) and −7 dB for case 6 (half-circle array). The second bearing response plot is that for a beamformer which assumes the element positions are those of the straight array irrespective of their true locations. The effect of not properly incorporating the actual array element locations into the beamformer process is a progressive degradation in the directivity or resolution capability of the beamformer while moving from case 2 through case 6.

Fig. 6 investigates a situation involving two sources spaced 45° apart in spatial angle. Comments regarding the two bearing response plots for the six cases essentially are the same as noted for the single source situations in Figs. 3–5.

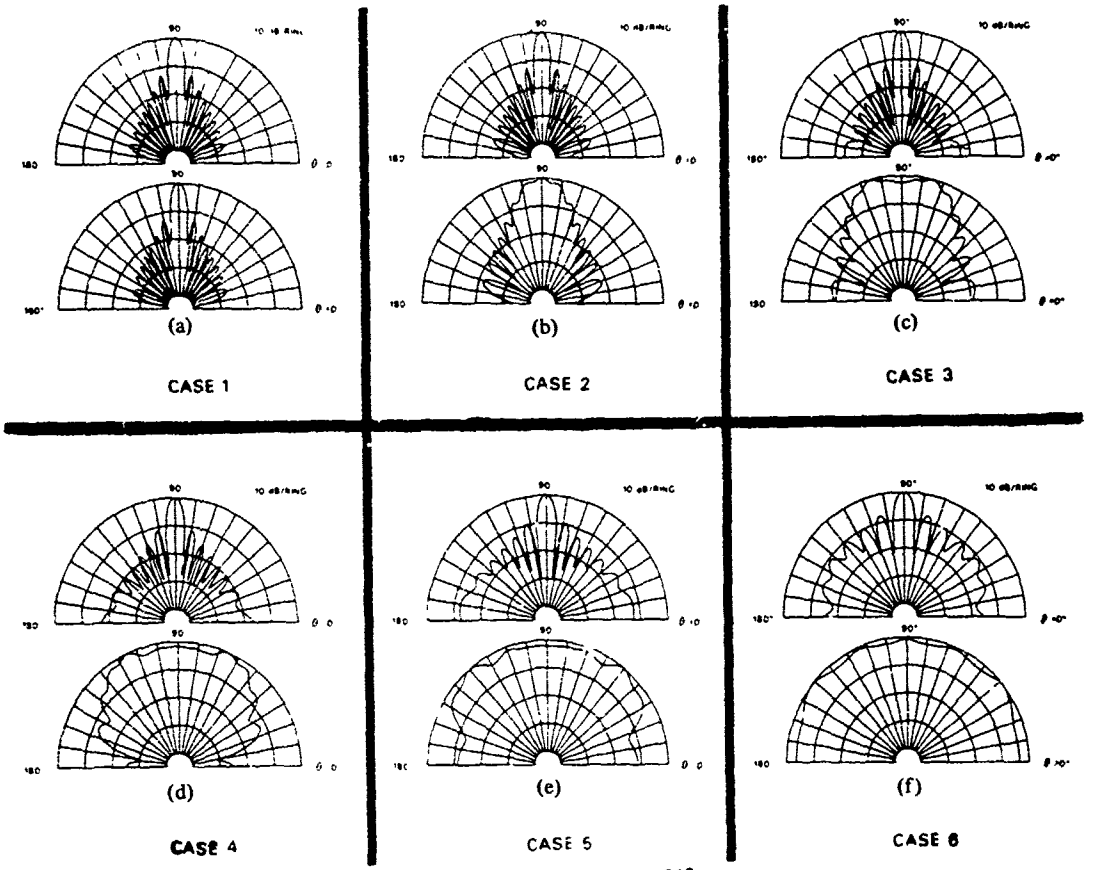

Fig 3. Source direction: $\theta = 90°$.

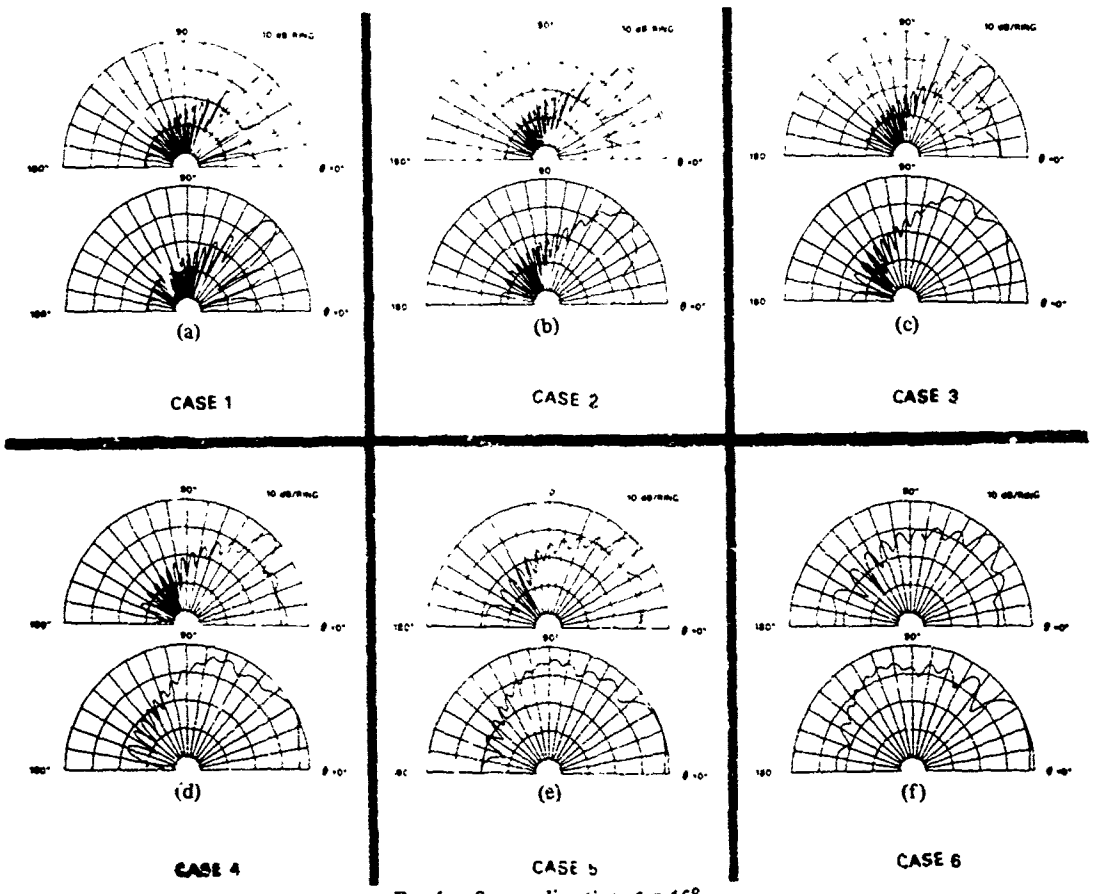

Fig. 4. Source direction: $\theta = 45°$.

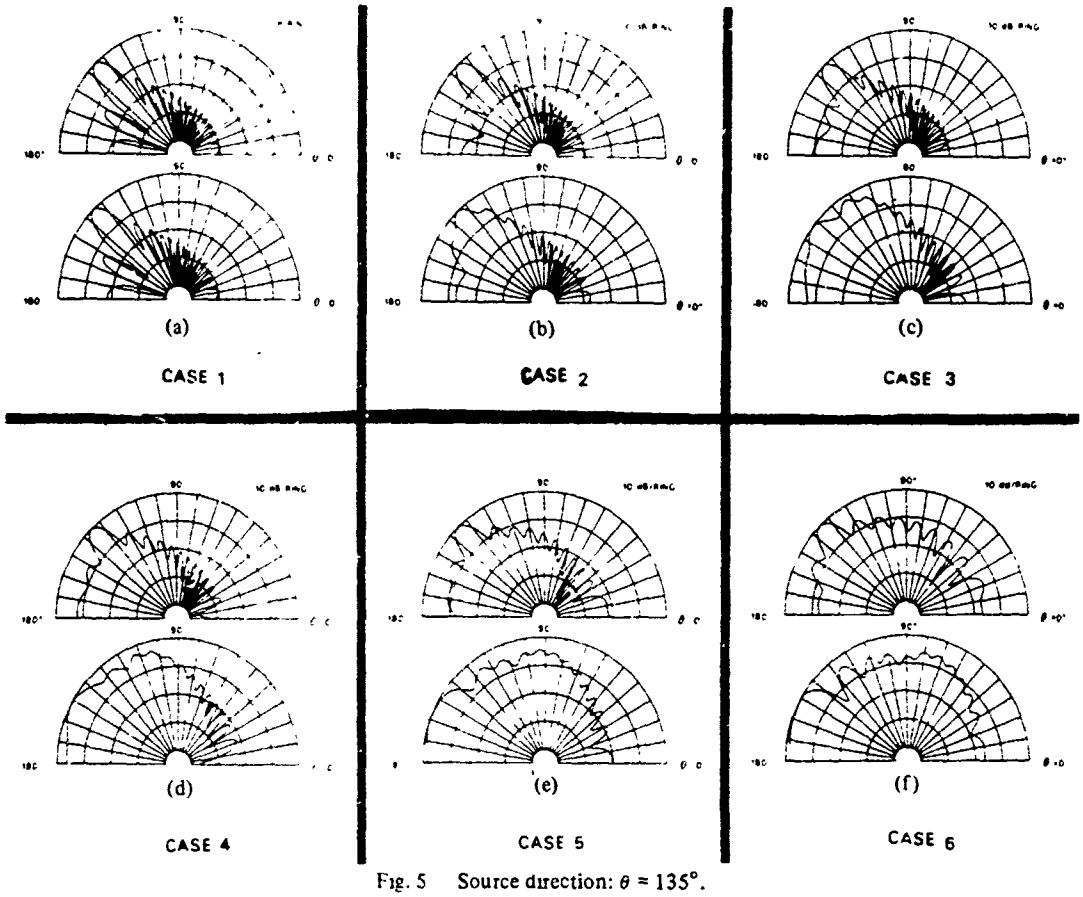

Fig. 5 Source direction: $\theta = 135°$.

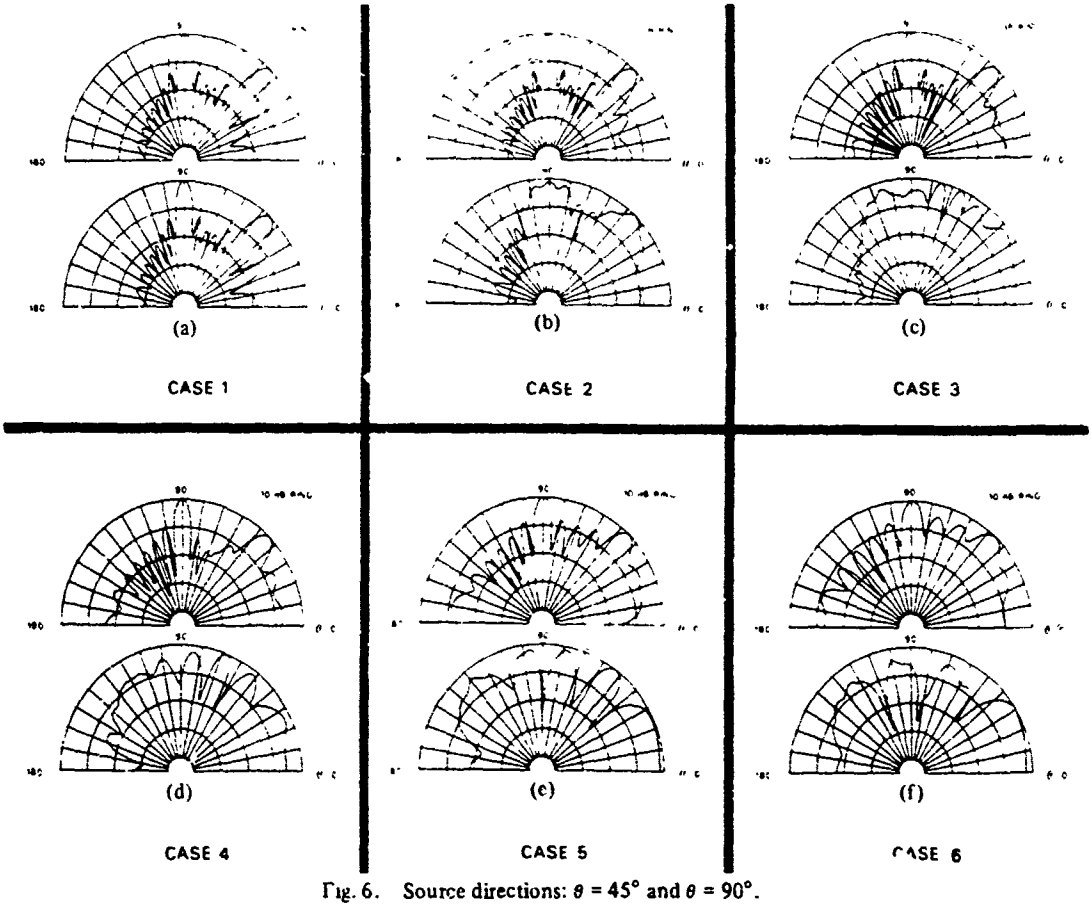

Fig. 6. Source directions: $\theta = 45°$ and $\theta = 90°$.

III. PASSIVE RANGING

Triangulation and wavefront curvature are two popular approaches to the passive ranging problem [9], [11], [13]. Although differing from a systems engineering viewpoint, they are quite similar mathematically. Essentially, triangulation considers two arrays where the intersection of their respective bearing lines provides source location information. Three arrays are employed in wavefront curvature processing to estimate the two delays from the forward array to the midarray and from the midarray to the after array. Wavefront curvature can be viewed as triangulation by envisioning the triple aperture and one system as being two arrays, one composed of the forward and midarrays and one composed of the mid and after arrays. Both triangulation and wavefront curvature are extremely sensitive to location uncertainty of the constituent subarrays. In particular, bowing or noncollinearity is more serious than array displacement and array rotation [9].

From an estimation theory point of view, the optimal solution to the passive ranging problem consists of the maximum likelihood (ML) processor. When the sensor (element) positions are known, the ML estimate of bearing and range is obtained by focusing the individual element time delays at many hypothesized range and bearing pairs and by selecting the pair which yield the largest system time-delay-and-sum output [4]-[8], [10]-[12]. ML processing (focused beamforming) is robust to element location uncertainty when the error is independent from element to element. The mathematics of focused beamforming is developed below along with several examples illustrating the influence of various geometrical parameters on processor output.

A. Curved Wavefront Beamforming

Consider again the coordinate system defined in Fig. 1. The curved wavefront or focused beamforming task consists of generating the waveform $b_m(t)$ for each desired steered beam direction $\boldsymbol{B}_m$ and range of focus r_m. Each $b_m(t)$ consists of the sum of suitably delayed replicas of the individual element signals $e_n(t)$. The time delays compensate for the assumed differential travel time differences between sensors for a signal from the desired beam direction and range.

Let the output of an element located at the origin of coordinates due to the lth source by $s_l(t)$. A source from direction $\boldsymbol{S}_l$ and range r_l produces the following sensor outputs:

$$e_n(t) = s_l\left(t + \frac{r_l - |r_l \boldsymbol{S}_l - \boldsymbol{E}_n'|}{c}\right)$$

$$= s_l\left(t + \frac{r_l - (r_l^2 + |\boldsymbol{E}_n'|^2 - 2r_l \boldsymbol{S}_l \cdot \boldsymbol{E}_n')^{1/2}}{c}\right) \tag{4}$$

where c is the (constant) speed of propagation (independent of location) and $\boldsymbol{E}_n'$ indicates the true nth element position which may differ from the assumed location $\boldsymbol{E}_n$. Appropriately delaying the individual element signals to focus a beam in the direction $\boldsymbol{E}_m$ and range r_m yields the focused beamformer output

$$b_m(t) = \sum_{n=1}^{N} w_n e_n\left(t - \frac{r_m - |r_m \boldsymbol{B}_m - \boldsymbol{E}_n|}{c}\right)$$

$$= \sum_{n=1}^{N} w_n \cdot e_n\left(t - \frac{r_m - (r_m^2 + |\boldsymbol{E}_n|^2 - 2r_m \boldsymbol{B}_m \cdot \boldsymbol{E}_n)^{1/2}}{c}\right) \tag{5}$$

$$= \sum_{n=1}^{N} w_n s_l(t + r_l - r_m + (r_m^2 + |\boldsymbol{E}_n^2|$$

$$- 2r_m \boldsymbol{B}_m \cdot \boldsymbol{E}_n)^{1/2} - (r_l^2 + |\boldsymbol{E}_n'|^2$$

$$- 2r_l \boldsymbol{S}_l \cdot \boldsymbol{E}_n')^{1/2}/c) \tag{6}$$

where the w_n are weights which have been applied to each element signal.

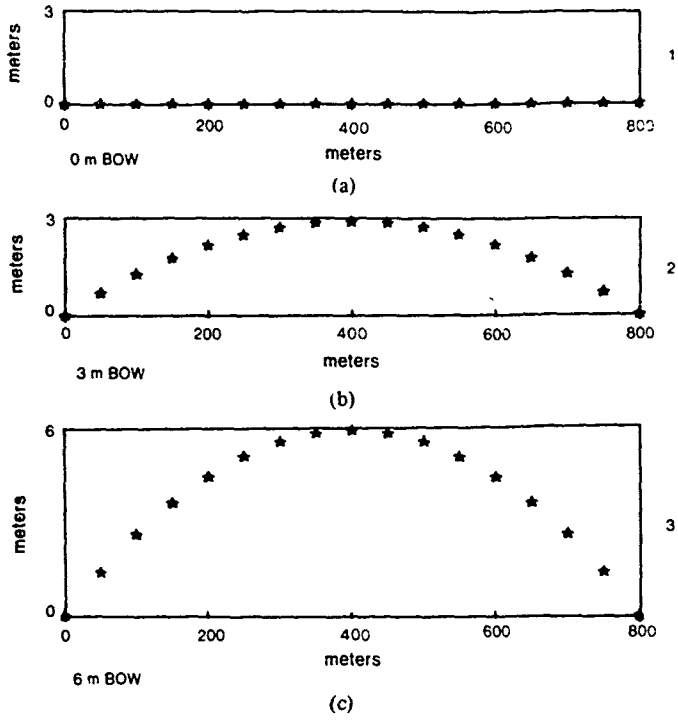

Fig. 7. Array geometries: 17 elements.

B. Examples

Curved wavefront or focused beamforming for the six array geometries depicted in Fig. 7 will be used as examples to supplement the foregoing mathematical derivations. The three arrays in Fig. 7 each have 17 elements with a constant interelement spacing of 50 m thus yielding a total array length of 800 m. The second and third arrays differ from the first in that the elements take on a gradual bow reaching a peak offset for the center array element of 3 m (Fig. 7(b))

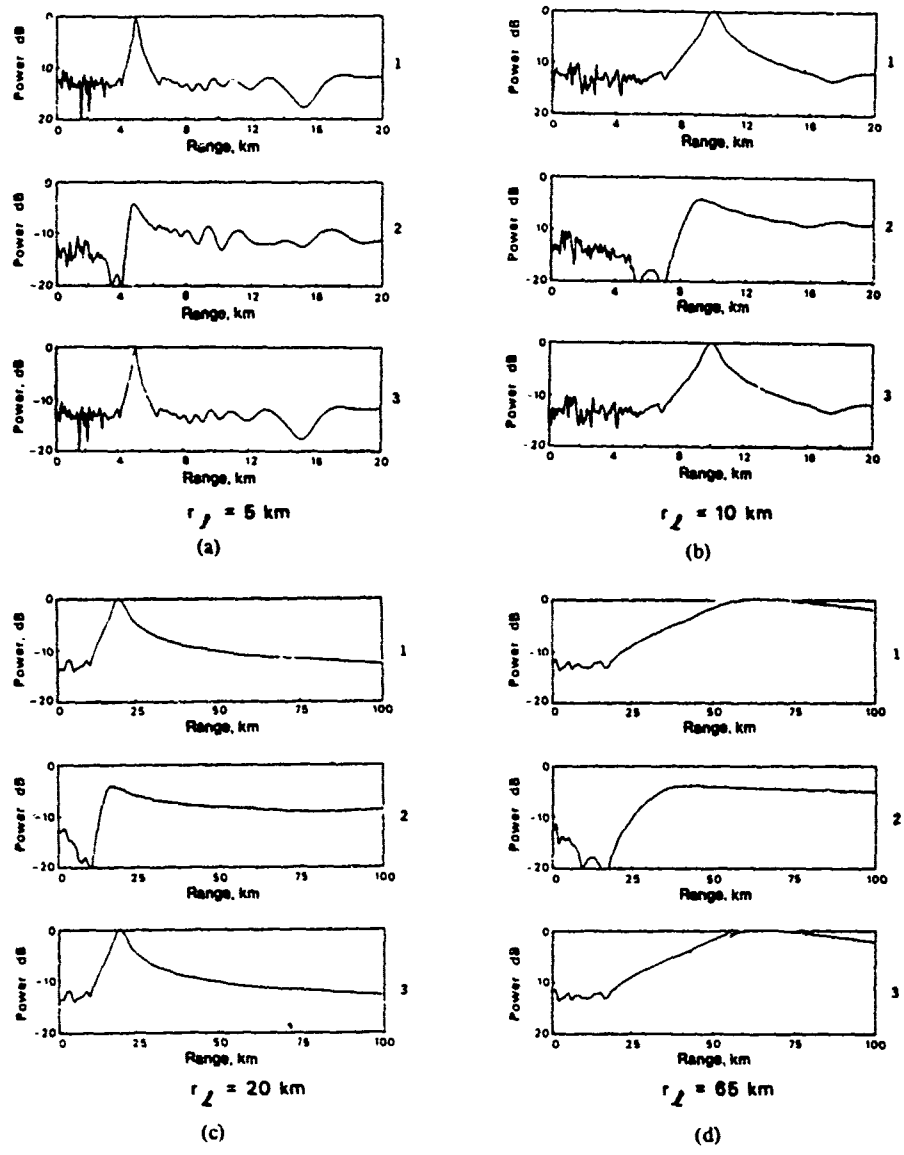

Fig. 8. 17-element array: 0-m and 3-m bow ($\theta_m = \theta_l = 90°$).

or 6 m (Fig. 7(c)) from a straight line connecting the first and last elements. As with the examples in Section II, these shapes have been chosen for the sake of simplicity and are not intended to represent any particular scenario.

For each array geometry, four ranges to a broadside source ($\theta_1 = 90°, \phi = 0°$) are investigated: 1) $r_l = 5$ km; 2) $r_l = 10$ km; 3) $r_l = 20$ km; and 4) $r_l = 65$ km. A wide-band source signal was simulated by the incoherent (power) addition of the response of the focused beamformer to five tonals uniformly spread across the band of 100–500 Hz. Three types of plots are presented illustrating the response of the focused beamformer range with $\theta_m = \theta_l$, azimuth with $r_m = r_l$, and the three-dimensional range-azimuth surface.

The range and azimuth plots represent orthogonal slices through the range-azimuth surface which intersect at the source location r_l and θ_l. For each source range r_l, three range and azimuth plots are provided: 1) focused beamformer response for the straight array ($E_n = E_n'$); 2) focused beamformer response for the bowed array when the elements incorrectly are assumed straight ($E_n \neq E_n'$); and 3) focused beamformer response for a bowed array whose element positions are correctly incorporated into the focused beamforming process ($E_n = E_n'$). Also provided for each source range r_l are three-dimensional range-azimuth surfaces for the first case noted above (straight array with $E_n = E_n'$).

Figs. 8–12 illustrate the focused beamformer response for the 17-element arrays. The range plots indicate a distinct response peak when the array element positions are correctly incorporated into the focused beamforming process. When the array actually is bowed but is assumed straight for the focused beamforming operation, a significant distortion of the range response occurs. The distortion consists of both a shift in the peak response such that the range is underestimated as well as a slow decrease in response for ranges beyond the peak rendering a determination of the exact range where the peak occurs more difficult. The surface of the focused beamformer reponse as a function of both range r_m and azimuth θ_m is illustrated nicely in Fig. 12.

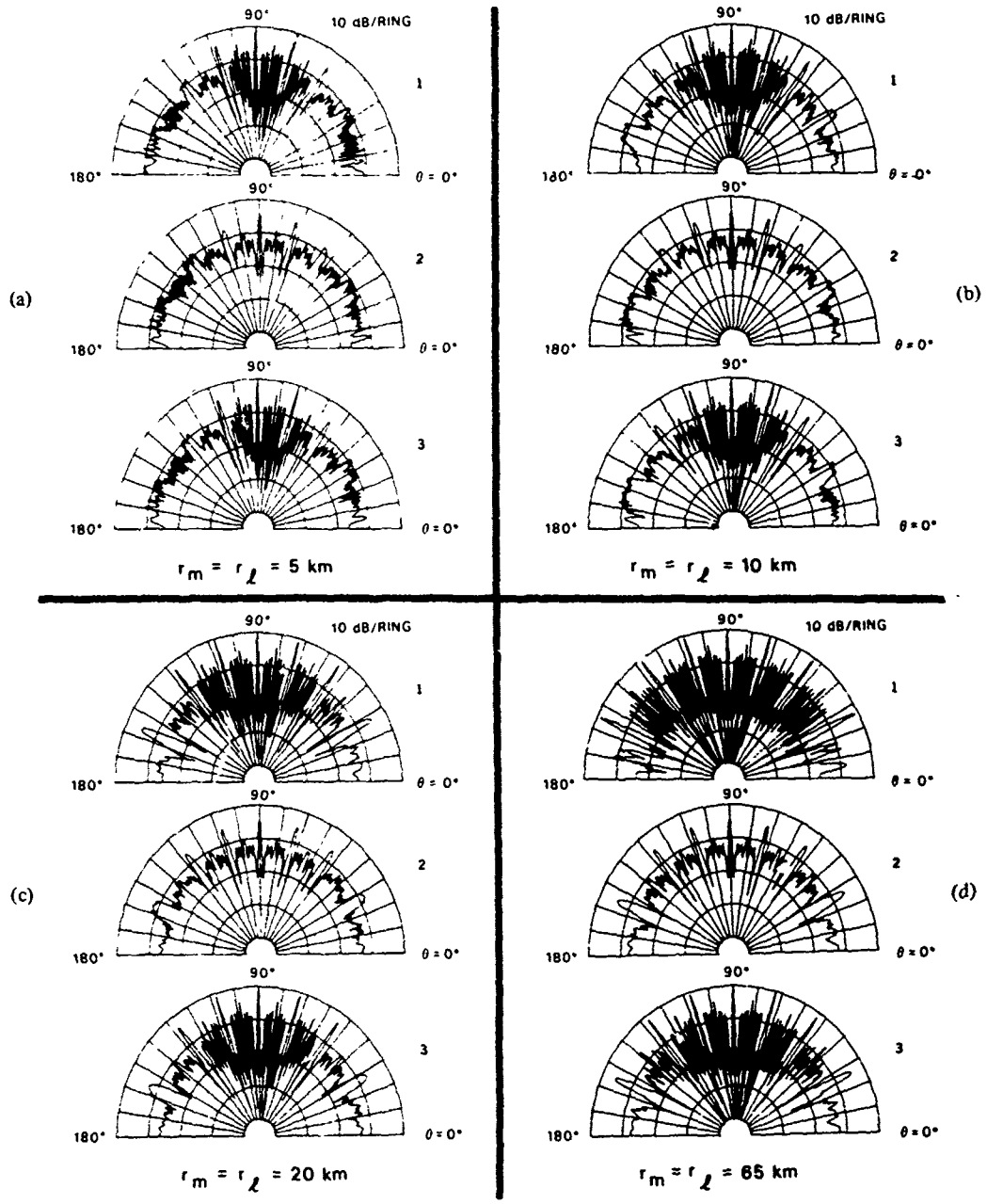

Fig. 9. 17-element array 0-m and 3-m bow ($\theta_l = 90°$).

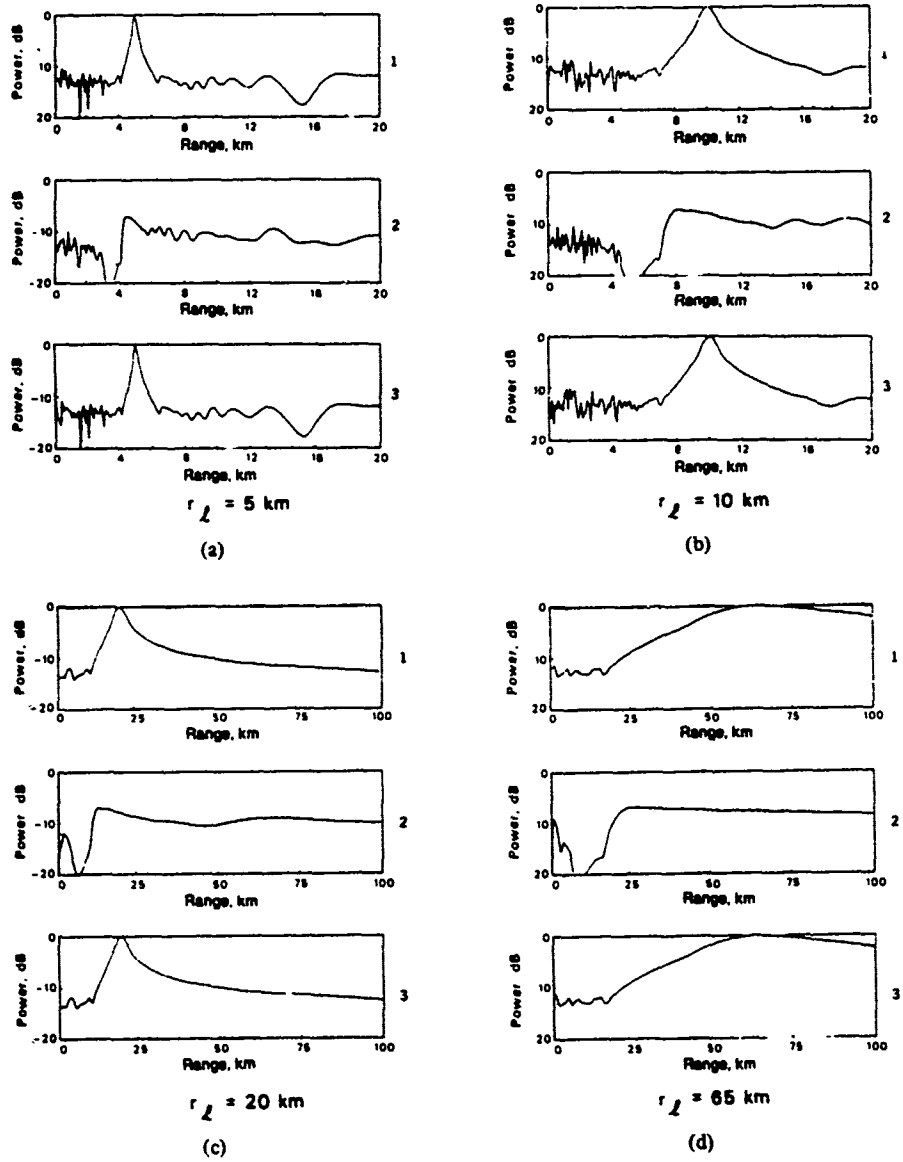

Fig. 10. 17-element array: 0-m and 6-m bow ($\theta_m = \theta_l = 90°$).

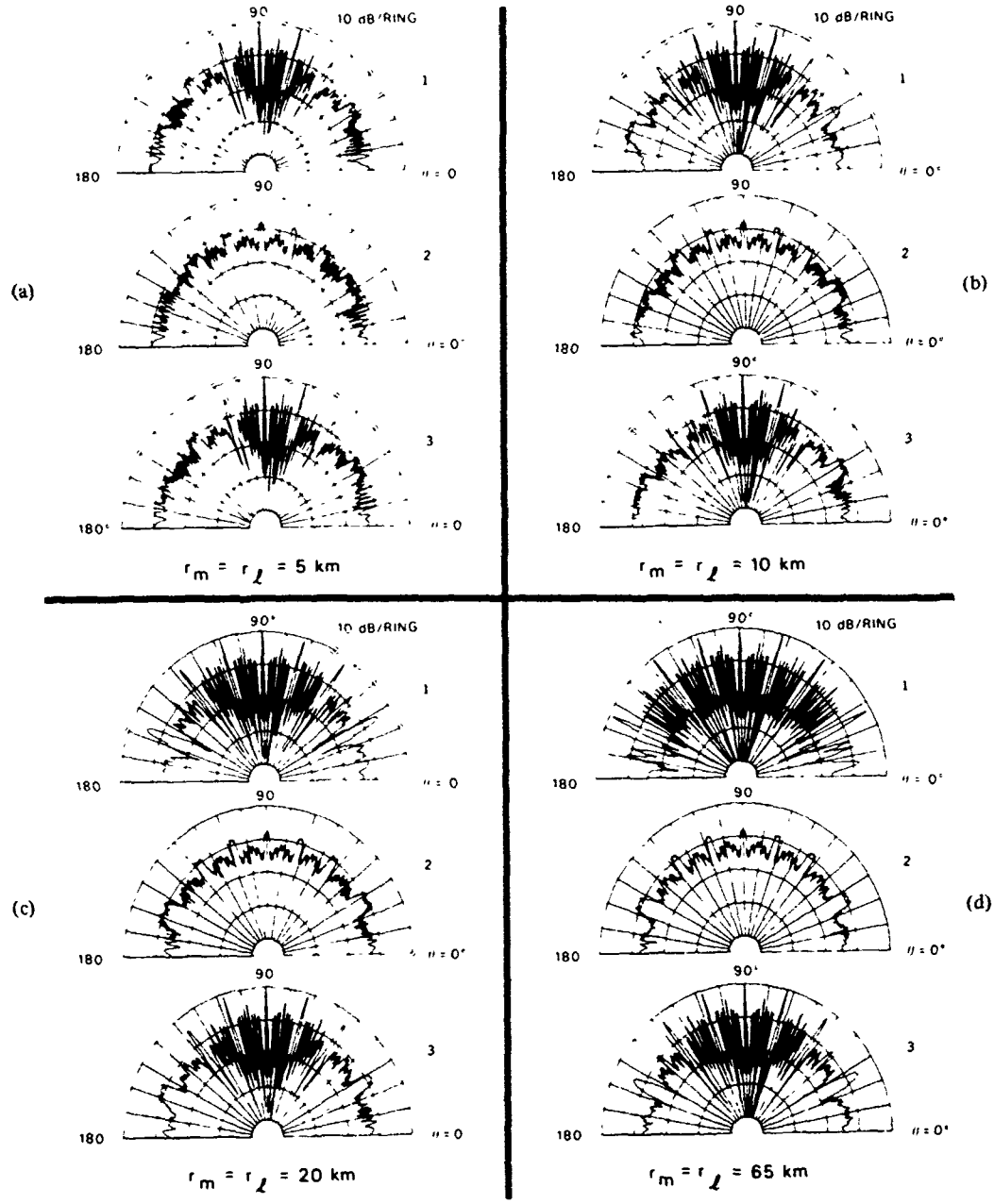

Fig. 11. 17-element array: 0-m and 6-m bow ($\theta_l = 90°$).

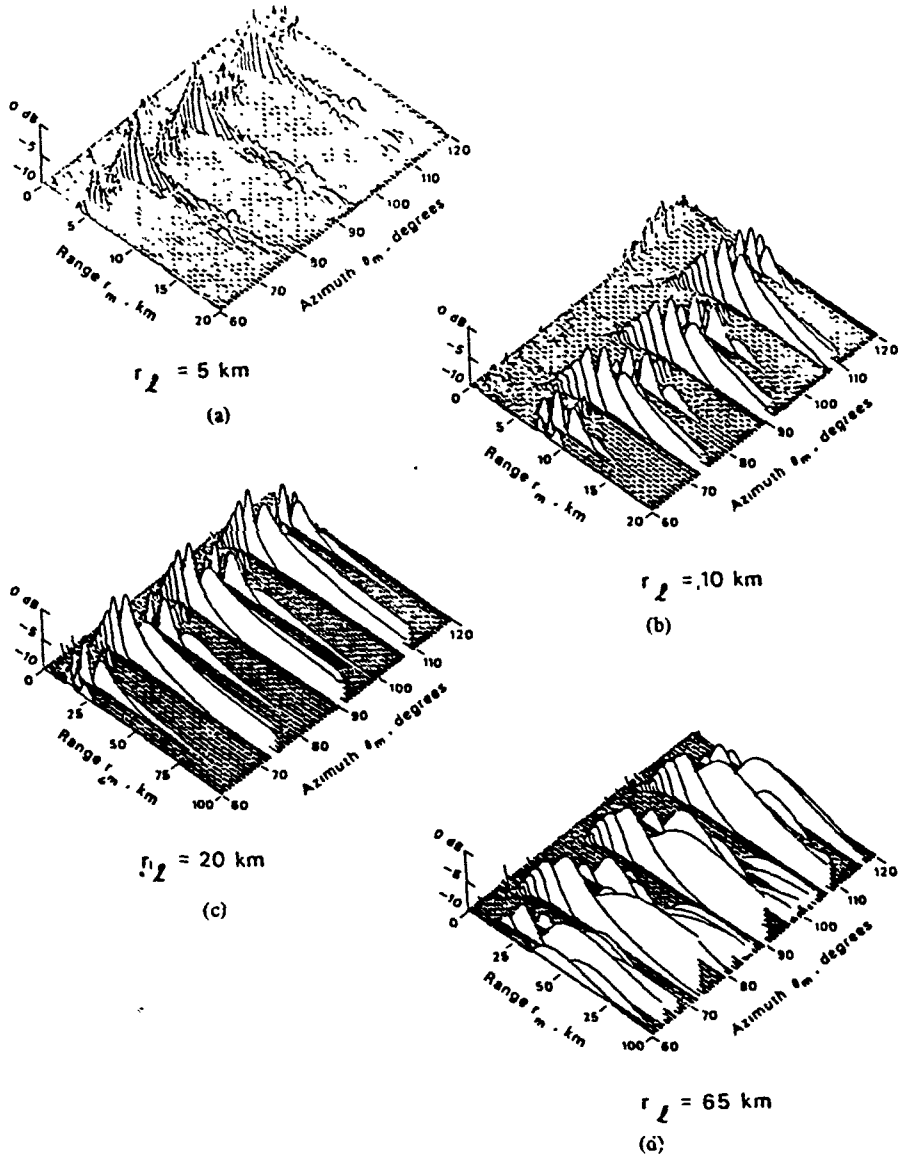

Fig. 12. 17-element array: 0-m bow ($\theta_\ell = 90°$).

IV. SUMMARY

The subject of this paper has been the problem of beam formation from a towed line array whose shape has been distorted. Essentially, the following has been demonstrated via these examples.

1) Perturbations from an assumed perfectly straight shape have serious consequences with regards to bearing and range estimation.

2) When the actual perturbed array shape is incorporated into the signal processing, desired system performance is regained.

Conventional array processing systems do not have the capability to account for the noncollinearity of the array elements. An approach to eliminate the undesired loss of system performance would be to carry out the beamforming dynamically. As an example, the MPL Dynamic Beamformer permits the incorporation of slow changes in element positions and beam steering directions while the beamformer carries out the real-time formation of 1300 beams from 32 input sensors [14]. The element coordinates are updated periodically so that the required time delays for each element signal can be computed for pure time-delay-and-sum beam formation in any specified direction. The original motivation behind the fabrication of a dynamically programmable beamformer by MPL was the coherent processing of data from a drifting sonobuoy array. In that program, the spatial distribution of the sonobuoy field was determined by an active array element location system. For towed array work, an alternative to an active element location system would be utilization of an algorithm which would predict the element positions based on parameter inputs (e.g., tow point trajectory) which characterize the time-evolving shape of the array.

ACKNOWLEDGMENT

The examples were carried out by L. P. Berger of the Marine Physical Laboratory.

REFERENCES

[1] B. D Steinberg, *Principles of Aperture and Array System Design* New York. NY, 1976

[2] H P Bucker, "Beamforming a towed line array of unknown shape," *J Acoust. Soc Amer*, vol 63, pp 1451–1454, 1978.

[3] D. J Ramsdale and R A Howerton, "Effect of element failure and random errors in amplitude and phase on the sidelobe level attainable with a linear array," *J Acoust Soc Amer*, vol 68, pp 901–906, 1980.

[4] V H MacDonald and P M Schultheiss, "Optimum passive bearing estimation in a spatially incoherent noise environment," *J Acoust Soc. Amer*, vol 46, pp 37–43, 1969.

[5] W. R Hahn, "Optimum signal processing for passive sonar range and bearing estimation," *J. Acoust Soc Amer*, vol 58, pp 201–207, 1975.

[6] M. J. Hinich and W. Rule, " Bearing estimation using a large towed array," *J Acoust Soc Amer*, vol. 58, pp 1023–1029, 1975

[7] M J. Hinich, "Bearing estimation using a perturbed linear array," *J. Acoust Soc Amer*, vol 61, pp 1540–1544, 1977

[8] G C Carter, "Variance bounds for passively locating an acoustic source with a symmetric line array," *J Acoust Soc Amer*, vol 62, pp 922–926, 1977

[9] G C Carter, "Passive ranging errors due to receiving hydrophone position uncertainty," *J Acoust Soc Amer*, vol 65, pp 528–530, 1979

[10] P. M Schultheiss and J P Ianniello, "Optimum range and bearing estimation with randomly perturbed arrays," *J Acoust Soc Amer*, vol. 68, pp 167–173, 1980

[11] G C Carter, "Time delay estimation for passive sonar signal processing," *IEEE Trans Acoust, Speech, Signal Processing*, vol. ASSP-29, pp 463–470, 1981.

[12] N. L Owsley and G. R. Swope, "Time delay estimation in a sensor array," *IEEE Trans. Acoust, Speech, Signal Processing*, vol ASSP-29, pp 519–523, 1981.

[13] K. B Theriault and R M Zeskind, "Inherent bias in wavefront curvature ranging," *IEEE Trans. Acoust, Speech, Signal Processing*, vol. ASSP-29, pp. 524–527, 1981

[14] W. S Hodgkiss and V. C Anderson, "Hardware dynamic beamforming," *J. Acoust. Soc Amer*, vol 69, pp 1075–1083, 1981

★

William S. Hodgkiss, Jr. (S'68–M'75), for a photograph and biography please see page 119 of this issue.

APPLICATIONS OF ADAPTIVE ARRAY PROCESSING

W.S. Hodgkiss and D. Alexandrou

Marine Physical Laboratory
Scripps Institution of Oceanography
San Diego, CA 92152

ABSTRACT

The application of adaptive least-squares lattice structures to problems in underwater acoustics is explored. The focus of attention is on the active sonar problem where a strong component of surface reverberation exists. Both single and dual channel problems are considered. The prewhitening of acoustic reverberation data is used as an illustration of the former while sea surface reverberation rejection is used as an illustration of the latter.

1.0 INTRODUCTION

Numerous applications exist which require a linear filtering operation. Often, the nature of that filtering task is time varying in some nondeterministic fashion due to nonstationarity of the underlying time series. In such situations, a filter which can adapt to a changing environment is needed.

Here, the application of adaptive least-squares lattice structures to problems in underwater acoustics is explored. Both single and dual channel problems are considered. The prewhitening of acoustic reverberation data is used as an illustration of the former while sea surface reverberation rejection is used as an application of the latter.

H. G. Urban (ed.), Adaptive Methods in Underwater Acoustics, 447–460
© 1985 by D. Reidel Publishing Company

Acoustic reverberation data has a complex and highly variable power spectrum. The spatial transfer function characteristics of both the transmitting and receiving transducers have a significant influence on the time-evolving shape of the corresponding range-Doppler map. Furthermore, depending on the location of the transducers in the water column, the ocean's boundaries (both surface and bottom) can add major contributions which characteristically have a sudden onset. Figure 1 illustrates graphically the origin of the three major contributors (surface, volume, and bottom) to the reverberation time series.

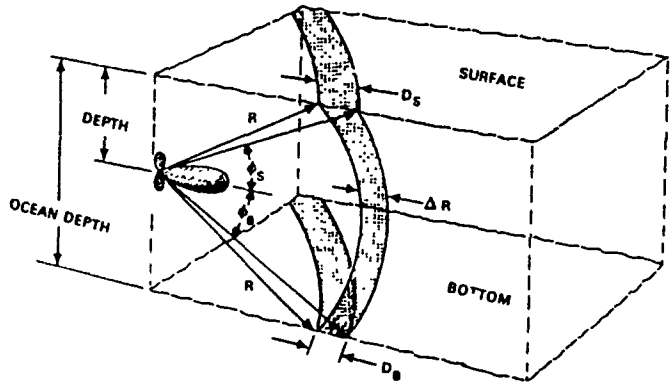

Figure 1. Reverberation model geometry.

As an illustration of an interesting application area where reverberation is both the signal of interest as well as a potential contaminant, consider the Doppler sonar problem. Doppler sonars use the perceived shift in carrier frequency between the outgoing pulse and the returning echo to make an estimate of scatterer radial velocity at several ranges of interest. Scatterers suspended neutrally buoyant in the water column are used as tracers for the remote sensing of water mass motion. Essentially, the problem is one of high resolution (distinguishing small differences in velocity) spectral estimation across short data segments (range bins). Adaptive spectral estimation techniques can be used to follow the time-evolving (corresponding to range) spectral characteristics of a returning echo. A simplistic model of the corresponding range-Doppler map (a three-dimensional surface) consists of a single symmetrical hump whose track as a function of time is indicative of the radial velocity of scatters in successive range cells. However, a more careful consideration of the sonar transducer's spatial response characteristics suggests that surface reverberation can be a significant contaminant in the range-Doppler map.

2.0 THE COMPLEX ADAPTIVE JOINT PROCESS ALGORITHM

The general problem of interest is dual channel. As will be seen, the single channel algorithm is embedded in the dual channel structure. The direct form implementation of the joint process structure is illustrated in Figure 2. The current and

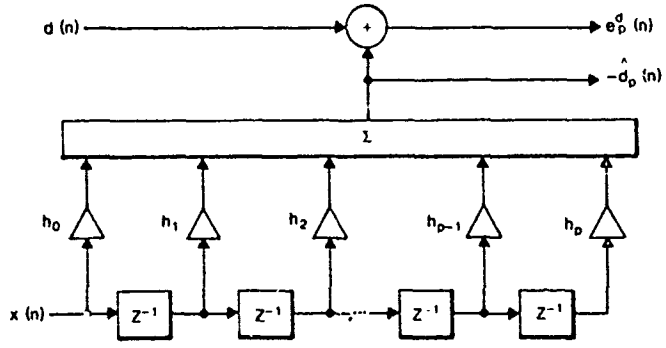

Figure 2. Direct form realization of the joint process structure.

most recent p samples of the reference channel process $\{x(n),x(n-1),\ldots,x(n-p)\}$ are linearly combined to form an estimate of $-d(n)$. Of particular interest in noise cancelling applications is the residual $e^d_p(n)$ obtained by subtracting the filtered reference channel from the primary channel [6]. The corresponding transfer function of the reference channel filter is given by

$$H(z) = \sum_{k=0}^{p} h_k z^{-k} \qquad (1)$$

Note that if $h_0=0$ and $d(n)=x(n)$, the filter in Figure 2 becomes the one-step forward linear predictor illustrated in Figure 3(a). Removing the predictable components from x(n) yields the forward prediction error sequence $e^d_p(n)$. The corresponding transfer function of the forward prediction error filter is given by

$$A(z) = \sum_{k=0}^{p} a_k z^{-k} \quad , \quad a_0 = 1 \quad . \qquad (2)$$

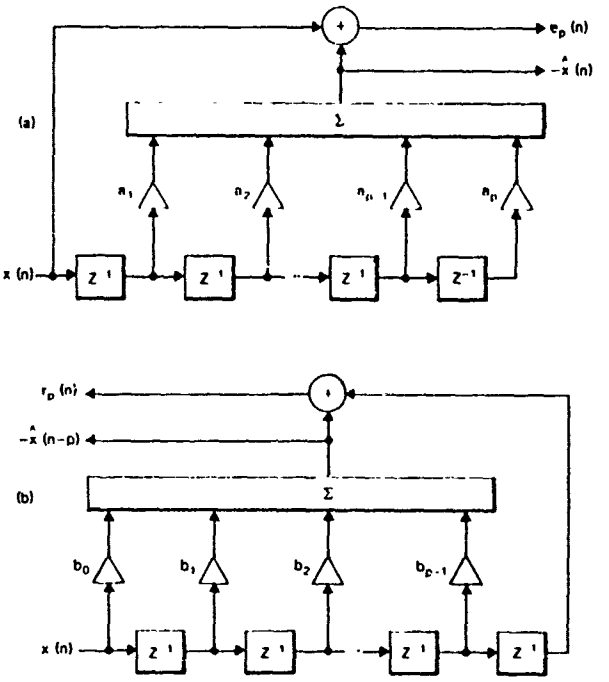

Figure 3. (a) One-step forward prediction error filter.
(b) One-step backward prediction error filter.

A companion to Figure 3(a) is the one-step backward linear predictor (coefficients $b_0, b_1, \ldots, b_{p-1}$) shown in Figure 3(b) along with the backward prediction error sequence $r_p(n)$.

The forward and backward linear predictors can be realized equivalently in the form of a lattice structure. Shown in Figure 4, the lattice parameters K^e_i and K^r_i are known either as reflection coefficients or partial correlation coefficients. The $e_i(n)$ and $r_i(n)$ are the ith order forward and backward prediction error sequences, respectively. Thus, the pth order linear predictor is created on a stage-by-stage basis a single order at a time.

As shown in Figure 5, the lattice realization of the forward and backward linear predictors can be embedded in the joint process structure. Additional parameters K^d_i weight the backward prediction error residuals $r_i(n)$. As with the lattice itself, the pth order joint process structure is created on a stage-by-stage basis a single order at a time.

A continuously adapting approach to the realization of the time varying, complex joint process structure is summarized

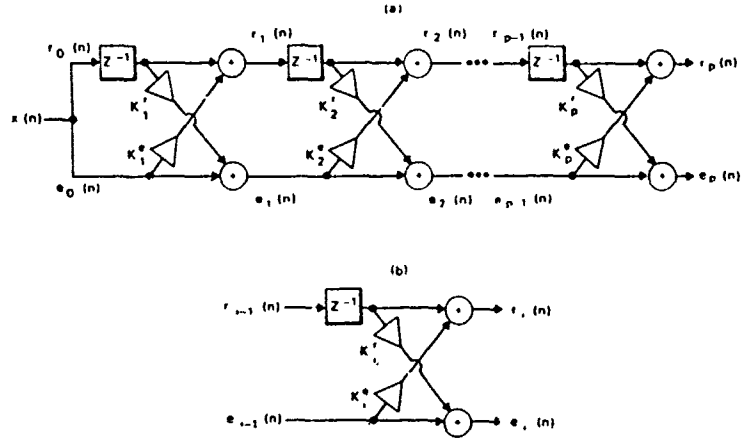

Figure 4. (a) Forward and backward prediction error filters. (b) The ith stage of the lattice.

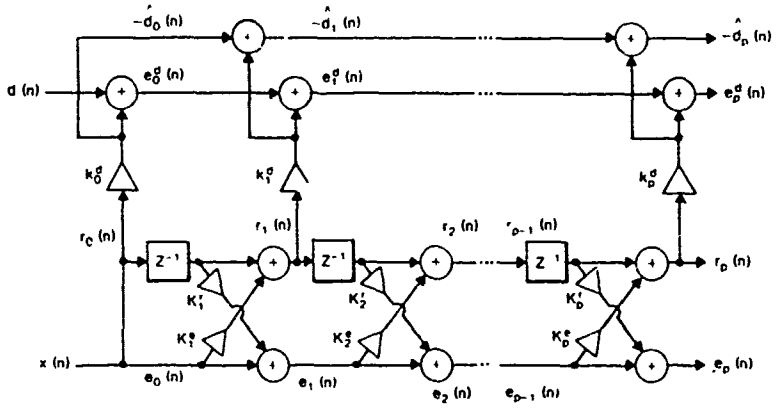

Figure 5. Lattice realization of the joint process structure.

below. The joint complex least-squares lattice (JCLSL) is based on a recursive in time solution for the filter whose transfer function is H(z). Bounded by [0,1], a parameter α is found in the algorithm which adjusts the time constant of its exponentially decaying memory of past data. Large α's imply short time constants. Additional material related to this algorithm can be found in [1-5] and the references cited therein.

The least squares lattice algorithm is summarized as follows (see Figure 5):

Initialization ($i = 0, 1, \ldots, p$)

$$r_i(-1) = 0 \quad , \quad i \neq p \tag{3a}$$

$$E_i^r(-1) = \varepsilon_{JCLSL} \quad , \quad \varepsilon_{JCLSL} = 0.001 \text{ and } i \neq p \tag{3b}$$

$$\Delta_i(-1) = 0 \quad , \quad i \neq 0 \tag{3c}$$

$$b_k^{(i)}(-1) = 0 \quad , \quad 0 \leq k \leq i-1 \quad , \quad i \neq 0, \text{ and } i \neq p \tag{3d}$$

$$\gamma_{i-1}(-1) = 0 \quad , \quad i \neq p \tag{3e}$$

$$K_i^d(i-1) = 0 \tag{3f}$$

Time update ($n \geq 0$)

$$e_o(n) = r_o(n) = x(n) \tag{3g}$$

$$E_o^e(n) = E_o^r(n) = (1 - \alpha_{JCLSL}) E_o^r(n-1) + |x(n)|^2 \tag{3h}$$

$$\gamma_{-1}(n) = 0 \tag{3i}$$

$$e_{-1}^d(n) = d(n) \tag{3j}$$

Order update ($i = 0, 1, \ldots, p$)

Lattice

$$\Delta_i(n) = (1 - \alpha_{JCLSL})\ \Delta_i(n-1) - \frac{e_{i-1}(n)r^*_{i-1}(n-1)}{1 - \gamma_{i-2}(n-1)} \quad , \quad i \neq 0 \tag{3k}$$

$$K^e_i(n) = \Delta^*_i(n) \ / \ E^e_{i-1}(n) \quad , \quad i \neq 0 \tag{3l}$$

$$K^r_i(n) = \Delta_i(n) \ / \ E^r_{i-1}(n-1) \quad , \quad i \neq 0 \tag{3m}$$

$$e_i(n) = e_{i-1}(n) + K^r_i(n)r_{i-1}(n-1) \quad , \quad i \neq 0 \tag{3n}$$

$$r_i(n) = r_{i-1}(n-1) + K^e_i(n)e_{i-1}(n) \quad , \quad i \neq 0 \tag{3o}$$

$$E^e_i(n) = E^e_{i-1}(n) - \left|\Delta_i(n)\right|^2 / \ E^r_{i-1}(n-1) \quad , \quad i \neq 0 \tag{3p}$$

$$E^r_i(n) = E^r_{i-1}(n-1) - \left|\Delta_i(n)\right|^2 / \ E^e_{i-1}(n) \quad , \quad i \neq 0 \tag{3q}$$

$$\gamma_{i-1}(n) = \gamma_{i-2}(n) + \left|r_{i-1}(n)\right|^2 / \ E^r_{i-1}(n) \quad , \quad i \neq 0 \tag{3r}$$

$$\Delta^d_i(n) = (1 - \alpha_{JCLSL})\Delta^e_i(n-1) - \frac{e^d_{i-1}(n)r^*_i(n)}{1 - \gamma_{i-1}(n)} \tag{3s}$$

$$K^d_i(n) = \frac{\Delta^d_i(n)}{E^r_i(n)} \tag{3t}$$

$$e_i^d(n) = e_{i-1}^d(n) + K_i^d(n) r_i(n) \tag{3u}$$

Predictors

$$a_i^{(i)}(n) = K_i^r(n) \tag{3v}$$

$$b_o^{(i)}(n) = K_i^e(n) \tag{3w}$$

$$a_k^{(i)}(n) = a_k^{(i-1)}(n) + K_i^r(n) + b_{k-1}^{(i-1)}(n-1) \qquad 1 \leq k \leq i-1 \tag{3x}$$

$$b_k^{(i)}(n) = b_{k-1}^{(i-1)}(n-1) + K_i^e(n) \; a_k^{(i-1)}(n) \tag{3y}$$

3.0 APPLICATION EXAMPLES

3.1 Prewhitening

As an example of a single channel problem, the prewhitening of acoustic reverberation will be considered. The results of processing a ping selected from an experimental ocean reverberation data set will be used for illustration. Of interest are: (1) the inputs to the prewhitening filters, (2) the prewhiteners themselves, and (3) the outputs of the prewhitening filters. The first 0.3 s of the complex basebanded ping under study has been set to zero so that transmit pulse leakage into the receiver at the time of data collection would not influence the processing. Since the goal of a prewhitening filter is to produce an output with a 'white' spectrum, it follows that the inverse of the spectrum of the prewhitening filter is an estimate of the spectrum of the input time series. Such time-evolving spectral plots will be compared with conventional range-Doppler maps of the input time series.

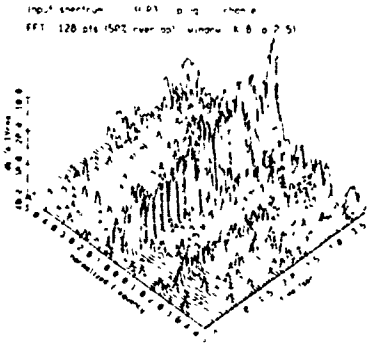

Figure 6.

Plots characterizing the performance of the complex least-squares lattice prewhitening structure are provided in the following order. First, Figure 6 is a conventional range-Doppler map of the ping under study. Then, a set of plots explores the characteristics of the prewhitening structure (Figures 7-12). The plots are presented in horizontal pairs - the plot on the left being the inverse of the prewhitening filter (an adaptive spectral estimate) and the plot on the right being the conventional range-Doppler map of the output of the prewhitening filter.

Trade-offs are illustrated as a function of the adaptation rate parameter (α). The values of α were chosen as follows. First, a mid-range value of α was determined. Then, values an order of magnitude larger and an order of magnitude smaller were added to the list of cases to process.

3.2 Surface Reverberation Rejection

As an example of a dual channel problem, sea surface reverberation rejection will be considered. In an active sonar system, transmitted energy reflected off the sea surface typically is discriminated against by the sidelobe characteristic of the receiving transducer. However, even though attenuated, this energy still can be a significant contributor to the noise background level. Here, an adaptive joint process structure is used which rejects boundary reverberation by taking advantage of the spatial separation between returning echoes of interest and transmitted energy reflected off the sea surface [6-7].

The results of processing another ping selected from the the experimental ocean reverberation data set mentioned above now will be presented. The sonar transducer consisted of a number of individual elements. For this ping, row sums of the elements were available. The primary channel signal (d(n) in

Figures 2 and 5) was obtained as a simple sum of these row sums (i.e. a forward looking beam). The reference channel signal (x(n) in Figures. 2 and 5) was obtained by differencing two adjacent rows (i.e. a beam with a null in the forward looking direction and large lobes towards the surface and the bottom).

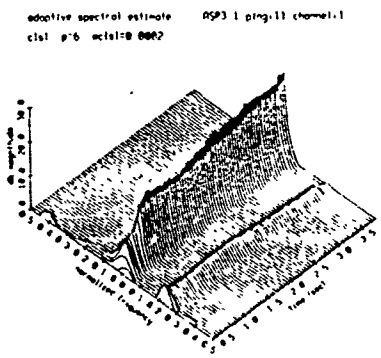

Figure 7.

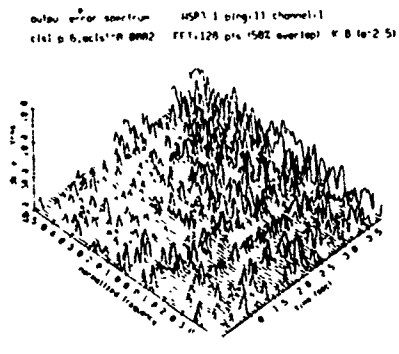

Figure 8.

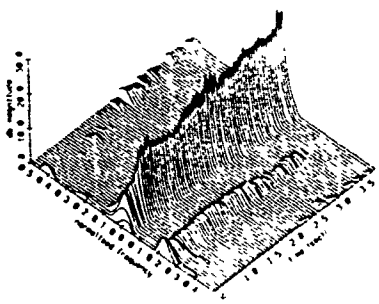

Figure 9.

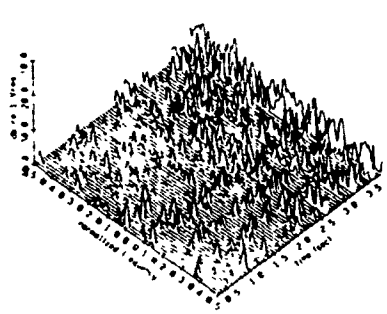

Figure 10.

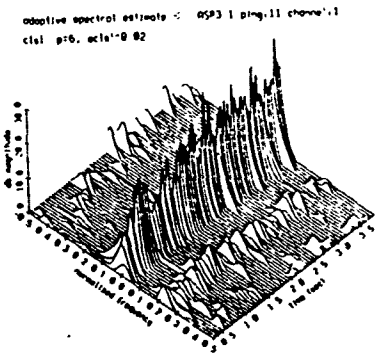

Figure 11.

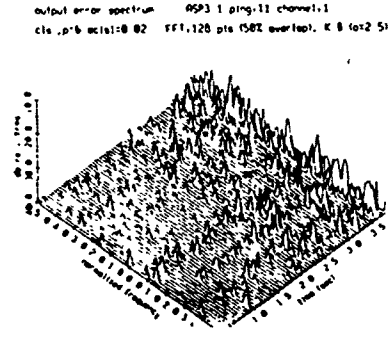

Figure 12.

The corresponding input and output range-Doppler maps for the joint process structure are provided in Figures 13-15. Both the primary and reference channel's range-Doppler maps are heavily contaminated by surface reverberation. In contrast, the output range-Doppler map shows a substantial reduction in this surface reverberation contamination.

4.0 SUMMARY

The application of adaptive least-squares lattice structures to problems in underwater acoustics has been discussed. The prewhitening of acoustic reverberation data was used as an illustration of a single channel problem. Then, sea surface reverberation rejection was used as an illustration of a dual channel problem.

ACKNOWLEDGEMENTS

This work was supported by the Office of Naval Research, Code 411, and by the Naval Sea Systems Command, under subcontract from the Applied Research Laboratory, The Pennsylvania State University, State College, PA.

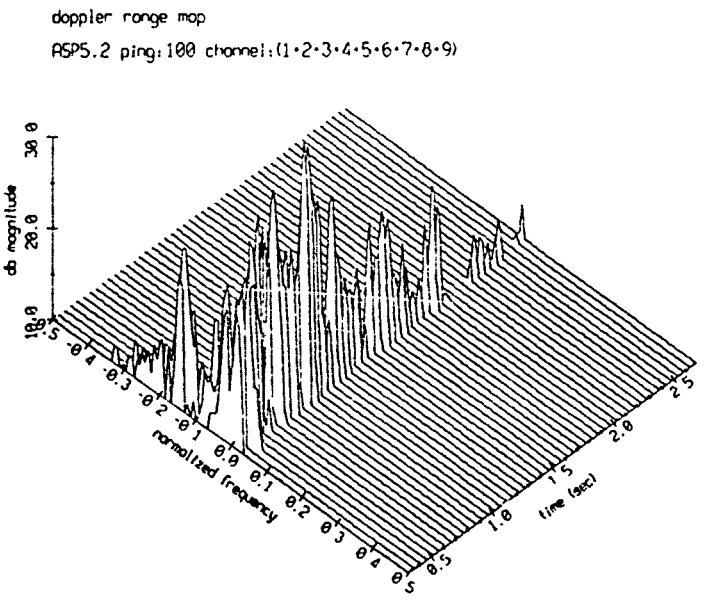

Figure 13.

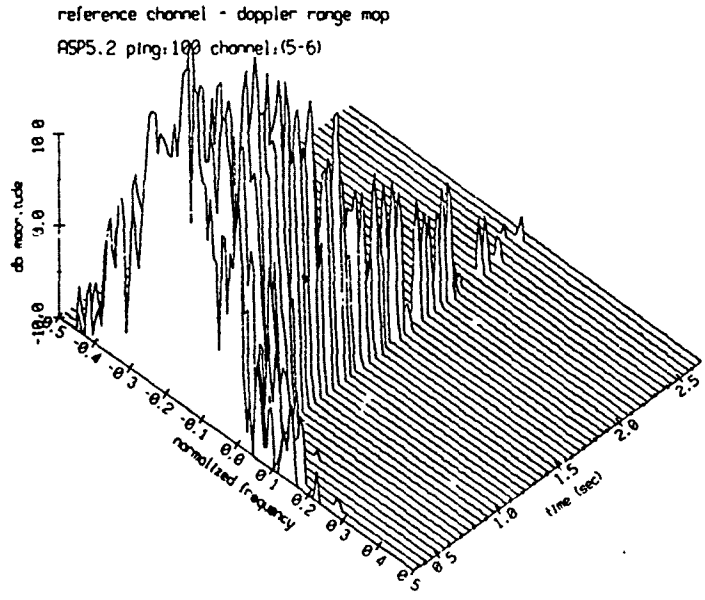

Figure 14.

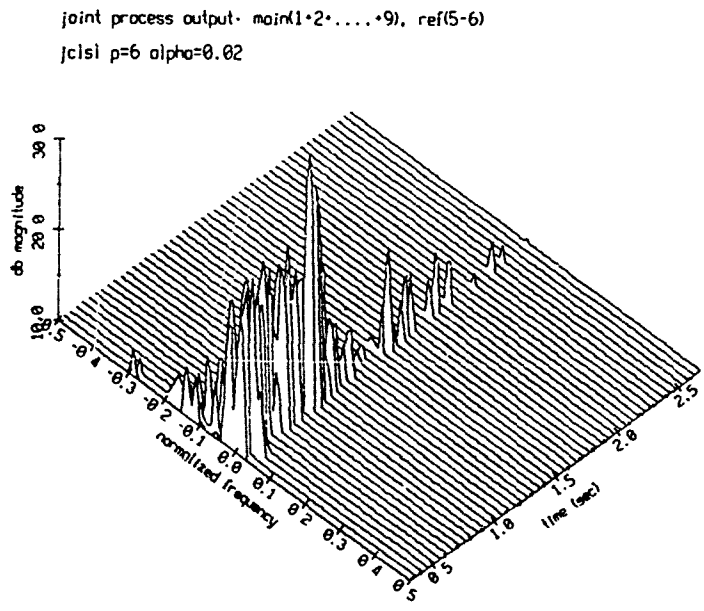

Figure 15.

REFERENCES

[1] D.T.L. Lee, "Canonical Ladder Form Realizations and Fast Estimation Algorithms," Ph.D. dissertation, Stanford University (August 1980).

[2] W.S. Hodgkiss and J.A. Presley, "Adaptive tracking of multiple sinusoids whose power levels are widely separated," IEEE Trans. Acoust., Speech, Signal Processing, vol. ASSP-29, pp. 710-721 (June 1981).

[3] W.S. Hodgkiss and J.A. Presley, "The complex adaptive least-squares lattice," IEEE Trans. Acoust., Speech, Signal Processing, vol. ASSP-30, pp. 330-333 (April 1982).

[4] B. Friedlander, "Lattice Methods for Spectral Estimation," Proc. IEEE 70(9), pp. 990-1017 (1982).

[5] B. Friedlander, "System Identification Techniques for Adaptive Noise Cancelling," IEEE Trans. Acoust., Speech, Signal Processing, ASSP-30(5), pp. 699-709 (1982).

[6] B. Widrow, et al, "Adaptive Noise Cancelling: Principles and Applications," Proc. IEEE 63(12): 1692-1716 (1975).

[7] W. Gabriel (Ed), "Special Issue on Adaptive Antennas," IEEE Trans. Antennas and Propagation, AP-24(5) (September 1976).

DISCUSSION*

Comment J W. R. Griffiths

Would you comment on the computational complexity of adaptive lattice structures?

Reply W S Hodgkiss

The lattice structure naturally falls out of the solution to the least-squares problem At the heart of things is Levinson's algorithm which has computational complexity on the order of p^2 for a p-stage filter.

Comment C van Schooneveld

What is the loss of preformance due to pursuing this scheme of adaptive beamforming as apposed to an approach which is "optimal" from a decision-theoretic standpoint?

Reply W S Hodgkiss

Your question points to an area deserving of additional work. In general, comparisons have not been made of performance between an adaptive structure (such as reported here) which appears to be doing a good job "locally" and a globally optimal processor working on the same problem.

Comment G. C. Carter

It is apparent that the overall cancellation ratio (conventional beam output power divided by adaptive beam output power) is rarely more than a few dB. Is the gain worth the effort?

Reply W S Hodgkiss

The benefits of adaptive beamforming are selective. In the results presented, not all regions of the range-Doppler map were affected equally For example, a large spike of reverberation coming in a sidelobe of the transducer was removed as well as a significant amount of the boundary reverberation beyond 1.2 s in range Whether the gain is worth the effort or not is critically dependent on the actual problem being worked on

*Paper presented by W S Hodgkiss

Boundary reverberation rejection via constrained adaptive beamforming

Dimitri Alexandrou
Marine Physical Laboratory, Scripps Institution of Oceanography, University of California, San Diego, La Jolla, California 92093

(Received 15 May 1986; accepted for publication 8 May 1987)

The problem of selective reverberation cancellation, whereby both "signal" and "noise" are constituent components of the received reverberation process, is the focus of this article. The proposed solution involves the application of a constrained adaptive beamforming technique. The "prewindowed" deterministic least-squares lattice filter is used as the central adaptive element. Constraints are in the form of simple spatial filtering prior to adaptation. The spatial correlation characteristics of volume and boundary reverberation are found to be directly applicable in a reverberation cancellation context. Experimental verification is offered by processing reverberation data from a shallow-water deployment of an active sonar system. It is shown that the boundary reverberation components can be effectively suppressed while preserving the volume return. Computer simulations of the experiment offer additional insight into the adaptation process.

PACS numbers: 43.60.Gk, 43.30.Gv, 43.30.Vh

INTRODUCTION

The ocean abounds with objects that can intercept and reradiate acoustic energy. Suspended sediment, organic detritus, air bubbles, plankton, fish, and minute discontinuities in the thermal structure are all capable of redirecting sound. Irregularities of the sea surface and the ocean floor are also significant contributors to this reradiation of sound known as *scattering*. The composite echo from all scatterers is known as *reverberation*. When the objective is signal detection, reverberation is clearly a form of noise. However, reverberation can also be a valuable information-bearing signal; it offers information about the nature and distribution of the scatterers and to the extent that the scatterers are influenced by a fluid process, about the process itself. The information, if properly extracted, can be used to quantify fishery species of commercial interest (Holliday, 1974), to examine planktonic communities (Greenblatt, 1980), to monitor pollution in industrial dumping sites (Orr and Hess, 1978), to identify ocean bottom types (de Moustier, 1985), or for remote sensing of oceanic fluid processes (Pinkel, 1981). As reverberation is being reevaluated in terms of its information content, so must the signal processing techniques used vis-a-vis reverberation be reconsidered. For instance, rather than indiscriminate reverberation suppression, the situation may call for the extraction, from a composite reverberation return, of the component created by the class of scatterers associated with the process of interest. In this scenario, "signal" and "noise" are both constituent components of the received reverberation process. Here, we offer a potential solution to this signal processing problem based on an *adaptive beamforming* technique.

As their name implies, *adaptive* filters are capable of responding to changing conditions through a rudimentary "learning" process. The filter parameters adjust themselves under the guidance of an appropriate cost function and track the evolving characteristics of the input signal(s). These structures grew out of the demand for systems capable of operating in uncertain, time-varying environments and were made possible by the increasing availability of computational power. They can be viewed as realizable approximations to optimal Wiener filters when only a single sample function of the "signal" and "noise" processes is available. In this case, the optimum filtering problem may be approached from a statistical viewpoint by invoking stationarity and ergodicity and performing time averaging, or through a deterministic least-squares formulation. Both solutions can be implemented either in a block-processing or a time recursive mode and both give rise to efficient *lattice structures*. Nonstationary processes are treated as locally stationary by restricting the time interval over which optimization is performed. An adaptive filter solves the Wiener problem, or its deterministic counterpart, over the restricted optimization interval controlled by an *adaptation coefficient*, which provides for a "fading" of past information in favor of recent values. Adaptive algorithms can be used to control the element weights of an array, changing its beam pattern in an optimum manner to reject interference. This class of adaptive filtering is known as *adaptive beamforming*.

I. CONSTRAINED ADAPTIVE BEAMFORMING

Conventional arrays are usually designed under the assumption that noise is spatially disorganized. These fixed-weight arrays suffer a degradation of performance in the presence of directional interference possessing a degree of spatial coherence. Such interference may be due to natural sources or reverberation returns. Other factors, such as array motion, multipaths, and constantly changing interference characteristics contribute to further deterioration. Adaptive arrays, on the other hand, are capable of reducing

 0001-4966/87/101274-17$00.80 © 1987 Acoustical Society of America

or eliminating directional noise components and of responding to changing conditions by adjusting their pattern response according to an appropriately chosen error criterion. In general, adaptive arrays are in the form of a space-time filter. The exact manner in which control of the available spatial and temporal degrees of freedom is relegated to the adaptive processor and the choice of a performance measure depends largely on the objectives and priorities of the specific application. A good tutorial introduction to the adaptive array problem is given by Gabriel (1976). Our objective here is to utilize the general adaptive algorithms derived under the minimum mean-square error (MMSE) criterion, in conjuction with the adaptive noise canceling (ANC) principle, in order to eliminate reverberation interference entering through the sidelobes and the mainlobe edges of the receiving array.

In an adaptive array application, it is important to utilize all available *a priori* information about signal and interference in order to ensure signal preservation at the output. Constraints may be incorporated into the adaptive algorithm to maintain a chosen frequency response in a desired direction (Frost, 1972). "Pilot" signals, simulating actual signals of interest, have also been used to describe a desired "main" look direction through a two-mode adaptation process (Widrow *et al.*, 1967). An alternative is to impose preadaptation constraints in the time, space, and frequency domains (Applebaum and Chapman, 1976). Restrictions may be applied in the time domain by allowing the array to adapt only when no signal is present; in the frequency domain, by allowing adaptation only to energy received outside the signal band; or preadaptation spatial filtering may be used to remove the signal from the reference channel, thus protecting it from cancellation. Such prefiltering may range from complete conventional beamforming [Fig. 1(a)] to simple element-to-element subtraction [Fig. 1(b)]. The former can be applied only when the spatial characteristics of the interference, as well as the signal, are known and requires an external steering mechanism. The latter is more appropriate when the directional characteristics of the interference are unknown, or variable, and results in (constrained) spatially adaptive cancellation beams.

Such spatial prefiltering operations, by eliminating the signal of interest from the reference channel(s), in effect place constrained adaptive beamforming in the context of ANC. This approach affords us the flexibility of using any efficient solution to the general filtering problem as the adaptive processor controlling the array element weights.

A. The adaptive noise canceling (ANC) concept

The noise canceling solution stems from the following dual-channel filtering problem: Given two discrete time stochastic processes $x(n)$, $d(n)$, estimate the second process (primary signal) by operating on the first process (reference signal). The MMSE solution is given by

$$R_{dx}(n,k) = \sum_{i=0}^{p} F_p^{(i)}(n) R_{xx}(n,k), \quad n-p<k<n, \quad (1)$$

where $F_p^{(i)}$ is a linear, causal filter of order p and R_{xx}, R_{dx} are the autocorrelation function of the reference signal and the cross-correlation function between the primary and reference signals, respectively.

The set of circumstances giving rise to the noise canceling concept is illustrated in Fig. 2(a). The primary channel consists of the signal s corrupted by a form of additive noise n_0 and the reference channel consists of a process n_1 related in some unknown way to the primary noise. The key requirement is that the signal be uncorrelated with both the primary noise and the reference process:

$$R_{sn_0} = 0, \quad R_{sn_1} = 0.$$

We then have

$$R_{dx} = R_{n_0 n_1},$$

which leads to the noise canceling solution as a special case of the general filtering problem solution:

$$R_{n_0 n_1}(n,k) = \sum_{i=0}^{p} F_p^{(i)}(n) R_{n_1 n_1}(n,k), \quad n-p<k<n. \quad (2)$$

Solving the filtering problem in this setting is equivalent to producing the best MMSE estimate of the primary noise process. The ANC output, obtained by subtracting this estimate from the primary input, will consist of the signal component s plus a residual error $n_0 - \hat{n}_0$.

A more detailed model for the noise canceling structure is shown in Fig. 2(b). The "mismatch" between the primary and reference inputs is represented by a linear transfer function $H(z)$. Additional uncorrelated noise components m_0 and m_1 are included in the two channels. This particular model, which is representative of many situations of practical interest, has been studied in detail by Widrow *et al.* (1975), who determined that the uncorrelated noise components have a deleterious effect on cancellation. Other factors limiting ANC performance are the presence of signal components in the reference channel and, somewhat surprisingly, a high signal-to-noise ratio in the primary channel.

B. Adaptive algorithms

Rather than evolving from a general mathematical premise, early adaptive filters were designed to solve specific real-time engineering problems (e.g., Glaser, 1961; Davisson, 1966; Anderson, 1969). The work of Widrow and Hoff (1960) produced the first generalized adaptive structure, based on the method of steepest descent, known as the least mean-square (LMS) algorithm. The LMS has been used as the central adaptive processor in applications such as adaptive array processing (Widrow *et al.*, 1967; Griffiths, 1969; Frost, 1972), adaptive modeling (Schade, 1971), adaptive channel equalization (Lucky, 1965), and adaptive noise canceling (Widrow *et al.*, 1975). Adaptive *lattice* structures were shown to outperform the LMS by Satorius and Alexander (1979) and Hodgkiss and Presley (1981) in channel equalization and frequency tracking applications, respectively. Lattice joint-process filters suitable for noise canceling have been suggested (Griffiths, 1978), but few applications in cases of practical interest have been reported (e.g., Alexandrou, 1985b).

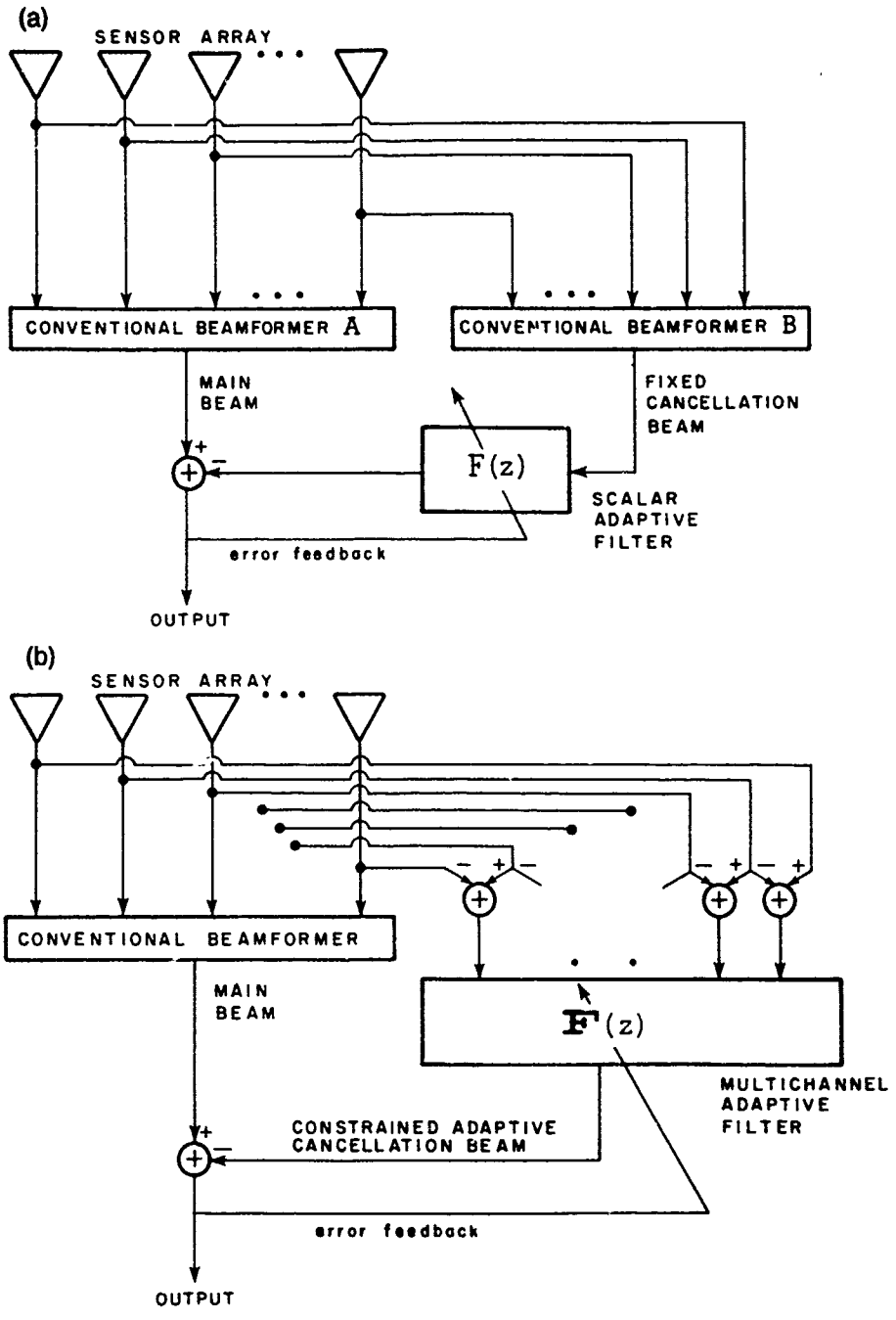

FIG. 1. Adaptive beamforming. (a) Fixed, preformed reference beam. An external steering mechanism is required to track the changing directional properties of the interference. (b) Constrained adaptive beamformer. The multichannel adaptive filter weights the constrained elements to form a spatially adaptive reference beam.

II. DETERMINISTIC LEAST-SQUARES ERROR (LSE) SOLUTIONS

The development of the LMS and its successful application in a plethora of experimental settings have demonstrated that adaptive structures of considerable diversity can be realized through a central adaptive estimator which is a practical implementation of a Wiener filter. In applications of practical interest, where real-time processing is of the essence, only a single sample function of the underlying random process is typically available and time averaging must be used. When wide sense stationarity (WSS) holds at least locally and ergodicity can be safely invoked this will still lead to the optimum solution. These assumptions form the basis for the development of *stochastic approximation* adaptive algorithms such as the LMS and the gradient lattice (GRL) filter (Makhoul, 1978). During transition periods, when the statistics of the signal change drastically, all stochastic approximation solutions are clearly suboptimal. In addition, the misadjustment noise of the gradient methods is often a limiting factor on the algorithm convergence speed.

An alternative to the stochastic approximation methods is the deterministic least-squares approach. When WSS holds, the solutions derived through this approach perform

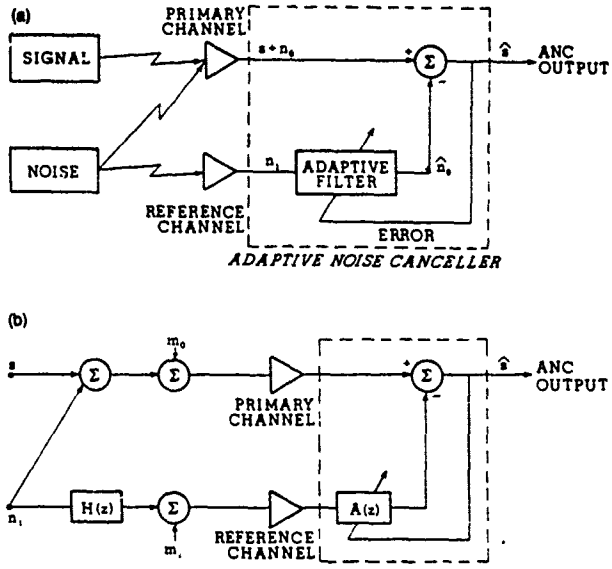

FIG. 2. The adaptive noise cancelling concept. (a) General structure, (b) Widrow *et al*'s (1975) linear model. Here, m_0 and m_1 represent uncorrelated additive noise components in the two channels. The "mismatch" between the primary and reference channels, expressed by $H(z)$, must be compensated for by the adaptive filter transfer function $A(z)$.

identically to their stochastic (time average) counterparts. However, they enjoy an important advantage in that they continue to be optimum (in a deterministic least-squares sense) even during abrupt changes in the signal statistics. This contributes to transient behavior superior to the gradient solutions and makes the least-squares structures excellent candidates for our choice of adaptive algorithm. For instance, an algorithm of this class was shown to converge successfully in the presence of amplitude transients that drove the LMS and the GRL to instability (Alexandrou, 1985a). This is relevant here because the onset of boundary reverberation in a volume reverberation backround can readily amount to an abrupt intensity "step."

The deterministic least-squares problem is formulated as follows: Given two discrete time series,

$$\{x(n),d(n)\}, \quad N_i \leqslant n \leqslant N_f,$$

of dimension m and l, respectively, we form the estimate of $d(n)$:

$$\hat{d}(n) = \sum_{j=0}^{p} F_j^{(p)}(n)x(n-j) = \mathbf{F}_p^T(n)\mathbf{x}_{(n\,n-p)},$$

where

$$\mathbf{F}_p^T = (F_p^{(0)}, F_p^{(1)},\ldots,F_p^{(p)})$$

$$\mathbf{x}_{(n\,n-p)} = \begin{pmatrix} x(n) \\ x(n-1) \\ \cdot \\ \cdot \\ \cdot \\ \cdot \\ x(n-p) \end{pmatrix}$$

and with

$$\epsilon_{p,i,f}(n) = d(n) - \hat{d}(n)$$

we seek to minimize

$$\xi_p^d(i,f) = \mathrm{tr}\sum_{i}^{f} \epsilon_{p,i,f}(n)\epsilon_{p,i,f}^H(n),$$

where i,f will be specified later ($N_i \leqslant i < N_f$, $i < f \leqslant N_f$).

The LSE solution to the filtering problem is easily obtained through the projection theorem and is given by

$$\mathbf{F}_p^T(i,f)\mathbf{R}_{x,p}(i,f) = \mathbf{R}_{dx,p}(i,f), \tag{3a}$$

where

$$\mathbf{R}_{x,p}(i,f) = \sum_{n=i}^{f} \mathbf{x}_{(n\,n-p)}\mathbf{x}_{(n\,n-p)}^H = \mathbf{X}_p(i,f)\mathbf{X}_p^H(i,f),$$

with

$$\mathbf{X}_p(i,f) = \begin{pmatrix} x(i) & \cdots & x(f) \\ \cdots & \cdots & \cdots \\ \cdots & \cdots & \cdots \\ x(i-p) & \cdots & x(f-p) \end{pmatrix},$$

$$\mathbf{R}_{dx,p}(i,f) = \mathbf{d}_{(i,f)}^T\mathbf{X}_p^H(i,f).$$

The minimum least-squares error is

$$E_p^d(i,f) = \min_{\{F\}}\xi_p^d(i,f)$$
$$= R_{d,00}(i,f) - \mathbf{F}_p^T\mathbf{R}_{dx,p}^H(i,f). \tag{3b}$$

Similarly, the LSE one-step predictor is given by

$$\mathbf{A}_p^T(i,f)\mathbf{R}_{x,p}(i,f) = [E_p^e(i,f),0,\ldots,0], \tag{4}$$

where

$$\mathbf{A}_p^T(i,f) = [I_m, A_1^{(p)}(i,f),\ldots,A_p^{(p)}(i,f)],$$
$$E_p^e(i,f) = R_{x,00}(i,f) - \mathbf{A}_p^T\mathbf{Q}_{x,p}(i,f),$$
$$\mathbf{Q}_{x,p} = \sum_{n=i}^{f} x(n)\mathbf{x}_{(n-1\,n-p)}^H.$$

Note that the exact form of $\mathbf{X}_p(i,f)$ depends on the choice of i and f. The following choices are most commonly made, resulting in *sample correlation* matrices $\mathbf{R}$ with different symmetry and/or shift invariance properties. Such properties are crucial to the development of algorithmic implementations of the above solutions.

(1) Prewindowed case:

$$i = N_i, \quad f = N_f.$$

(2) Nonwindowed case:

$$i = N_i + p, \quad f = N_f.$$

(3) Prewindowed and postwindowed cases:

$$i = N_i, \quad f = N_f + p.$$

A. The "prewindowed" least-squares lattice (LSL)

In this case, for $N_i = 0$ and $N_f = N$, the *sample correlation* matrix $\mathbf{R}$ of order p is of the form

$$\mathbf{R}_{p,N} = \mathbf{X}_{p,N}\mathbf{X}_{p,N}^H,$$

where

$$\mathbf{X}_{p,N} = \begin{pmatrix} x(0) & \cdots & x(p) & \cdots & x(N) \\ 0 & \cdots & \cdots & \cdots & \cdots \\ 0 & 0 & x(0) & \cdots & x(N-p) \end{pmatrix}.$$

Note that $\mathbf{R}_{p,N}$ is not Toeplitz, but it consists of a product of two (upper and lower triangular) Toeplitz matrices and might be thought of as being "near Toeplitz." In fact, it

falls within the class of the so-called *α-stationary* matrices which can be expressed as

$$\mathbf{R} = \mathbf{T} + \sum_{i=1}^{\alpha} \sigma_i \mathbf{U}_i \mathbf{U}_i^H, \quad \sigma_i = \pm 1, \tag{5}$$

where $\mathbf{T}$ is Toeplitz and the $\{\mathbf{U}_i\}$ are upper triangular Toeplitz matrices (Friendlander *et al.*, 1979). These matrices, also known as "low shift rank" matrices, have certain shift-invariance properties that lead to efficient recursive solutions. Specifically in the prewindowed case, $\mathbf{R}_{p,N}$ is *α-stationary* with $\alpha = 2$ and satisfies the following recursive identities:

order and time update.

$$\mathbf{R}_{x,p}(N) = \begin{pmatrix} \mathbf{R}_{x,00}(N) & \mathbf{Q}_{x,p}(N) \\ \mathbf{Q}_{x,p}^H(N) & \mathbf{R}_{x,p-1}(N-1) \end{pmatrix}, \tag{6a}$$

order update:

$$\mathbf{R}_{x,p}(N) = \begin{pmatrix} \mathbf{R}_{x,p-1}(N) & \mathbf{V}_{x,p}^H(N) \\ \mathbf{V}_{x,p}(N) & \mathbf{R}_{x,pp}(N) \end{pmatrix}, \tag{6b}$$

time update:

$$\mathbf{R}_{x,p}(N) = \mathbf{R}_{x,p}(N-1) + \mathbf{x}_{(N-p,N)}\mathbf{x}_{(N-p,N)}^H, \tag{6c}$$

where

$$\mathbf{V}_{x,p}(N) = \sum_{n=0}^{N} x(n-p)\mathbf{x}_{(n-1,n-p)}^H,$$

and all other quantities are as previously defined. These identities form the basis for the exact order- and time-update recursions for the prewindowed prediction-error LSL. The joint-process LSL can be obtained through an embedding technique, whereby the *joint* sample correlation matrix $\mathbf{R}_{z,p}(N)$ is defined as

$$\mathbf{R}_{z,p} = \mathbf{Z}_p(N)\mathbf{Z}_p^H(N),$$

where

$$\mathbf{Z}_p(N) = \begin{pmatrix} d(0) & \cdots & d(p) & \cdots & d(N) \\ x(0) & \cdots & x(p) & \cdots & x(N) \\ 0 & \cdots & \cdots & \cdots & \cdots \\ 0 & 0 & x(0) & \cdots & x(N-p) \end{pmatrix}.$$

Then, the filtering normal equations can be reexpressed in terms of $\mathbf{R}_{z,p}(N)$ as follows:

$$\mathbf{F}_{jp}^T \mathbf{R}_{z,p}(N) = [E_p^d(N), 0, \ldots, 0], \tag{7}$$

where

$$\mathbf{F}_{jp}^T(N) = [I_1, \mathbf{F}_p^T(N)].$$

Here, $\mathbf{R}_{z,p}$ has shift properties similar to $\mathbf{R}_{x,p}$. The two sets of recursions can be combined to concurrently solve the forward prediction, backward prediction, and filtering problems, giving rise to the joint-process LSL. The needed algebraic manipulations are given by Lee (1980). A schematic diagram of the scalar LSL is given in Fig. 3.

1. Exponential weighting

An adaptive version of the LSL filter can be easily derived by introducing an exponential "window" in the error norm. Specifically, one may choose to minimize

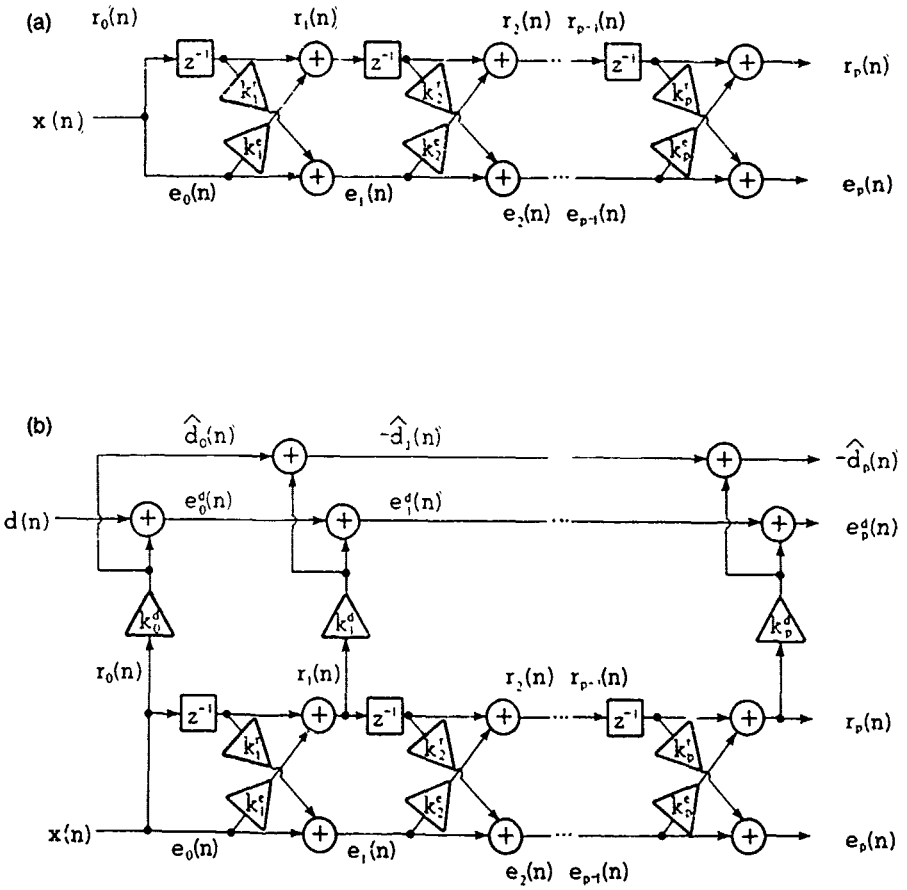

FIG. 3 The scalar LSL filter. (a) Prediction error (whitening) filter; k_i^r and k_i^r are the forward and backward reflection (PARCOR) coefficients; $e_i(n)$ and $r_i(n)$ are the ith-order forward and backward prediction error sequences. (b) Joint-process filter; the $r_i(n)$ constitute an orthogonal basis for the reference process $x(n)$ and are weighted by the cross-channel coefficients k_i^d to produce an estimate of the primary process $d(n)$.

$$\xi_p^e(N) = \mathrm{tr} \sum_{n=0}^{N} (1-\alpha_{\mathrm{LSL}})^{N-n} \epsilon_{p,N}(n) \epsilon_{p,N}^H(n),$$

where α_{LSL} is a constant ≥ 0, so that past errors will have a smaller influence on the estimate. This constant "fade" factor is easily incorporated into the lattice recursions and controls the effective "averaging interval," i.e., the number of samples over which the algorithm solves the filtering problem at any given instant. This "effective" number of samples may be defined in terms of a "time constant" as follows:

$$(1-\alpha_{\mathrm{LSL}})^{N-n} = \exp - [(N-n)/N_{\mathrm{eff}}].$$

Therefore,

$$N_{\mathrm{eff}} = \min\{N, -1/\ln(1-\alpha_{\mathrm{LSL}})\}.$$

2. Summary of the LSL algorithm

The complex, multichannel, joint-process, exponentially weighted, prewindowed least-squares lattice algorithm is summarized as follows:

initialization ($i = 0, 1, \ldots, p$):

$$\mathbf{r}_i(-1) = 0, \quad i \neq p, \tag{8a}$$

$$\mathbf{E}_i^r(-1) = \epsilon \mathbf{I}_m, \quad i \neq p, \tag{8b}$$

$$\mathbf{\Delta}_i(-1) = 0, \quad i \neq 0, \tag{8c}$$

$$\gamma_{i-1}(-1) = 0, \quad i \neq p, \tag{8d}$$

time update ($n \geq 0$):

$$\mathbf{e}_0(n) = \mathbf{r}_0(n) = \mathbf{x}(n), \tag{8e}$$

$$\mathbf{E}_0^e(n) = \mathbf{E}_0^r(n) = (1-\alpha_{\mathrm{LSL}})\mathbf{E}_0^r(n-1) + \mathbf{x}(n)\mathbf{x}^H(n), \tag{8f}$$

$$\gamma_{-1}(n) = 0, \tag{8g}$$

$$\mathbf{e}_{-1}^d(n) = \mathbf{d}(n). \tag{8h}$$

order update ($i = 0, 1, \ldots, p$):

$$\mathbf{\Delta}_i(n) = (1-\alpha_{\mathrm{LSL}})\mathbf{\Delta}_i(n-1) - \frac{\mathbf{e}_{i-1}(n)\mathbf{r}_{i-1}^H(n-1)}{1-\gamma_{i-2}(n-1)}, \quad i \neq 0, \tag{8i}$$

$$\mathbf{K}_i^e(n) = \mathbf{\Delta}_i^H(n)\mathbf{E}_{i-1}^{-e}(n), \quad i \neq 0, \tag{8j}$$

$$\mathbf{K}_i^r(n) = \mathbf{\Delta}_i(n)\mathbf{E}_{i-1}^{-r}(n-1), \quad i \neq 0, \tag{8k}$$

$$\mathbf{e}_i(n) = \mathbf{e}_{i-1}(n) + \mathbf{K}_i^r(n)\mathbf{r}_{i-1}(n-1), \quad i \neq 0, \tag{8l}$$

$$\mathbf{r}_i(n) = \mathbf{r}_{i-1}(n-1) + \mathbf{K}_i^e(n)\mathbf{e}_{i-1}(n), \quad i \neq 0, \tag{8m}$$

$$\mathbf{E}_i^e(n) = \mathbf{E}_{i-1}^e(n) - \mathbf{\Delta}_i(n)\mathbf{E}_{i-1}^{-r}(n-1)\mathbf{\Delta}_i^H(n), \quad i \neq 0, \tag{8n}$$

$$\mathbf{E}_i^r(n) = \mathbf{E}_{i-1}^r(n-1) - \mathbf{\Delta}_i^H(n)\mathbf{E}_{i-1}^{-e}(n)\mathbf{\Delta}_i(n), \quad i \neq 0, \tag{8o}$$

$$\gamma_{i-1}(n) = \gamma_{i-2}(n) + \mathbf{r}_{i-1}^H(n)\mathbf{E}_{i-1}^r(n)\mathbf{r}_{i-1}(n), \quad i \neq 0, \tag{8p}$$

$$\mathbf{\Delta}_i^d(n) = (1-\alpha_{\mathrm{LSL}})\mathbf{\Delta}_i^d(n-1) - [\mathbf{e}_{i-1}^d(n)\mathbf{r}_i^H(n)]/[1-\gamma_{i-1}(n)], \tag{8q}$$

$$\mathbf{K}_i^d(n) = \mathbf{\Delta}_i^d(n)\mathbf{E}_i^{-r}(n), \tag{8r}$$

$$\mathbf{e}_i^d(n) = \mathbf{e}_{i-1}^d(n) + \mathbf{K}_i^d(n)\mathbf{r}_i(n). \tag{8s}$$

3. On the choice of adaptation coefficient

If WSS holds for all time, then $\alpha_{\mathrm{LSL}} = 0$ is the optimum choice and the time-invariant Wiener–Hopf solution is obtained. In cases of practical interest, local WSS is a more realistic assumption and the effective "averaging interval" is dictated by the time scale of variation of the signal statistics. Therefore, the lower limit of the adaptation coefficient α_{LSL} (or the upper limit of the allowable averaging interval) is set by the time scale over which local stationarity can be assumed. In the gradient descent algorithms (LMS.GRL) the upper bound of the adaptation coefficient is imposed by *misadjustment* noise, caused by excessively large steps in the gradient search process. In the case of the exact deterministic least-squares solution (LSL), there is no misadjustment error. The upper bound of α_{LSL} is strictly a question of statistical reliability.

Insight may be gained by considering the variance of the following cross-correlation estimate between two bandwidth-limited white noise processes $x(n)$ and $y(n)$:

$$\hat{R}_{xy}(k) = \frac{1}{N_{\mathrm{eff}}} \sum_{i=0}^{N_{\mathrm{eff}}} x(i)y(i+k), \tag{9}$$

where

$$N_{\mathrm{eff}} = -1/\ln(1-\alpha_{\mathrm{LSL}}).$$

The variance of the estimate is given by (see Bendat and Piersol, 1971)

$$\mathrm{var}[\hat{R}_{xy}(k)] = (1/N_{\mathrm{eff}})[R_{xx}(0)R_{yy}(0) + R_{xy}^2(k)]. \tag{10}$$

Equation (10) indicates that large, spurious cross-correlation values can be generated between two uncorrelated processes [$R_{xy}(k) = 0$] for sufficiently small N_{eff} and/or large autocorrelations within the two processes. Although direct comparison between this simple result and the behavior of the lattice parameters for arbitrary signals is not warranted, the LSL joint-process filter has been observed to obey this general rule. Specifically, the filter has shown a tendency toward cancellation of the primary channel when the primary and reference channels consisted of independent white noise sequences, for $\alpha_{\mathrm{LSL}} \geq 0.02$. This empirically derived value will be used as the upper bound for α_{LSL} throughout this article.

III. REVERBERATION IN THE CONTEXT OF ADAPTIVE BEAMFORMING

Oceanic reverberation is usually classified as volume, surface, and bottom reverberation. The scatterers responsible for volume reverberation are mostly biological in nature (Clay and Medwin, 1977). Inorganic particles are insignificant contributors and reflections from sound velocity microstructure are effectively masked by biological scattering (Kaye, 1978). Zooplankton such as copepods are the dominant source of volume scattering in the near-surface region. In deeper water, biological scatterers are often distributed within diffuse deep scattering layers (DSL) consisting of siphonophores, copepods, pteropods, euphausiids, and mesopelagic fish. Surface reverberation is generated by the entire spectrum of the rough air/sea interface and is a function

of wind speed and the transmitted frequency (Urick and Hoover, 1956; Chapman and Harris, 1962). Specular reflections from normally inclined wave facets and scattering from an isotropic layer of bubbles in the near surface have also been suggested as reverberation sources at high and low grazing angles, respectively (Medwin, 1966; Clay and Medwin, 1964). Bottom reverberation is an extremely complex phenomenon owing to the diversity of ocean floor types, lateral inhomogeneity, and potential contribution of subbottom layers. It appears that both particle size and bottom relief are important factors (McKinney and Anderson, 1964; Buckley and Urick, 1968).

The received backscattered return is typically a composite process with two or more reverberation types contributing at any given instant. This is especially true in shallow-water environments. Our objective here is to achieve selective reverberation cancellation, whereby the desired reverberation component is preserved and the rest suppressed or eliminated. In this context, the spatial correlation characteristics of the various reverberation components are critically important. Certain theoretical predictions of the point-scattering reverberation model provide valuable insight into the spatial correlation properties of surface, volume, and bottom reverberation, and point to an adaptive system configuration conducive to selective reverberation cancellation.

A. The point-scattering model of reverberation

According to the *point-scattering* model developed by Faure (1964), Ol'shevskii (1967), and Middleton (1967a, b, 1972a,b), reverberation is described as a random process constructed by a linear superposition of the individual echoes emanating from a large number of point reflectors located independently in a homogeneous medium. For a transmitted signal $s(t)$, the backscattered signal is represented by

$$r(t) = \sum_{i=1}^{n} a_i G_i(t) s[\alpha_i (t - t_i)]. \tag{11}$$

The returning echo from each scatterer, indexed by i, is delayed by t_i, the two-way travel time between the source and the ith scatterer. The a_i and α_i are random variables representing distributions of acoustic cross section and Doppler factor of the scatterers, respectively. For a monostatic sonar,

$$G_i(t) = g B_i^2(\mathbf{r}_i) F(t),$$

where g is a system gain factor, B_i^2 is the two-way beam pattern sensitivity in the direction of the ith scatterer, and $F(t)$ represents the two-way propagation loss.

Assuming that for a sufficiently large scattering region the mean scatterer density is constant, the number of scatterers n contributing to the reverberation return at any given time may be described as a Poisson random process. Based on this assumption, the second-order statistics of reverberation can be calculated for general experimental geometries, beam patterns, and transmitted signals.

B. Spatial correlation properties of reverberation

Spatial correlation expresses mathematically the fact that returns arriving from widely separated angular directions tend to add out of phase at spatially separated receivers. The geometry for the volume backscattered return is depicted in Fig. 4(a). The two receivers R_1 and R_2 are a distance s apart and vertically aligned. Volume reverberation arrives from a range of elevation and azimuthal angles determined by the directional characteristics of the transmitting and receiving arrays. For omnidirectional transmission and reception and narrow-band (quasiharmonic) transmitted signals, the spatial correlation coefficient of volume reverberation is (Ol'shevskii, 1967)

$$R_V(s) = \sin(ks)/ks, \tag{12a}$$

with

$$k = 2\pi/\lambda = 2\pi f/c,$$

where f is the transmitted frequency and c is the speed of sound. Thus the spatial correlation coefficient of volume reverberation is a decaying function and will tend to zero as the transmitted frequency and/or receiver separation increase.

The geometry for the boundary return is described in Fig. 4(b). The two receivers lie in the xz plane and the line connecting them forms an angle ϕ_0 with the x axis. In this case, for omnidirectional transmission and reception and for

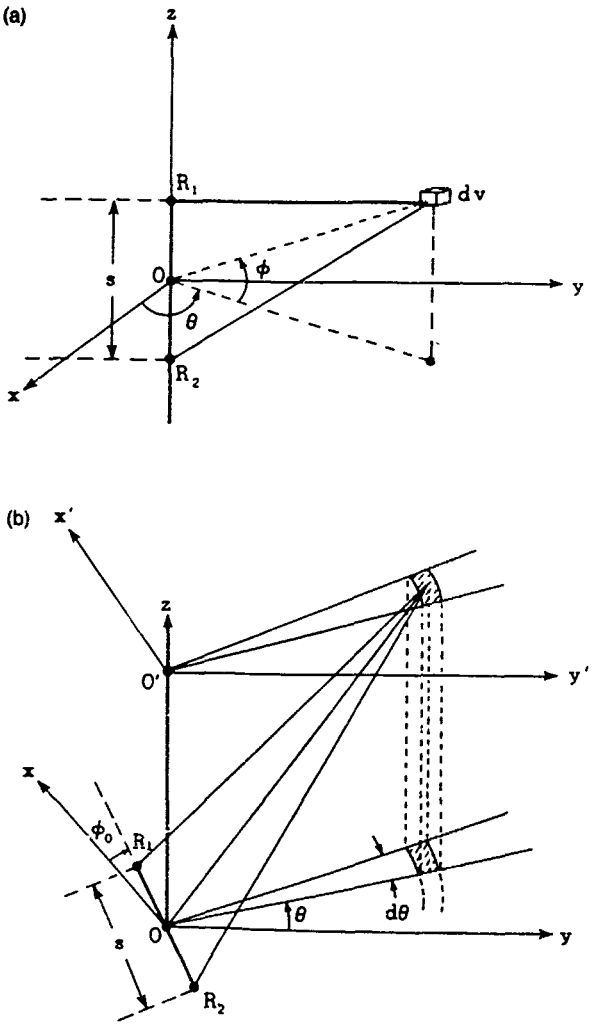

FIG. 4. Spatial correlation geometry. (a) Volume reverberation, (b) boundary reverberation ($\phi_0 = \pi/2$ for vertical separation).

ranges much larger than the receiver separation, the spatial correlation coefficient is given by

$$R_B(s) = J_0(ks \cos \phi_0), \tag{12b}$$

where J_0 is the modified Bessel function of the first kind. For $\phi_0 = 0$ (horizontal separation), the result is again a decaying, oscillating function. However, for $\phi_0 = \pi/2$ (vertical separation), we have

$$R_B(s) = J_0(0) = 1.$$

Therefore, no loss of spatial correlation is suffered for vertical separation of the receivers. This can be explained intuitively in terms of the lack of vertical extent of the insonified surface patch. The above relations are similar to some earlier results on the correlation properties of spatially distributed ambient noise fields (Cron and Sherman, 1962; Jacobson, 1962). For directional transmission and reception, Jackson and Moravan (1984) show that the vertical correlation of volume reverberation will be zero for receiver separations larger than the sum of the dimensions of the transmitting and receiving array. On the other hand, surface and bottom reverberation will be highly correlated between the same vertically separated receivers, at least for ranges large relative to the distance of receiver separation.

Experimental evidence exists supporting these model predictions. For instance, Urick and Lund (1964) have shown varying degrees of correlation between vertically separated receivers for different reverberation types, with boundary returns displaying decidedly higher values than the volume component. The same investigators (Urick and Lund, 1970a,b) have shown that the spatial correlation of composite reverberation in a shallow-water environment is substantially higher in the vertical than in the horizontal. This was confirmed in a more recent experiment involving pulsed, high-frequency sonar and directional receivers (Wilson and Frazer, 1983).

The predicted disparities in vertical correlation form a natural premise for the application of the ANC principle, whereby the correlated component between the primary and reference channels is canceled. If the primary and reference channels consist of the outputs of two vertically separated receivers in a composite reverberation field, one would expect boundary reverberation (the correlated component) to be canceled and volume reverberation (the uncorrelated component) to be preserved at the filter output. Therefore, a vertical array would be conducive to removing boundary reverberation while preserving the volume component. This prediction is supported by the experimental results presented in Sec. IV. It should be noted that if suppression of the entire reverberation background is desired, e.g., in the presence of a discrete coherent signal, then a horizontal array is in order.

C. Reverberation simulation

REVGEN, (REVerberation GENerator) (Goddard, 1985) is a software implementation of the point-scattering model. Simulated returns from a large number of discrete scatterers, distributed randomly throughout the volume and the boundaries, are summed coherently at each receiver to obtain a reverberation time series. The REVGEN output is a dual digital data stream representing the I (in phase) and Q (quadrature) components of the complex-basebanded reverberation signal. A backscattering coefficient for each reverberation type and the densities of their Poisson distributions are specified by the user. Scattering layers, random scatterer motion, platform trajectories, attenuation and reflection losses, arbitrary (multiple) transmitting and receiving beam patterns, and several transmitted signal types may be specified through appropriate REVGEN parameters to create realistic experimental settings. Here, we use REVGEN simulations in parallel with real data to investigate the cancellation performance of the chosen adaptive beamforming scheme.

IV. BOUNDARY REVERBERATION REJECTION IN A SHALLOW-WATER ENVIRONMENT

In this section, the adaptive beamforming concept is applied to real reverberation data from a shallow-water active sonar experiment. The shallow-water environment creates some unique difficulties. As opposed to deep-water settings where the acoustic paths are few and identifiable, shallow-water reverberation returns arrive in rapid succession, imposing stringent adaptation requirements on the algorithm and complicating the performance evaluation process. Volume reverberation is assumed to be the component of interest, with boundary reverberation the interference. This scenario may arise, for instance, in a fisheries sonar application. The performance of a horizontally directed sonar deployed from a surface vessel is often limited by surface reverberation. The general method used is adaptive beamforming with spatial constraints and the LSL algorithm is used exclusively as the central adaptive processor. Given the distinctly different scattering mechanisms responsible for the three reverberation types, the independence assumptions needed for ANC are readily satisfied. No further assumptions need to be made about the relative intensity and duration of signal and interference and no modifications of the algorithm are necessary in order to impose the constraints.

A. Experiment description

The experiment was conducted in the deepest part of Dabob Bay, Washington (maximum depth ~200 m). The physical, biological, and acoustical properties of Dabob Bay have been studied intensively (Helton, 1976). Dabob Bay is characterized by large fluctuations of temperature and salinity. In addition to the usual seasonal variations in the top ~30 m, cellular inhomogeneities exist in the deeper regions, caused by intrusions of Pacific Ocean water. These transient water masses cause wide fluctuations in the sound velocity structure and create the need for up-to-date sound velocity profiling during acoustic experiments. Coring device sampling (Burns, 1962) has shown that the deep regions of Dabob Bay are covered by silt and mud with some sand and fine gravel. A maximum bottom backscattering coefficient of −20 dB has been measured. Correspondingly, the surface backscattering coefficient was found to be in the range of −35 to −25 dB. Intensive volume sampling and volume

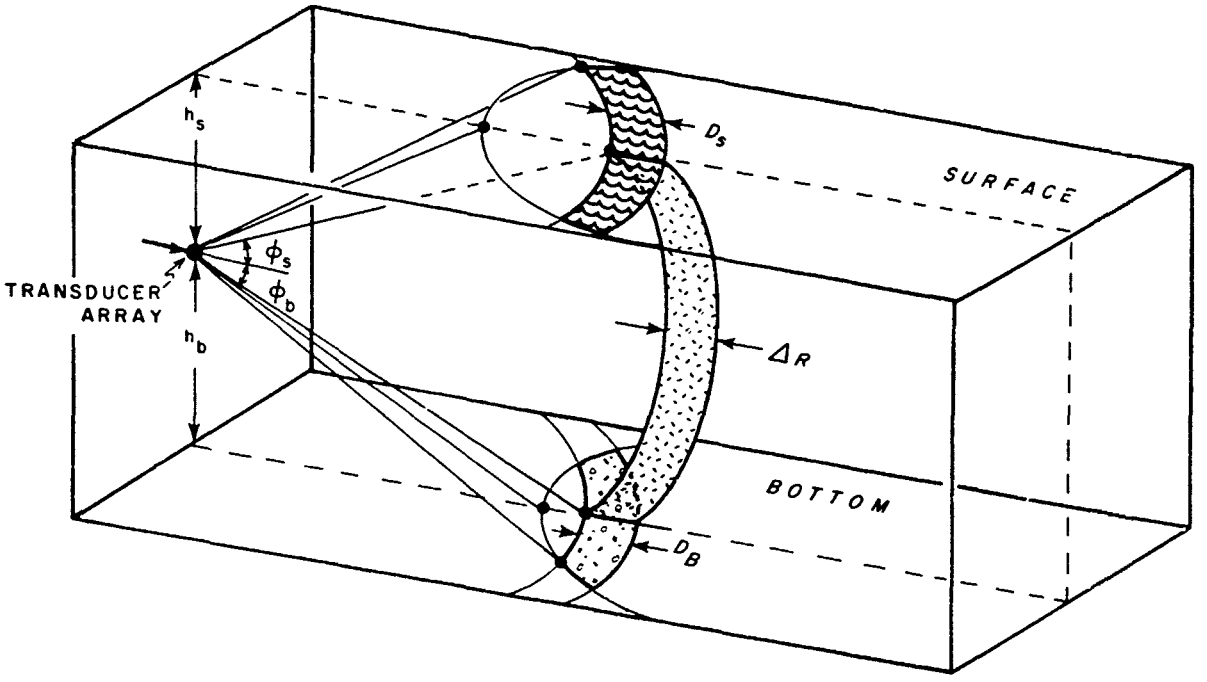

FIG. 5. Shallow-water experimental geometry The surface, volume, and bottom contribute to the backscattered return.

scattering measurements over a period of 2 years have revealed multiple scattering layers with substantial seasonal variations (Anderson, 1981). The maximum measured volume scattering coefficient is ~ -60 dB.

The overall experimental geometry is depicted in Fig. 5. The sonar system moved with constant velocity along straight line paths. It carried a transducer array whose elements were combined by a programmable conventional beamformer capable of producing several transmit/receive beam sets. During one of the experimental runs, a "wide" ($60°\times60°$) transmitting beam was used and 9 row sums of the receiving elements were individually available, thus forming a 9-element vertical array. According to the results of Sec. III this arrangement has good potential for selective reverberation cancellation. We, therefore, focus our attention to this particular data set. The sound velocity profile effective for this run and the corresponding ray tracing diagram are shown in Fig. 6. The sonar system transmitted 180-ms pulses from a depth of 30 m and recorded digitally the complex-basebanded reverberation return. In addition, a narrow-band calibration signal is present, arriving broadside to the array, which is valuable in assessing the cancellation results. A REVGEN simulation preserving the experimental geometry and all known characteristics of the sonar system was carried out. The receiving (row) elements were approximated by rectangular pistons at $\lambda/2$ spacing and a constant sound velocity profile was assumed.

B. Data description

The primary beam was constructed by adding the outputs of the nine row elements. The simulated primary beam is shown in Fig. 7(a). In addition, eight constrained reference beams were created by pairwise subtraction among the nine rows, in the manner depicted in Fig. 1(b). The beam of a single constrained reference beam, characterized by a central null, is the dotted curve in Fig. 7(b). The real and simulated (composite) reverberation signals entering the primary beam are displayed in parallel in Fig. 8. The first plot is a range Doppler map (RDM) display intended to show the time-varying character of the data in the frequency domain. It was constructed by taking successive 128-point FFTs of windowed (Kaiser–Bessel, $\alpha_{KB} = 2.5$) data segments with 50% overlap. The dB magnitude of each transform corresponds to a single line in the pseudo 3-D plot. The main reverberation "ridge" occupies the near-dc region, following complex basebanding. The second plot, an RDM with $\sim$90% overlap, provides a more detailed view of the near ranges where boundary reverberation enters through the sidelobes. The data have been frequency shifted to compensate for the Doppler shift due to sonar motion. Clearly visible is the typical "hook" pattern of negative Doppler features in the initial $\sim$0.5 s of the ping. This pattern is entirely due to high-angle boundary returns which are imparted a lesser net Doppler shift by the velocity of the sonar. With increasing range, as the lower sidelobes and eventually the mainlobe become the boundary reverberation outlets, the pattern merges into the main ridge. This artifact is useful for identifying sidelobe returns and establishing their cancellation following adaptive processing.

Although the real and simulated data have similar overall structure, several differences are apparent. The real data are characterized by a somewhat wider hook which may be an indication that the real beam pattern has an appreciable sidelobe response at a higher angle than the simulated beam

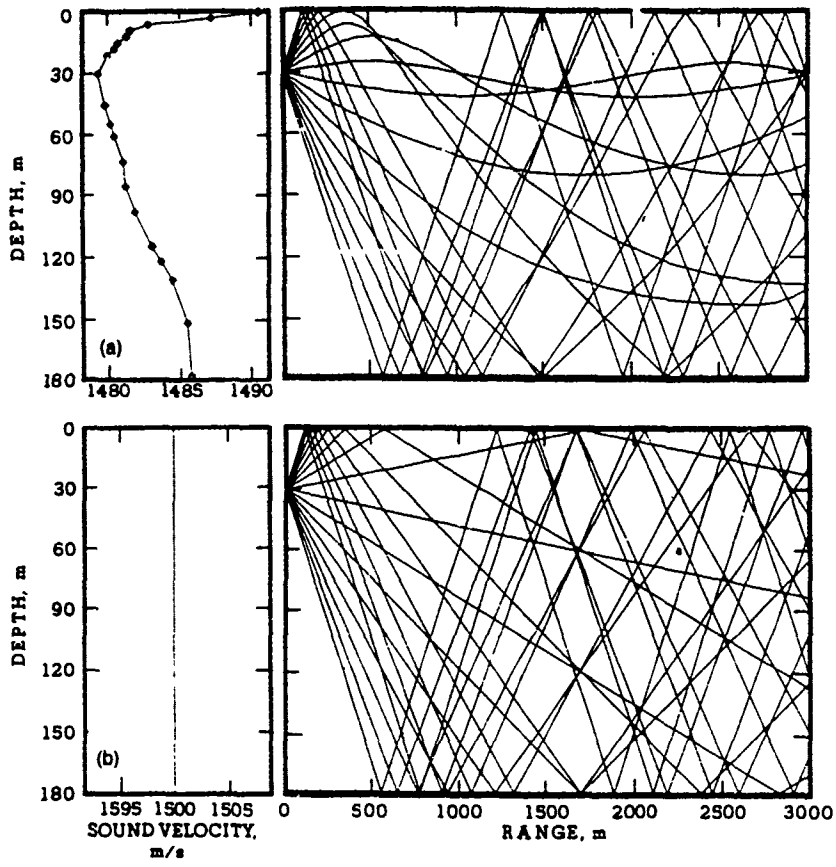

FIG. 6. Velocity profile and ray trace diagram (a) Real data, (b) REVGEN simulation. Note that, in the real data case, a shadow zone is formed in the near surface and no surface reverberation is produced at the far ranges. In the simulated case, on the other hand, surface reverberation continues to be produced at the far ranges.

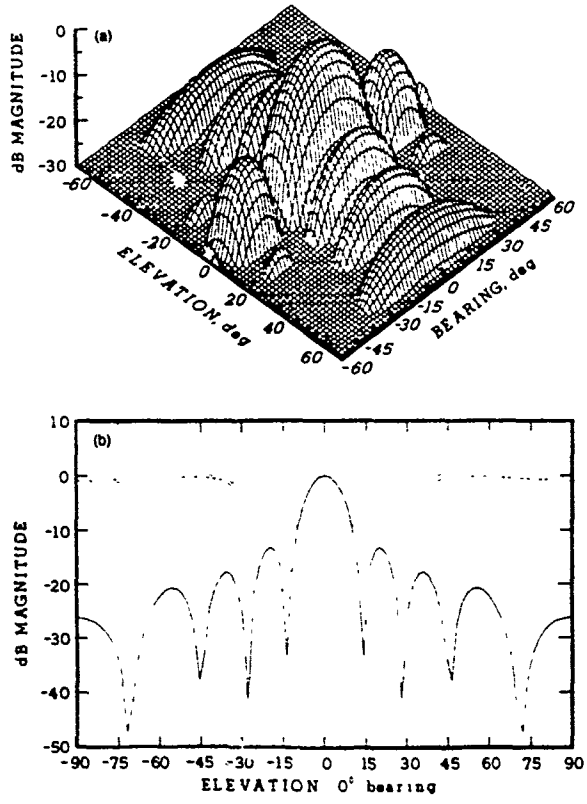

FIG. 7. Beam patterns. (a) Primary beam pattern, produced by adding all nine rows; (b) single vertical 0° bearing cuts of the primary beam (solid line) and of a single constrained beam pattern produced by subtracting two rows (dotted line)

or that the actual velocity of the sonar was underestimated in the simulation. In addition, the simulated reverberation is better sustained at long ranges. Two reasons may be cited for this. First, no decaying function of grazing angle was introduced in the simulation for boundary reverberation. This decay with grazing angle is a well-documented fact (Urick, 1975). The second reason may be inferred from the ray tracing diagram (Fig. 6) and the time of arrival versus angle of arrival plot (Fig. 9). Because of the well-developed thermocline, a shadow zone is formed in the near surface past a range of $\sim$500 m. The surface contribution disappears abruptly at that point. In the simulated case, an isovelocity profile is used and the surface continues to contribute at long ranges. Finally, a high-Doppler calibration signal can be observed in the real data RDM at $t \sim 1.5$ s. It arrives broadside to the array. This signal was not included in the simulation.

C. ANC with a single constrained reference element

A single constrained reference element, created by subtracting one row element from another, has a beam pattern [Fig. 7(b)] which at first glance appears to be well suited for our purposes. Excluding its broadside null, it is nearly omnidirectional in the vertical, thus covering all possible directions of arrival for boundary reverberation. One may expect it to be effective in canceling the sidelobe-born boundary returns and to some extent mainlobe interference, while protecting much of the volume signal in its null.

The data were processed in this manner, using the scalar LSL with $p = 3$ and $\alpha_{LSL} = 0.02$. The single reference chan-

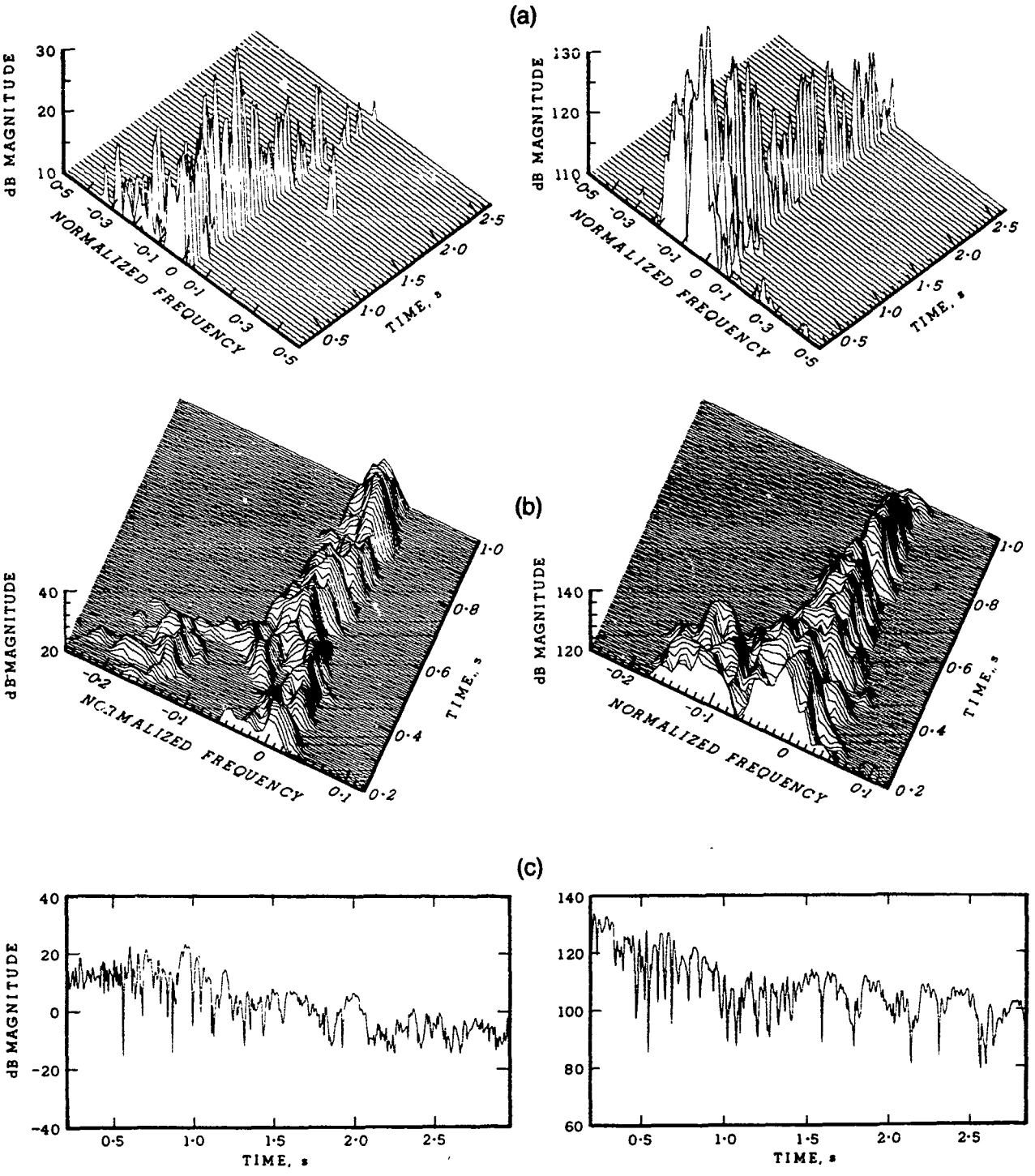

FIG. 8. Shallow-water data Real (left-hand side) and REVGEN (right-hand side). (a) Standard RDM, (b) expanded near-range plot (note the typical hook pattern caused by the high-angle boundary reverberation returns), and (c) time series plot.

nel consisted of rows 5–6. The results for both the real and simulated data are displayed in Fig. 10. In addition to the RDMs and the time series plots, a cancellation curve is included which is simply the dB magnitude of the ratio of primary signal power over filter output power. Cancellation is generally low in the near ranges. In addition, the simulated case displays a significant increase in background noise level for $t \leqslant 0.5$ s. Moderate cancellation was achieved in both cases for intermediate ranges ($1.0 \leqslant t \leqslant 2.0$), while the behavior in the far ranges is distinctly different for real and simulated data. For the latter, cancellation continues to improve with range, while little or no cancellation is observed for the former.

The low overall cancellation in the near ranges is a man-

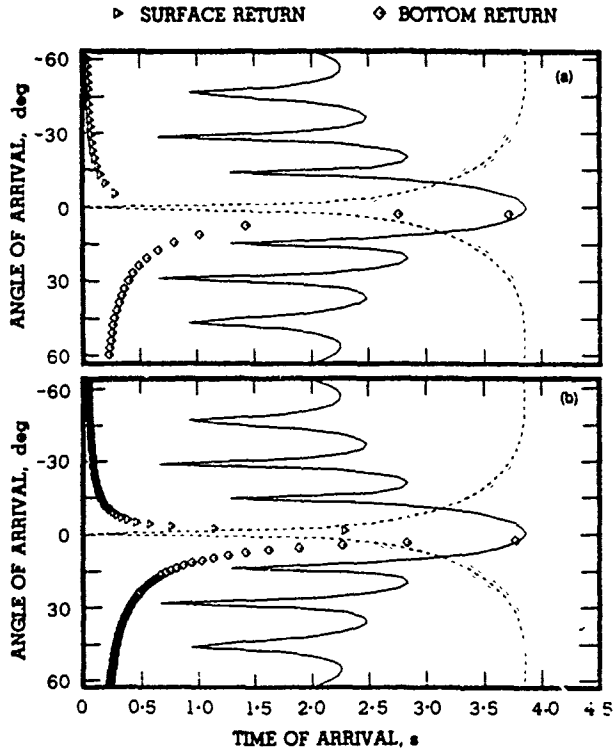

FIG. 9 Angle versus time of arrival (a) Real, (b) REVGEN data These plots were intended to illustrate the origin of the "uncorrelated noise" effect. In the early ranges, the constrained reference beam (dotted line) receives reverberation from angular directions where the primary beam (solid line) has a null response.

ifestation of the ANC theoretical prediction regarding the effect of uncorrelated noise components in either the primary or the reference channel (Widrow *et al.*, 1975). This effect comes into play here as follows: The transmit beam insonifies the entire angular region from $-60°$ to $+60°$. The reference beam, being nearly omnidirectional in the vertical, receives reverberation from the entire range with the exception of the near broadside. The main beam, on the other hand, has a definite sidelobe response which operates on the high-angle returns. Each time boundary reverberation arrives through the nulls between the sidelobes it is excluded from the primary channel. The same components enter the reference channels without being attenuated and cause the uncorrelated-to-correlated noise power ratio to increase, resulting in reduced signal-to-noise ratio at the filter output. This explains the observed rise of the noise "floor" [Fig. 10(a)]. The somewhat better cancellation apparent for the high-angle ($\pm 60°$) returns in the real versus the simulated data may be an artifact of the RDM displays caused by dynamic range differences, unavoidable in view of the necessarily incomplete model of reality which is used in the simulation. The particular sidelobe structure of the real main beam, which may be substantially different from the simulated beam, could also explain this difference.

The difference in far-range cancellation performance is due to the grazing angle effect. In the real case, there is simply little boundary reverberation left in the far ranges and therefore the cancellation potential is low. This effect was not included in the simulation and as a result significant cancellation was achieved there. Interestingly, there is a clear trend of improving cancellation performance with range, which is consistent with another ANC theoretical prediction. Specifically, the output noise spectrum was found to be proportional to the signal-to-correlated noise ratio at the primary input (Widrow *et al.*, 1975). In our experimental geometry, this ratio should decrease with range as the boundary returns begin to enter through the mainlobe instead of the sidelobes. Therefore, one may expect the output noise power to decrease and cancellation to improve with range.

Two additional observations can be made concerning the real data results. First, the high-Doppler "control" signal was virtually unaffected by this processing. This is an indication that the constraining scheme is effective. Second, a large zero-Doppler feature was revealed [marked V1 in Fig. 10(c)] at $t \sim 1.0$ s. This is probably a volume reverberation feature, the origin of which will be discussed later.

1. Remarks

(i) Processing with a single constrained reference beam would be more effective in the sidelobe cancellation mode if the transmit beam was identical to the main receive beam. In that case, the "uncorrelated noise" effect would not exist and near-range cancellation would improve.

(ii) Regarding the constrained reference cancellation beam, a choice must be made about the width of the broadside null. It would be desirable to have a wide null initially, when interference arrives through the sidelobes and a progressively narrower null as the main beam begins to intersect the boundaries.

(iii) An alternative explanation for the improved cancellation observed in the far ranges is in terms of the increased spatial coherence of boundary reverberation predicted by the point-scattering model.

D. An application of constrained adaptive beamforming

The multichannel joint-process filter can compensate for noise components not present in the primary channel, which are correlated between the reference channels. Therefore, if the multichannel LSL filter were to be used in the present case, with the eight constrained reference elements comprising the vector reference input, one may expect it to be more effective than the single-channel filter by alleviating the near-range "uncorrelated noise" effect. Equivalently, the multichannel adaptive algorithm should, in theory, form an adaptive reference (cancellation) beam, with the tendency to emulate the sidelobe features of the main beam. This adaptive reference beam will still have the central null according to the beam pattern product theorem (Urick, 1975) and, therefore, the basic constraining scheme will still be in effect.

The results for the same ping processed through the 8-channel LSL filter are displayed in Fig. 11. Overall, cancellation is substantially improved over the single reference ele-

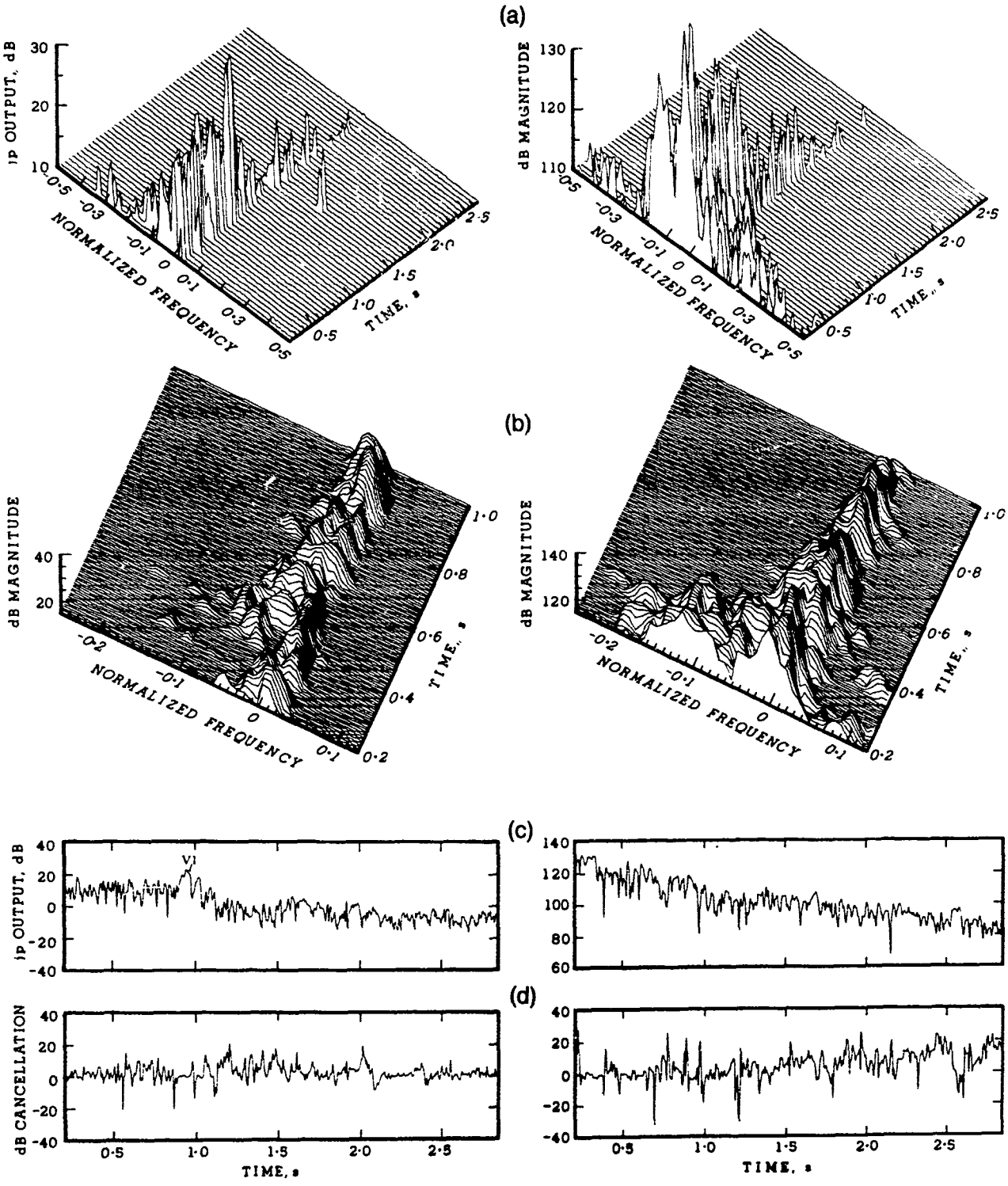

FIG. 10. ANC with single constrained reference element Real (left-hand side) and REVGEN simulation (right-hand side). (a) Standard RDM, (b) expanded RDM. Substantial reverberation cancellation is seen for both real and simulated data in the far ranges, but near-range performance is marginal. Note the increase in noise level in the simulated results (c) Output time series and (d) dB cancellation curve. A volume "signal" (V1) is exposed in the real data output. Cancellation is seen to improve with range for simulated data and to level out for real data.

ment case. As evidenced by the virtual elimination of the hook pattern from the RDM plots, the sidelobe boundary interference has been successfully removed. A dramatic improvement is observed in far-range cancellation. As a result, in the real data case, volume feature V1 is even more clearly in evidence at $t \sim 1.0$ s and an additional feature (V2) was exposed at $t \sim 1.6$ s.

In order to examine more closely the cancellation per-

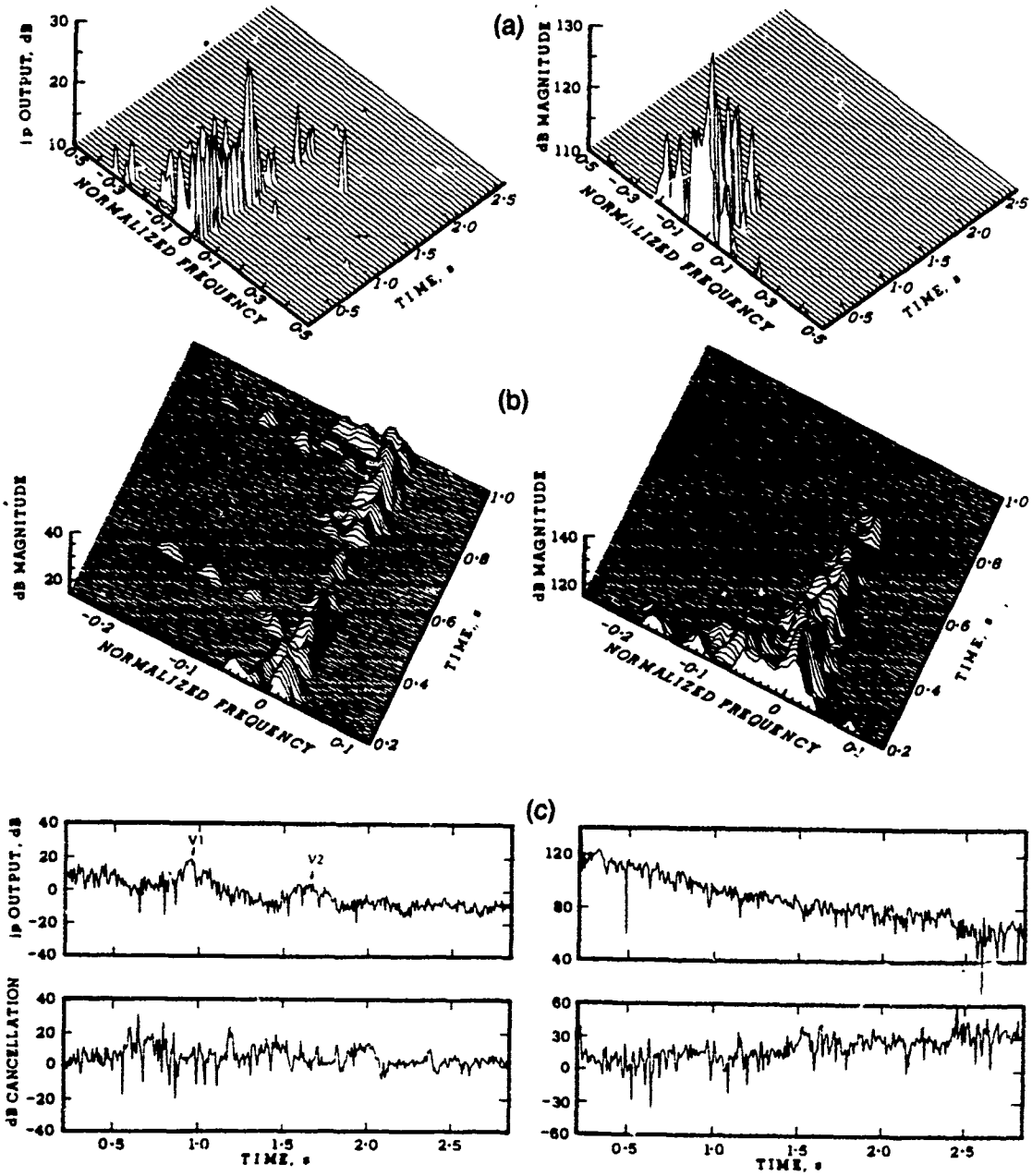

FIG. 11. Adaptive beamforming with eight constrained reference elements. Real (left-hand side) and REVGEN simulation (right-hand side) (a) Standard RDM; (b) expanded RDM. Cancellation improves dramatically for both real and simulated data in all ranges. (c) Output time series and dB cancellation curve. An additional volume "signal" (V2) is revealed.

formance of this arrangement, a separate simulation run was performed with only volume scatterers present. Thus the desired "signal" was isolated. Figure 12(a) shows that the multichannel constrained adaptive beamformer is generally very successful toward achieving our objective, especially for $t \geq 1.0$ s. Insight may be gained on the adaptive operation performed by this structure by considering the adaptive cancellation beam it creates. Vertical "cuts" of this beam, at zero bearing, were calculated from each set of eight cross-channel reflection coefficients at ~0.024-s intervals and are displayed in a "waterfall" plot [Fig. 12(b)]. Note that the adaptive cancellation beam still has the central adaptive null, as expected. Moreover, it strives to approximate the sidelobe structure of the main beam in the early ranges of high-angle boundary returns. At longer ranges ($t \geq 1.0$ s), when the sidelobe activity subsides, the adaptive cancellation beam concentrates on the mainlobe boundary returns to the extent allowed by the broadside null.

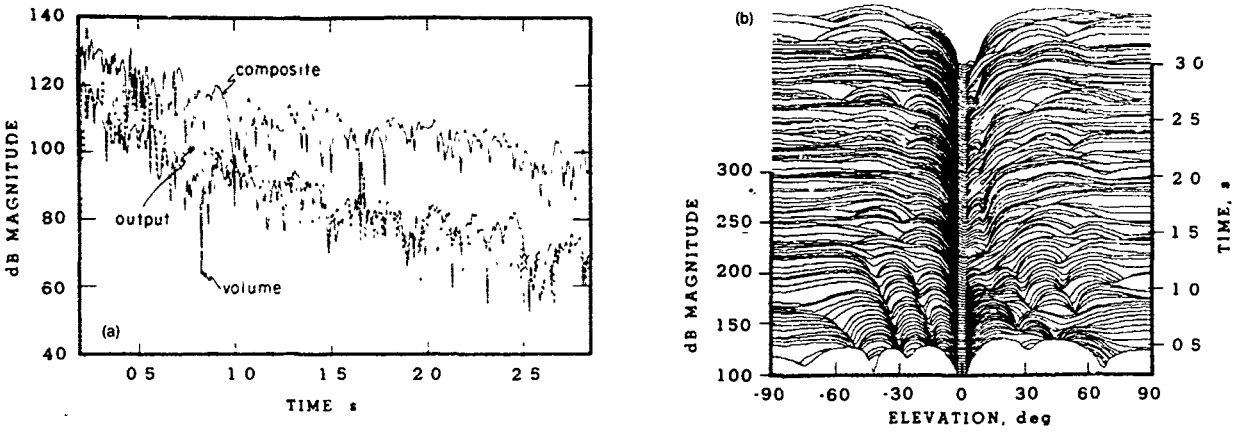

FIG 12. Selective reverberation cancellation performance. (a) Composite reverberation (top solid line), pure volume component (bottom solid line), and output of 8-channel adaptive beamformer (dotted line) With the exception of a near-range region (0.5–1 0 s), selective reverberation cancellation is achieved (b) "Waterfall" plot of the adaptive reference (cancellation) beam produced by the algorithm. The adaptive beam strives to emulate the sidelobe structure of the primary beam in the near ranges

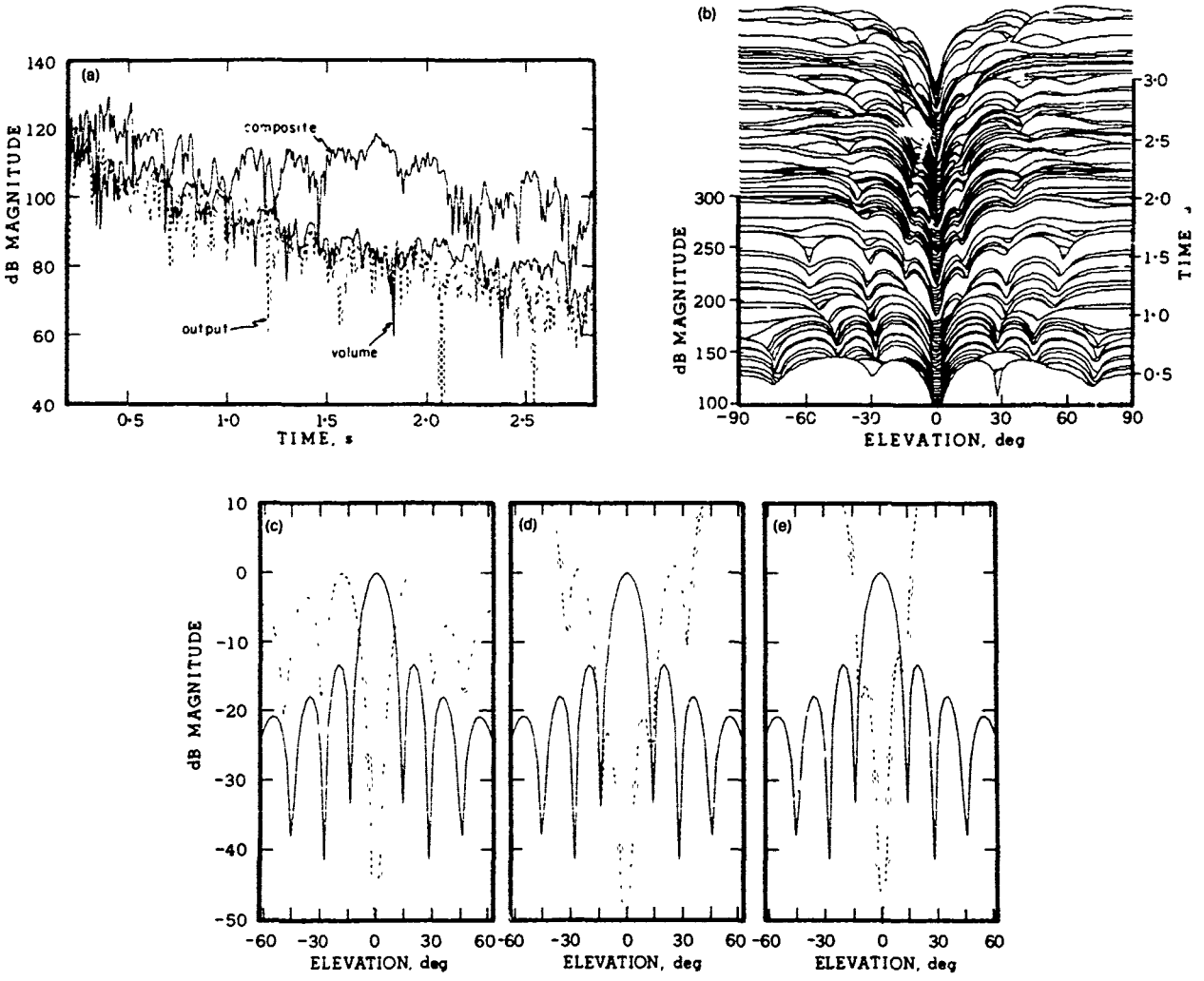

FIG. 13. REVGEN symmetric scenario (a) Cancellation performance improves in the near ranges and (b) a symmetric adaptive cancellation beam is produced Vertical "cuts" of the adaptive beam pattern at (c) $t = 0.5$ s, (d) $t = 1.0$ s, and (e) $t = 2.0$ s show three stages of the adaptation process. Initially, the reference beam (dotted line) emulates the sidelobe structure of the primary beam (solid line), thus eliminating the near-range "uncorrelated noise" effect. As the high-angle sidelobe returns diminish and boundary reverberation begins to enter through the mainlobe, the reference beam progressively narrows its center null to compensate for the near-grazing boundary returns.

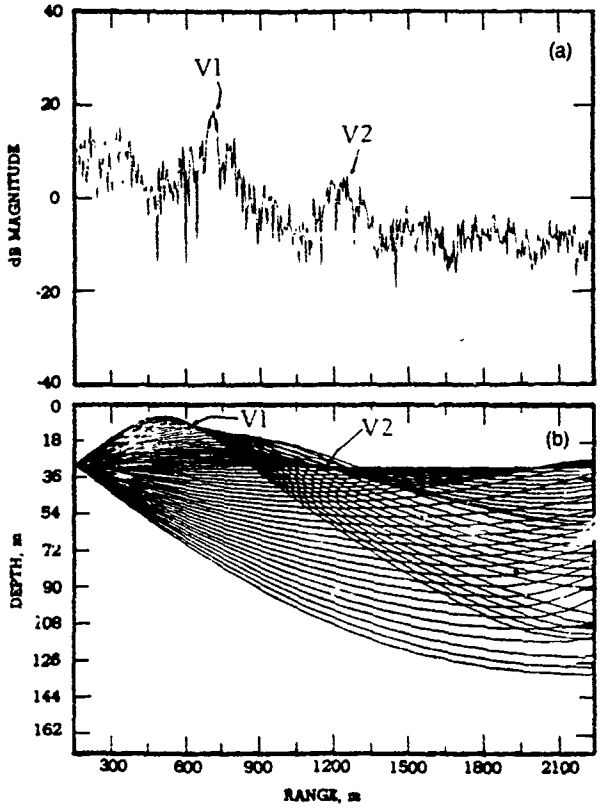

FIG 14. Volume "feature" interpretation The two volume "signals" exposed in the data by the adaptive beamforming operation (a) correspond well in range with two caustics resulting from the sharp velocity gradient in the near surface. The ray trace diagram (b) covers an angular range of $\pm 3°$, which is covered by the null of the reference channel Therefore, the strong volume reverberation returns originating at the caustic regions are protected from cancellation and preserved at the filter output

1. Simulation with symmetric experimental geometry

In order to further examine the nature of the adaptive cancellation beam, the same processing was carried out in a more benign symmetric experimental geometry. In this REVGEN simulation, the overall depth was set to 300 m and the sonar was positioned at 150 m. The surface and bottom backscattering coefficients were both set equal to -30 dB. In the sequence of plots presented in Fig. 13, it is apparent that the symmetrical arrangement is beneficial to the cancellation performance in the near ranges. The adaptive cancellation beam is itself symmetric and its behavior easier to interpret. In its sidelobe cancellation mode ($t = 0.5$) it successfully emulates the sidelobe structure of the main beam. As the mainlobe begins to intersect with the boundaries, the adaptive filter is seen to alter adaptively the effective width of the broadside null, making it progressively narrower with increasing range [plots for $t = 1.0$ and $t = 2.0$ in Fig. 13(d) and (e)]. This is intuitively satisfying and explains the dramatic improvement in far-range cancellation performance achieved by the adaptive beamformer over single-channel (i.e., fixed null shape) ANC.

E. Volume "feature ' interpretation

A number of hypotheses were considered regarding the origin of the volume features (V1 and V2) exposed by the adaptive beamforming operation on the real data. First, the possibility that they are acoustic echoes from schools of fish or cellular water masses within the angular range of the null was debated. This hypothesis was rejected based on the processing results for another ping preceding our data by ~ 104 s. During this time, assuming they were moving slowly relative to the sonar, one would expect the echoes to be at discernibly different ranges for the two pings. This, in fact, was not the case; the features appeared at precisely the same ranges.

Alternatively, the features may be explained by the presence of a strong, well-defined scattering layer at a shallow depth. Such a layer, consisting mainly of prespawning populations of Pacific herring, has been consistently observed in the spring months (Friedl, 1970; Anderson, 1981). If, due to refraction effects, the near broadside rays residing in the null region intersect this layer at appropriate ranges, they could possibly account for the features. The high-resolution ray tracing plot created to provide support for this hypothesis exposed additional evidence (Fig. 14). Specifically, two caustics are clearly visible at ranges which correspond well with the feature position. The intense scattering caused by the presence of the caustics in the strong shallow scattering layer can probably account for the two volume features.

V. SUMMARY

An adaptive beamforming technique with simple spatial constraints was considered. The theoretical foundation of the joint-process least-squares lattice algorithm was exposed. The predictions of the point-scattering model regarding the spatial correlation properties of oceanic reverberation were found to be valuable in determining optimum adaptive array configurations. Data from a shallow-water active sonar experiment were used to demonstrate the potential of removing boundary reverberation while preserving the volume component. Several predictions of Widrow *et al.*'s (1975) ANC model were found to have direct bearing on our results. Constrained adaptive beamforming implemented through the multichannel joint-process least-squares lattice was shown to offer superior performance over single-channel ANC. REVGEN simulations of the experiment proved to be very useful in assessing algorithm performance and interpreting the cancellation results.

ACKNOWLEDGMENTS

I wish to thank Professor W. S. Hodgkiss for many hours of useful discussion throughout the course of this work, R. P. Goddard of the Applied Physics Laboratory (University of Washington) for making REVGEN available to the Marine Physical Laboratory, and Jo Griffith for preparing the figures. This research was supported by the Naval Sea Systems Command, Code 63R14.

Alexandrou, D (1985a) "Sea beam sidelobe interference cancellation," OCEANS '85 Conf Proc., San Diego, CA, 12–14 November 1985, 472–476.

Alexandrou, D. (1985b) "Selective reverberation cancellation via adaptive beamforming," Ph D thesis (Univ of California, San Diego)

Anderson, V. C (1969). "DICANNE, a realizable adaptive process," J Acoust Soc Am 45. 398–405

Anderson, W. B (1981) "Volume reverberation characteristics of NUWES ranges," NUWES Rep. 1542.

Applebaum. S P., and Chapman, D J (1976) "Adaptive arrays with main beam constraints," IEEE Trans. Ant Prop AP-24, 650–662

Bendat, J S., and Piersol, A G (1971) *Random Data Analysis and Measurement Procedures* (Wiley, New York).

Buckley, J P., and Urick, R J (1968) "Backscattering from the deep sea bed at small grazing angles," J. Acoust. Soc Am 44, 648–650

Burns, R E (1962) "A model of sedimentation in small sill-less embayed estuaries of the Pacific Northwest," Ph D thesis (Univ. of Washington, Seattle)

Chapman, R P., and Harris, J. H. (1962) "Surface backscattering strengths measured with explosive sound sources," J Acoust Soc Am 34, 1592–1597.

Clay, C S , and Medwin, H (1964) "High-frequency acoustical reverberation from a rough sea surface," J. Acoust Soc Am. 36, 2131–2135.

Clay, C S , and Medwin, H (1977) *Acoustical Oceanography* (Wiley, New York)

Cron, B F., and Sherman, C H (1962). "Spatial correlation functions for various noise models," J. Acoust Soc Am 34, 1732–1736

Davisson, L D (1966) "A theory of adaptive filtering," IEEE Trans Inform Theory IT-12, 97–102

Faure, P (1964) "Theoretical model of reverberation noise," J. Acoust Soc Am 36, 259–266.

Friedl, W A. (1970) "Sonic scattering and its probable causes in two areas of Puget Sound," in *Proceedings of the International Symposium on Biological Sound Scattering in the Ocean*, edited by G B Farquhar 31 March–2 April (Arlie House Conference Center, Warrenton, VA Maury Center for Ocean Science, Report No MC-005), pp 527–548

Friendlander, B , Morf, M , Kailath, T , and Ljung, L (1979) "New inversion formulas for matrices classified in terms of their distance from Toeplitz matrices," Lin Alg Appl 27. 31–60

Frost, O L (1972) "An algorithm for linearly constrained adaptive array processing," Proc IEEE 60. 926–935

Gabriel, W. F (1976) "Adaptive arrays—An introduction," Proc IEEE 64, 239–272

Glaser, E M (1961) "Signal detection by adaptive filters," IRE Trans Inform Theory IT-7. 87–98

Goddard, R. P (1985) *REVGEN, High-Fidelity Simulation of Sonar Signals* (Applied Physics Labor., Univ of Washington, Seattle, WA)

Greenblatt, P R. (1980) "Observations of zooplankton patchiness using a high frequency sonar and a multiple sample plankton net," Ph D thesis (Univ. of California, San Diego).

Griffiths, J J (1969). "A simple adaptive algorithm for real-time processing in antenna arrays," Proc IEEE 57, 1696–1704.

Griffiths, J. J. (1978) "An adaptive lattice structure for noise-canceling applications," IEEE International Conference on Acoustics, Speech and Signal Processing, Tulsa OK, April 1978. 87–90

Helton, R. A. (1976). "Oceanographic and acoustic characteristics of the Dabob Bay range," NAVTORPSTA Rep 1300

Hodgkiss, W. S., and Presley, J. A. (1981). "Adaptive tracking of multiple sinusoids whose power levels are widely separated," IEEE Trans Circuits Syst CAS-28, 550–561.

Holliday, D. V. (1974). "Doppler structure in echoes from schools of pelagic fish," J. Acoust. Soc Am. 55, 1313–1322.

Jackson, D. R., and Moravan, K. Y. (1984) "Horizontal spatial coherence of reverberation," J Acoust. Soc. Am 75, 428–436

Jacobson, M. J (1962). "Space-time correlation in spherical and circular noise fields," J. Acoust Soc Am. 34, 971–978.

Kaye, G. T (1978) "Backscattering from discrete targets at 87.5 kHz," J Acoust. Soc Am 64, 556–562

Lee, X (1980). "Canonical ladder form realizations and fast estimation algorithms," Ph.D. thesis (Stanford University, Stanford, CA)

Lucky, R W. (1965) "Automatic equalization for digital communication," Bell Sys. Tech J 24, 547–588.

Makhoul, J. (1978) "A class of all-zero lattice digital filters: Properties and applications," IEEE Trans Acoust Speech Signal Process ASSP-26, 304–314.

McKinney, C M , and Anderson, C D (1964) "Measurements of backscattering of sound from the ocean bottom," J Acoust. Soc Am 36, 158–163

Medwin, H (1966). "Specular scattering of underwater sound from a wind-driven surface," J Acoust Soc Am 41, 1485–1495

Middleton, D. (1967a) "A statistical theory of reverberation and similar first-order scattered fields, part I Waveforms and the general process," IEEE Trans Inform Theory IT-13, 372–392.

Middleton, D (1967b) "A statistical theory of reverberation and similar first-order scattered fields, part II Moments, spectra and special distributions," IEEE Trans Inform Theory IT-13, 393–414.

Middleton, D. (1972a). "A statistical theory of reverberation and similar first-order scattered fields part III. Waveforms and fields," IEEE Trans Inform Theory IT-18. 35–67

Middleton, D. (1972b) "A statistical theory of reverberation and similar first-order scattered fields part IV: Statistical models," IEEE Trans Inform Theory IT-18. 68–90

de Moustier, C P (1985) "Inference of manganese nodule coverage from Seabeam acoustic backscattering data," Geophysics 50, 989–1001

Ol'shevskii, V V (1967) *Characteristics of Sea Reverberation* (Consultants Bureau, New York)

Orr, M H , and Hess, F R (1978) "Remote acoustic monitoring of industrial chemical waste released at Deep Water Dumpsite 106," J Geophys Res 83, 6145–6154

Pinkel, R (1981) "On the use of Doppler sonar for internal wave measurements," Deep-Sea Res 28A, 269–289

Satorius, E H , and Alexander, S T (1979) "Channel equalization using adaptive lattice algorithms," IEEE Trans Comm COM-27, 899–905

Schade, C. M (1971) "Optimal regulation of physiological systems via real-time adaptive model synthesis," SEL-71-003 (Stanford Electronics Lab , Stanford Univ , Stanford, CA)

Urick, R J , and Hoover, R M (1956) "Backscattering of sound from the sea surface, its measurement, causes, and application to the prediction of reverberation levels," J Acoust Soc Am 28. 1038–1042

Urick, R. J , and Lund, G R (1964). "Vertical coherence of explosive reverberation," J Acoust Soc Am 36, 2164–2170

Urick, R J., and Lund, G R (1970a). "Horizontal coherence of explosive reverberation," J. Acoust Soc Am 47, 909–911.

Urick, R J , and Lund, G. R (1970b) "Vertical coherence of shallow-water reverberation," J Acoust Soc Am 47, 342–349.

Urick, R J. (1975). *Principles of Underwater Sound* (McGraw-Hill, New York).

Widrow, B., and Hoff, M , Jr (1960) "Adaptive switching circuits," IRE WESCON Conv Rec , part 4, 96–104

Widrow, B., Mantey, P. E , Griffiths, L. J , and Goode, B B (1967) "Adaptive antenna systems," Proc IEEE 55, 2143–2159

Widrow, B., Glover, J. R , McCool, J. M , Kaunitz, J., Williams, C. S , Hearn. R H , Zeidler, J. R , Dong, E Jr., and Goodlin, R C (1975) "Adaptive noise cancelling: Principles and applications," Proc. IEEE 63. 1692–1716.

Wilson, G. R., and Frazer, M E. (1983). "Horizontal covariance of surface reverberation: Comparison of a point-scatterer model to experiment," J. Acoust. Soc. Am. 73, 749–760.

J-OE/13/4//23361

Large Aperture Digital Acoustic Array

Barbara J. Sotirin
John A. Hildebrand

Reprinted from
IEEE JOURNAL OF OCEANIC ENGINEERING
Vol. 13, No. 4, October 1988

Large Aperture Digital Acoustic Array

BARBARA J. SOTIRIN AND JOHN A. HILDEBRAND

(Invited Paper)

Abstract—**A digital array of 120 acoustic channels and 900 m in length has been constructed to study low-frequency (20–200 Hz) ambient noise in the ocean. The array may be deployed vertically or horizontally from the research platform *FLIP* and the array elements are localized with a high-frequency acoustic transponder network. This paper describes the instrumentation, telemetry, and navigation systems of the array during a vertical deployment in the northeast Pacific. Preliminary ambient noise spectra are presented for various array depths and local wind speeds. Ambient noise in the frequency band above 100 Hz or below 25 Hz increases with local wind speed. However, in the frequency band 25–100 Hz ambient noise is independent of wind speed and may be dominated by shipping sources.**

Keywords—**acoustic array, ambient noise, acoustic navigation, low frequency.**

I. Introduction

A DIGITAL ARRAY of 120 acoustic channels and 900 m in length has been constructed for the study of low-frequency (20–200 Hz) ambient noise. A large aperture array is required for high-resolution directional information at low frequencies. A well-filled array is required to provide low side-lobe levels for the study of ambient noise. This paper describes the characteristics of a large aperture linear array of hydrophones which may be deployed vertically or horizontally from the research platform *FLIP*. Preliminary observations of low-frequency ambient noise from a vertical deployment of this array in the northeast Pacific during September 1987 are described.

Oceanic ambient noise is the prevailing sustained background of sound in the ocean. These noise levels place constraints on the operation of acoustic sensors in the ocean. For this reason, it is valuable to understand the sources generating the sound, the absolute levels, and the spectral shapes of ambient noise. Low-frequency noise is particularly important because of its low attenuation and therefore its ability to propagate over long distances. Only recently has it been practical to investigate the directionality of ambient noise sources at low frequency (less than 100 Hz) due to power, size, and cost constraints.

The following have been identified as sources of low-frequency noise in the ocean [1]. shipping, wind and waves, seismic disturbances, and nonlinear ocean wave interactions. In the frequency band between 20 and 100 Hz, shipping is thought to be the dominant noise source where shipping sources are present [2], [3]. This component may include reverberative paths, perhaps related to prominent bottom topographic features, as well as forward scattering and channeling of the shipping sources. The variation of shipping noise may depend on whether the sources are of single-ship or multiple-ship origin and whether they are local or distant.

At frequencies between 100 and 200 Hz, sea surface noise generated by wind and waves may be dominant. The reported contribution by local wind sources in this band is quite variable, ranging from a difference in spectral level of approximately $+16$ to -4 dB/μPa/$\sqrt{\text{Hz}}$ [1], [4]. The sources responsible for this variation may be identified by examining the vertical and horizontal directionality. Distant storms and noise generated at the edges of the ocean due to waves breaking on cliffs, rocks, or beaches as well as the nonlinear generation due to interference of incoming and reflected coastal swell may produce an azimuthally nonuniform contribution; local wind should induce a vertically variable contribution.

The unique capabilities of the array described in this paper allow its deployment as a high-performance vertical or horizontal array. Arrays previously used to measure low-frequency vertical directionality are listed in Table I to facilitate comparison. The number of elements (120) and large aperture (900 m) of our array is substantially greater than previously reported vertical arrays. This large aperture will allow higher resolution vertical directionality than was previously available. Horizontal directionality is usually measured using large aperture towed arrays. Our array can be moored horizontally because of its neutrally buoyant design. When operated in the horizontal configuration, the flow noise affecting our array is significantly less than for towed arrays, leading to improved array performance.

II. Array Description

This section describes the array electrical and mechanical design. The array has a modular design, which facilitates assembly and transportation and allows for a variable aperture. It is separable into identical hose sections of ten elements each, joined together by in-line interchangeable pressure cases. Each of the ten elements consists of two hydrophones, a preamp, a filter, and a line drive submerged in insulating norparm oil. The oil-filled hoses are neutrally buoyant in seawater, necessary for horizontal deployments. The interelement spacing is 7.5 m and the elements are secured within the 2.54-cm diameter urethene hose by a kevlar line which is terminated near each end of the hose subsection. In-line pressure cases are located between each hose section of ten hydrophones. The pressure cases are 45 cm long with a 7.6 cm outside di-

Manuscript received February 2, 1988; revised July 6, 1988. This work was supported by the Office of Naval Research under Contract nos. N00014-87-K-0225 and N00014-87-C-0127.

The authors are with the Marine Physical Laboratory, Scripps Institution of Oceanography, La Jolla, CA 92093.

IEEE Log Number 8823361.

0364-9059/88/1000-0271$01.00 © 1988 IEEE

TABLE I
COMPARISON OF VERTICAL ARRAYS

Number of Elements	Aperture meters	Hydrophone Spacing	Frequency Range Hz	Deployment Depth (actual) meters	Deployment Platform	Reference
120	960	uniform	20-200	400-3100	*FLIP**	this paper 1988
11	34	nested subarrays	62.5-1K	200	free floating	[14] Buckingham and Jones 1987
48	115	uniform	0-450	sound channel	*FLIP*	[15] Hodgkiss and Fisher 1986
27	93	uniform	0-600	sound channel	*FLIP*	[15] Hodgkiss and Fisher 1986
31	180	nested subarrays	20-800	300	free floating	[3] Burgess and Kewley 198[illegible]
31	310	uniform	45-100	1500	surface ship	[16] Wales and Diachok 1982
12	237	logarithmic	<200	300-3100	free floating	[17] Browning, *et al* 1982
20	<560 (variable)	uniform	5-400	700-4800	*FLIP*	[18] Tyce 1982 [19] Anderson 1979
40	97	geometric	112-1414	4400	anchored to bottom	[20] Axelrod, *et al* 1965

* *FLIP* (Floating Instrument Platform) is a manned 109 meter spar buoy stable platform operated by the University of California, San Diego, Marine Physical Laboratory.

ameter providing a low-profile cross section. These pressure cases house nonpressure tolerant electronics for processing and telemetering the hydrophone signals. Hydrophone data are transmitted asynchronously along the ray to a telemetry module near the *FLIP* end of the array. This module buffers the data and synchronously transmits it through a double-lay armored electrical cable to the surface where it is recorded by the data acquisition computer (LSI-11). The tension carried by the electrical support cable is transferred at the telemetry module to a 1.5 cm diameter kevlar line. During vertical deployment, the hoses and pressure cases are attached to the kevlar line, which has 1500 kg at its bottom to maintain verticality. The array is deployed from the research platform *FLIP*, which maintains station by a multipoint moor. The array is suspended from a hydrographic winch which allows it to be lowered to a specified depth below *FLIP*. Fig. 1 shows a schematic of the array configuration during vertical deployment.

The coaxial armored uplink electrical cable carries frequency-multiplexed data in three bands: uplink data, downlink commands, and dc power. The spectrum allocated for the uplink data is from 100 kHz up to approximately 1.5 MHz. The uplink data rate is 1 Mbit per second encoded using a Miller code to reduce the bandwidth required to approximately 500 kHz. The downlink spectrum is from 100 kHz down to 1.5 kHz. The downlink data is encoded on a 20 kHz carrier which is used to synchronize the data sampling clocks, and a command synchronization bit sequence is transmitted every 2 ms. The cable simultaneously carries the dc power for the array. Each section of the array has dc-to-dc converters that produce 5 V at 600 mA and ±15 V at 150 mA to power the electronics and hydrophone elements. The sections are in series so that they use the same current; the voltage necessary for the complete array is 5.1 V times the number of sections. The power loss in the armored uplink cable is proportional to the current and does not change as the number of array sections changes.

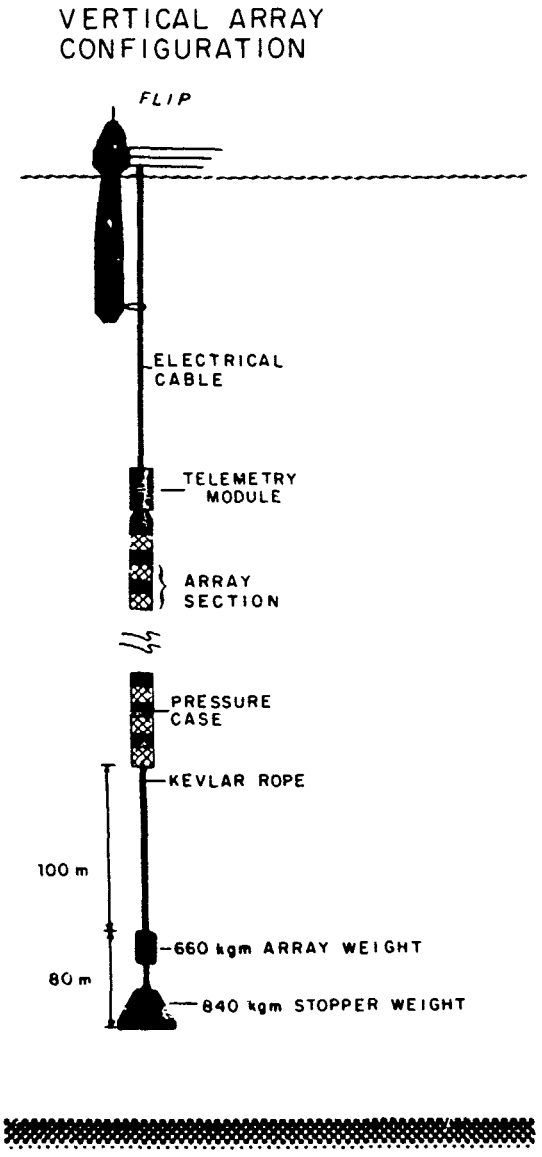

Fig. 1. Vertical deployment configuration of the low-frequency digital acoustic array from the research platform *FLIP*.

A. Uplink Data Stream

This section describes the uplink of acoustic data from the array hydrophones to the topside electronics. The data stream

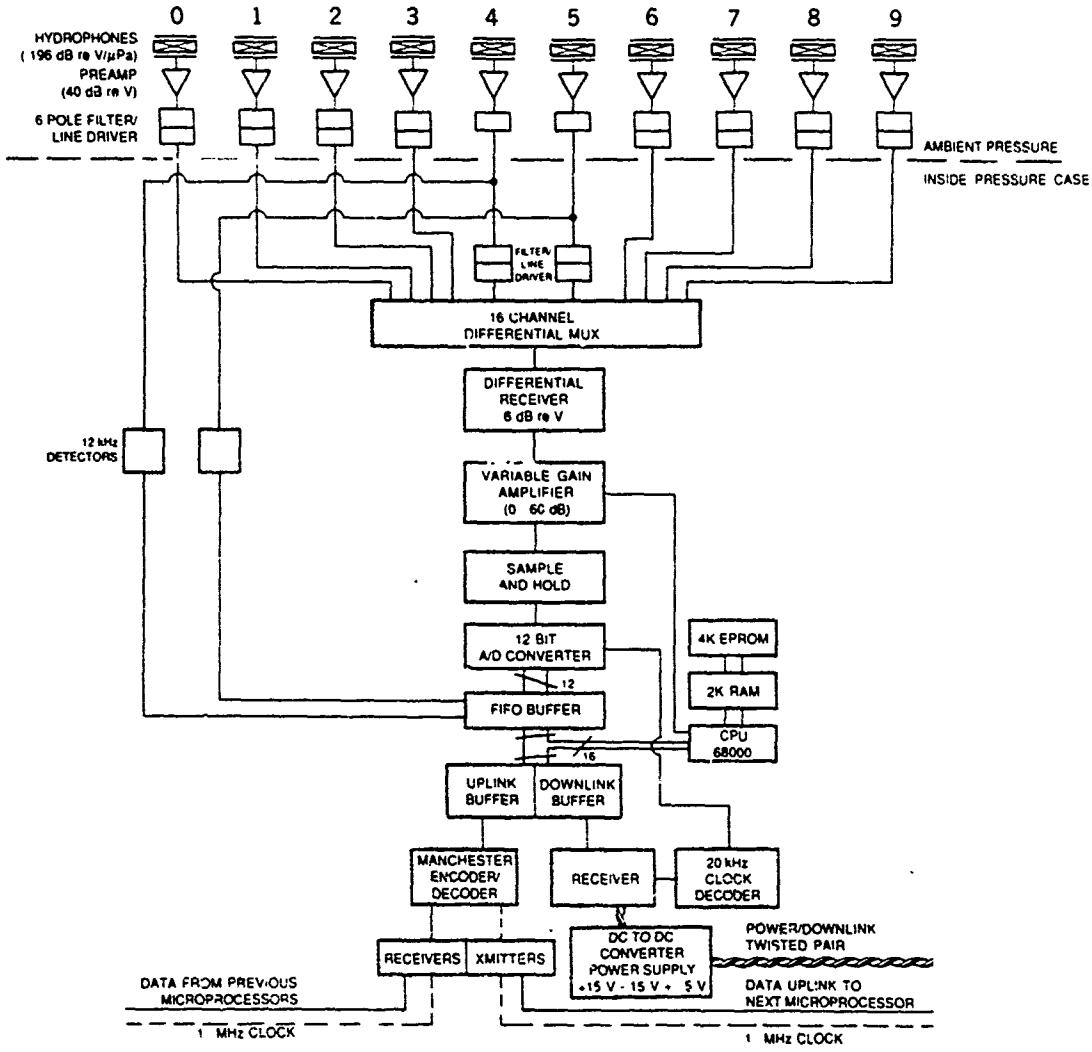

Fig 2. Array Section Block Diagram. The hydrophone signals are amplified and filtered at the element except for hydrophones 4 and 5 which are filtered within the processor pressure case to allow detection of 12 kHz navigation signals. The low-frequency acoustic signals are multiplexed, amplified, captured by the sample and hold, and converted to digital format before being transmitted to the surface.

originates at the hydrophones. It is amplified, filtered, converted to a digital signal, reformatted, and finally transmitted to the surface, as shown schematically in Fig. 2. The hydrophones are an Aquadyne AQ-1 with sensitivity of −204 dB re 1 V/μPa and a capacitance of 12 nf. AQ-1 hydrophones have been calibrated with respect to pressure, temperature, and frequency and exhibit a well-behaved response over the range of operating conditions [5]. There is a 2 to 3 dB re 1 V/μPa sensitivity increase from low pressure (near surface) to high pressure (6000 m), a 0.2 to 0.3 dB re 1 V/μPa sensitivity increase from 0° to 22°C, and a ±0.2 dB re 1 V/μPa sensitivity variation across a frequency band of 10 to 1000 Hz. There are two hydrophones per array element wired in series for an element sensitivity of −198 dB re 1 V/μPa. Tested at a constant depth (1830 m), the relative phase of the hydrophones is within 0.2°C; changing the depth from just below the surface to full operating depth (3000 m) induced a relative phase change between hydrophones which was less than 0.6°C. The hydrophone output is applied to a very low noise FET preamplifier with 40 dB of gain. The minimum expected acoustic noise level is approximately 45 dB re 1 μPa at 100 Hz [6], and the electrical noise in the preamp is approximately 15 dB below this level. The output is filtered by a six pole low-pass phase-matched filter with a corner frequency at 220 Hz and whose in-band gain is 1. The preamp has a low-frequency cutoff below 10 Hz. A differential line driver is used to transmit the signal a distance of up to 33.75 m to a processor pressure case. There are ten elements per 75 m section with each processor receiving five inputs from the hose on either side. The two elements immediately adjacent to a processor pressure case are filtered within the pressure case rather than at the element to provide 12 kHz acoustic information required for navigating the array.

In the processor pressure case the hydrophone inputs are

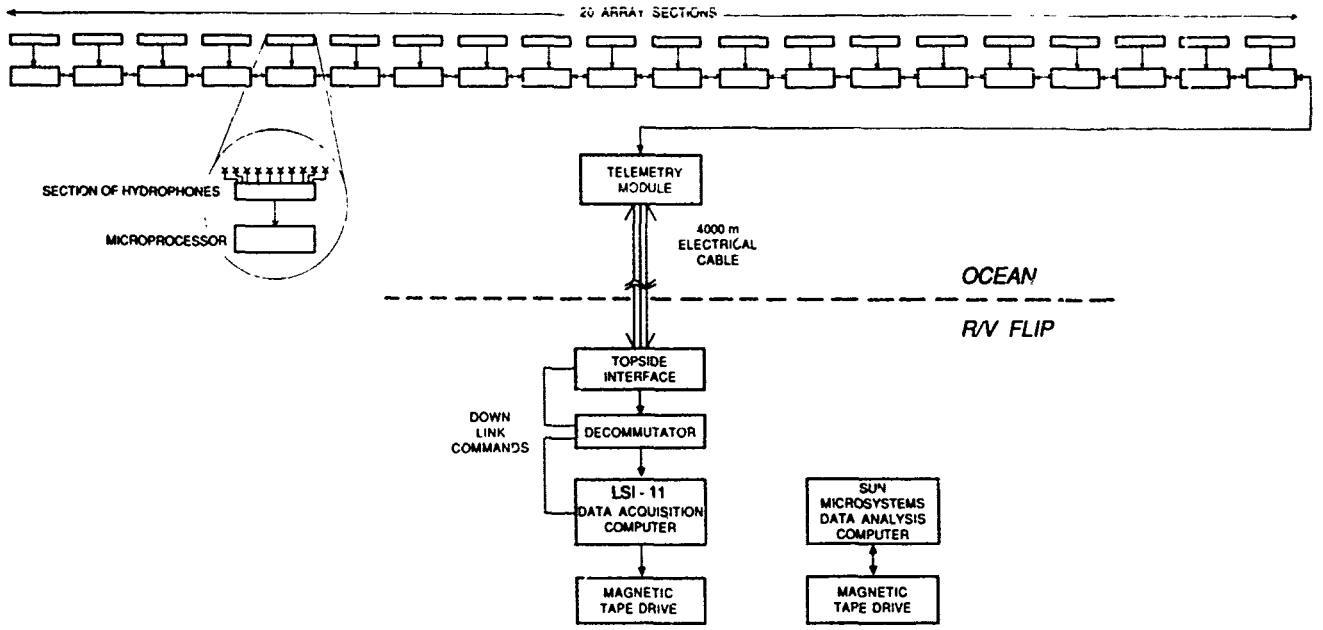

Fig. 3. Array System Diagram. The data path from the hydrophones through the telemetry module to the magnetic tape drive is shown. Further analysis of the data is accomplished by a Sun Microsystems computer.

selected sequentially by a differential multiplexer, converted from differential to single-ended signals, amplified by a programmable variable gain amplifier, captured by a sample-and-hold circuit, and converted to 12-bit digital form. The programmable analog to the digital converter (A/D) clock is synchronous with the 20 kHz downlink carrier and the A/D outputs are stored in a 16-word first-in, first-out (FIFO) register before the processor is interrupted to take the ten data words. Of the 16 bits per word stored in the FIFO, 12 bits are data, 2 bits are from the navigation detectors, and 2 bits are hardware status flags. Prior to low-pass filtering, the signals from the hydrophones adjacent to the pressure case are routed to a 12 kHz detection circuit. This circuit compares the signal level in a narrow band receiver at 12 kHz to the level of a broadband receiver to determine the presence or absence of a 12 kHz acoustic transponder signal. The 1-bit detection from each circuit is multiplexed in with every 12-bit hydrophone word as it is stored in the FIFO. The CPU is a Motorola 68000 operating at 4 MHz with 4K ROM and 2K RAM available. The 4 MHz clock is derived from a 16 MHz crystal which is phase-locked to a 1 MHz clock signal from the telemetry module. The software is interrupt driven with the highest priority interrupt responding to the A/D. The second highest priority interrupt transmits the processed data, and the lowest priority services the downlink synchronization sequence. The signal data are loaded from the FIFO into a large RAM buffer and the CPU then processes the data before presenting it to a Manchester code repeater/encoder for transmission.

The array processors are synchronized by a downlink pattern at a 500 Hz rate. At synchronization, the farthest processor from *FLIP* transmits a synchronization word and the processed data. Each sequential processor repeats the data bit stream from the processor before and inserts its data, followed by a unique ID within a specified time window. At the *FLIP* end of the array is a telemetry module which contains a Manchester decoder, a FIFO, and a synchronous data transmitter. The telemetry module converts the asynchronous data along the array to a continuous data stream up the cable to *FLIP*. It adds frame sync words and null data when the FIFO is empty or busy. The data are driven up the cable at a 1 MHz rate by a high-power amplifier (10 W) to overcome the cable attenuation of approximately 45 dB re 1 V. A bit stream containing data from all the array sections is available every 2 ms at *FLIP*.

B. Topside Electronics

This section describes the topside data acquisition system (Fig. 3). The uplink data are presented to an array interface module where they are amplified and filtered to remove cable phase distortion. A Decom Systems bit synchronizer/decommutator locks to the frame sync word in the data bit stream, and decodes the data to present it to the data acquisition computer (LSI-11). The decommutator hardware transfers data by direct memory access (DMA) to a ring buffer initialized by the LSI-11 data handler software. An 8-word header containing a buffer ID and the timing sequence information are prepended to the ring buffer prior to the transfer to magnetic tape. The tape transfer is a DMA directly from the ring buffer, thus avoiding the overhead in an intermediate-user buffer transfer. A buffer counter tracks the number of transfers and when the tape is full, the handler automatically begins accessing a second tape drive without loss of data. Confirmation of the buffer ID, buffer counter, frame sync

word, and processor ID during data processing verifies the integrity of the telemetry system.

C. Downlink Command Stream

This section describes the downlink of commands from the topside data acquisition computer to the array processors. The commands are entered at the operator terminal or from a set of switches on the array interface box and may be sent at any time while the array is operating. The maximum downlink command data rate is limited to 550 baud to ensure accuracy of transmission. Downlink commands may be specified to selected processors or broadcast to all processors. There are three categories of commands as shown in the Appendix: diagnostic, control/initialization, and data format. The diagnostic commands assist in localizing errors in individual processors. Allowable functions are to test memory, read specific memory locations, enter and execute additional machine codes, alter the processor position in the uplink bit stream, turn off the transmitter of the addressed processor so the bit stream is passed around it, and full or partial resets. The control/initialization commands modify array operational parameters. The *select* command determines the order in which hydrophones or other sensors are digitized, allowing selection of other sensors such as depth gauges. The *scan off* command causes only one hydrophone to be digitized per section. The *A/D rate* command selects the rate at which the A/D will digitize the incoming data. The *variable gain* command selects specific gain outputs of a two-stage amplifier. Gains between 5 and 1000 are obtained by selecting a gain of 1, 5, 10, or 20 from the first stage, and 5, 8, 12, or 20 from the second stage. The *data format* command determines the data format to be transmitted. The formats available transmit some combination of test data, hydrophone data, navigation data, and a processor ID. The *navigation receiver* commands select which navigation receiver signal is digitized when the choice of data format restricts the number of navigation bits transmitted.

D. Navigation

Array acoustic navigation is accomplished by detecting the return signals of near-bottom acoustic transponders [7]. A minimum set of three transponders are interrogated from *FLIP* at unique frequencies and their replies are detected by the array. The time of arrival of each reply corresponds to the range between the transponder and the array element. A set of ranges are determined for each array navigation element and input to a program which calculates the element position [8].

The transponders employed were developed for navigation of the MPL deeptow fish [9]. For navigation of the array these transponders are deployed in roughly a one nautical mile equilateral triangle about *FLIP*. They are anchored above the seafloor by a 100 m length of line. To increase the reliability of detection in a noisy environment, the receive circuitry in the transponders (as well as in the array) compares the energy in a narrow band (200 Hz effective bandwidth) about the interrogation frequency to the total energy received in a passband of approximately 1.5 kHz. By adjusting the bandwidth and Q of the recognition circuitry, a short recognition time (> 1 ms) and high-noise rejection are achieved. The interrogation signal for each transponder is unique and upon detection the transponder replies with a 3 ms 12 kHz pulse which is received and recorded by *FLIP* and the array.

The transponder locations must be surveyed to determine their relative positions before using them to navigate the array. The transponder locations are adjusted relative to an arbitary origin by an iterative approach which alternately determines ship positions from known transponder positions and transponder positions from known ship positions using a least squares approach. The initial transponder positions are derived from the GPS satellite navigation positions of the surface ship as each transponder is deployed. A data set containing slant ranges, depths, and initial positions is input to the navigation program. The difference between the calculated and measured positions defines the error.

The horizontal projection (Fig. 4) of the slant range between a given transponder and a given surface ship position (or *FLIP* or an array element) is

$$Hproj(ntr,\ npos) = \sqrt{S^2 - D^2}$$

where *ntr* indicates a particular transponder, *npos* indicates a particular fix or position of the surface ship, S is the slant range from the source to that transponder, and D is the transponder depth minus the source depth. The mean squared error is

$$E_{mse} = 1/\hat{N}\Sigma(rngxy - Hproj)^2$$

$$\text{where } rngxy = \sqrt{(x_{ss} - x_{T1})^2 + (y_{ss} - y_{T1})^2}.$$

The horizontal range *rngxy* is determined by the initial X–Y positions where x_{ss} and y_{ss} represent the position of the surface ship, and N is the number of transponders. If the RMS errors are large the position is adjusted and the process iterates. The adjustment is calculated using the method of steepest descent to follow the mean squared error gradient to a minimum. For known transponder positions, the perturbed ship position in the x direction is

$$x_{ss} = x_{ss} + hE'_{mse}(x_{ss},\ y_{ss})$$

$$x_{ss} = x_{ss} + h * (x_{ss} - x_{T1}) * (rngxy - Hproj)/(rngxy * N)$$

where x_{ss} is the surface ship position, h is the step size, and E'_{mse} is the derivative of the error function with respect to x. The y-direction adjustment is calculated similarly. When the RMS error becomes small the current position is saved.

Assuming the ship positions are known parameters, the transponder positions are adjusted using the same technique. Upon completion of the adjustment loops, the RMS error for all the transponders is evaluated. If this error is not acceptable then the RMS errors associated with each ship position are examined, and any position with an error greater than a specified value is deleted and the process begins again. This method

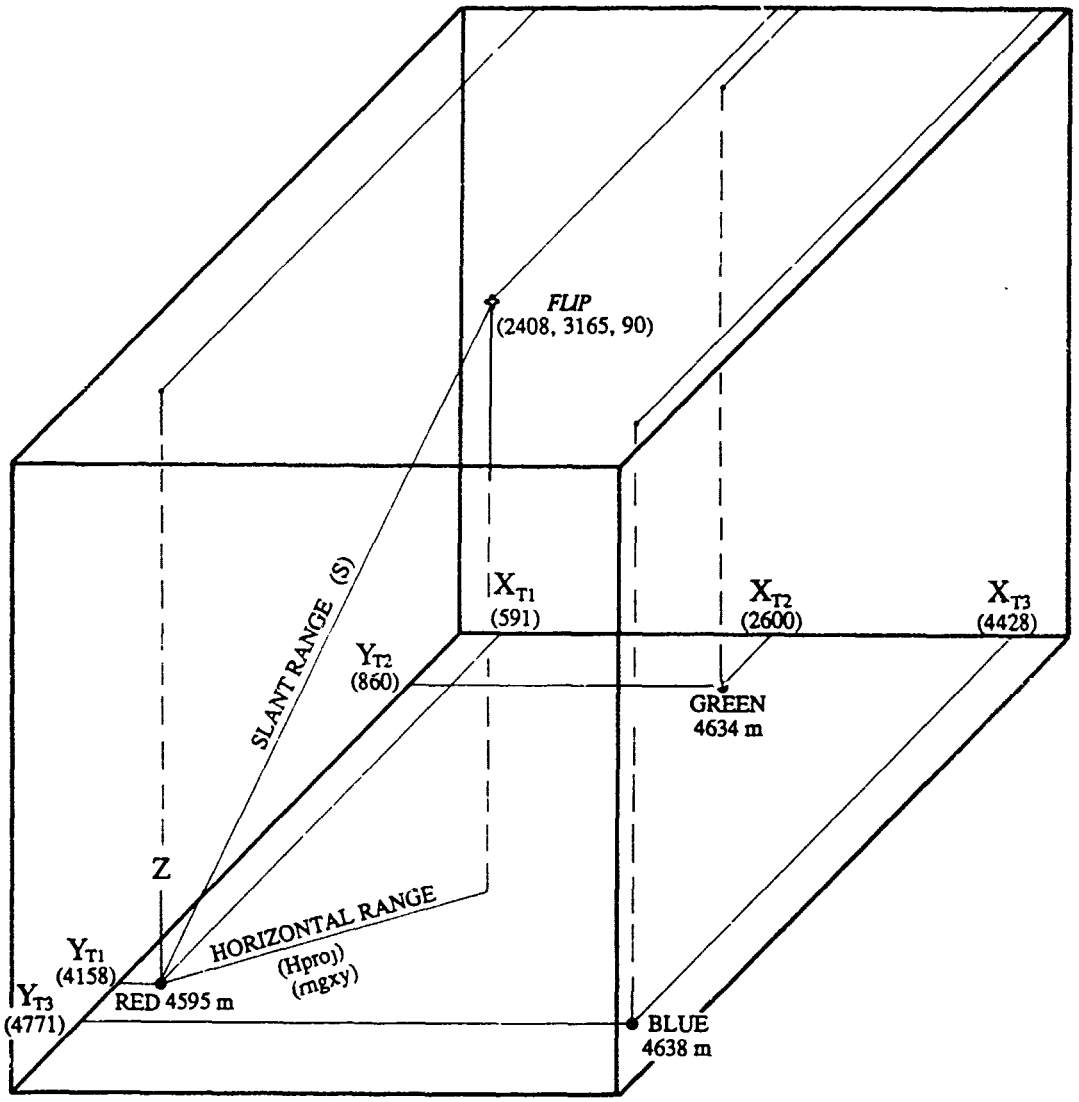

Fig 4. Navigation Overview. The horizontal projection is estimated first by using the slant range and depths (*Hproj*) and then with the initial *X–Y* positions (*rngxy*).

gives the best transponder locations in a least squares sense which are consistent with the available data.

The array and *FLIP* are navigated similarly. A hydrophone located at the bottom of *FLIP* transmits a series of transponder interrogation sequences (TIS). A TIS consists of four interrogation pulses at 10 second intervals followed by a silent interval. The first three pulses are at the interrogate frequencies of the bottom transponders (10, 10.5, and 11 kHz). Upon receiving an interrogation pulse a bottom transponder replies with a 3 ms pulse at 12 kHz. The fourth TIS pulse is at 12 kHz and is received by the array navigation elements to indicate array depth. The array therefore receives four consecutive 12 kHz pulses, whose timing indicates the transponder ranges and depth beneath *FLIP*. The array samples the 12 kHz pulses at an operator selected rate (typically 0.4 ms). The CPU decimates the data, if necessary, to provide a continuous time series consistent with the number of bits allowed for navigation. The interrogation sequence is synchronized with the data-sampling timebase in the array and the initiation time of the sequence is recorded. The navigation time series establishes the range from each navigation element to each transponder after removal of the *FLIP* to transponder ranges [10]. The ranges are corrected for a varying sound speed profile by integrating over the ray path.

Calculation of the hydrophone position begins by determining the two intersections of the horizontal projection arcs. The third transponder range determines which intersection is used as an initial position. The data are iterated as described above to reduce the RMS errors. Array element relative-location accuracies of a few meters may be achieved by this method. Examples of array element positions from the September 1987 experiment are displayed in Fig. 5, demonstrating the relative motion. The symbols represent the array at 4-hour increments spanning a 24-hour period. There is less than 1° tilt from vertical across the 900 m array aperture. The motion of *FLIP* (Fig. 5(a)) appears to be driven by the increasing northerly wind over the time analyzed (see Fig. 7(h)). The north–south motion of the array (Fig. 5(b)) is affected by the

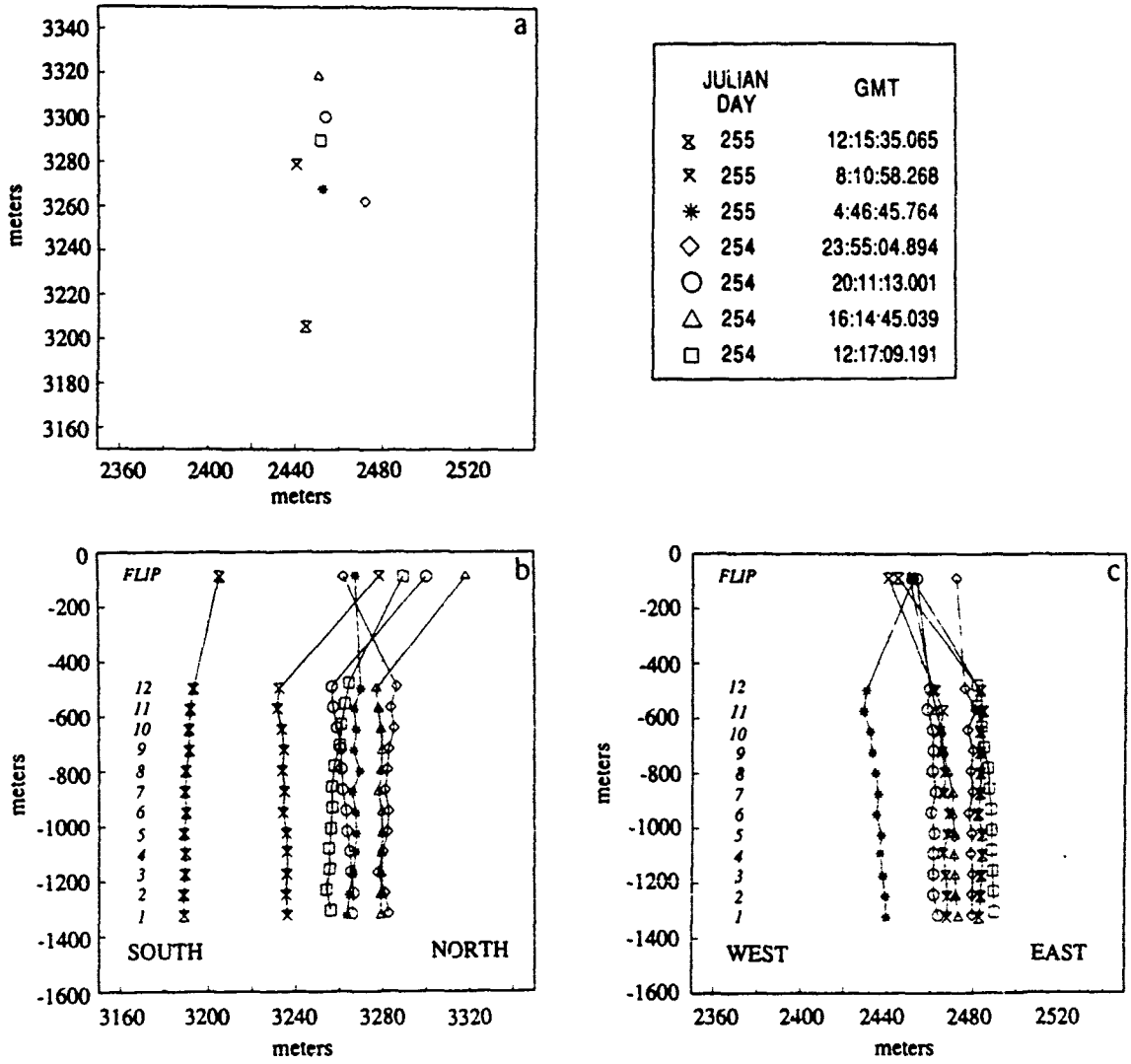

Fig. 5. Navigation Results A time series of the array position sampled approximately every four hours. The three plots represent (a) a plan view in X (increasing toward the east) and Y (increasing toward the north), (b) X versus depth, and (c) Y versus depth. The scale in (b) and (c) is enhanced in the vertical direction by 8:1.

motion of *FLIP* as well as by tidal motion. The east–west array motion (Fig. 5(c)) is primarily tidal driven, with a semidiurnal period.

III. Experimental Results

Ambient noise data are presented from an experiment conducted in the northeast Pacific during the month of September 1987. Data were collected for 20 days, approximately 400 km southwest of Monterey in 4700 m of water. The programmable data sampling rate was selected at 500 Hz. The array was deployed at various water depths spanning the water column from 400 to 3100 m. Fig. 6 shows the array depth superimposed on the sound speed profile.

Representative hydrophone spectra illustrate the ambient noise variation with depth and wind speed (Fig. 7). The local wind speed varied from 4 to 28 knots during the experiment, as shown in Fig. 7(h). The spectra were obtained by incoherently averaging 11 8192-point FFT's with 50 percent overlap of a Kaiser–Bessel ($\alpha = 2.5$) windowed time series. The nearly uniform spectral level with depth is consistent with previous investigation [1], [11]. There is a distinct difference in the spectral level as wind speed increases (Fig. 7(a)). The spectra at a nominal depth of 1300 m at low wind speed (Fig. 7(c)) and high wind speed (Fig. 7(d)) were bin-averaged and subtracted to provide a measure of wind speed dependent variations. Significant variation in ambient noise was observed for frequencies above 100 Hz and below 25 Hz. Above 100 Hz at all depths, an increasing amplitude and distinct whitening of the spectra are observed at high wind speeds. The observed spectral difference is consistent with previous observations which are diverse in this frequency band (see Table II). Another effect of the wind is the level of mechanical vibration or strum which increases with wind speed. This source is important to the spectral shape below 25 Hz at all wind speeds

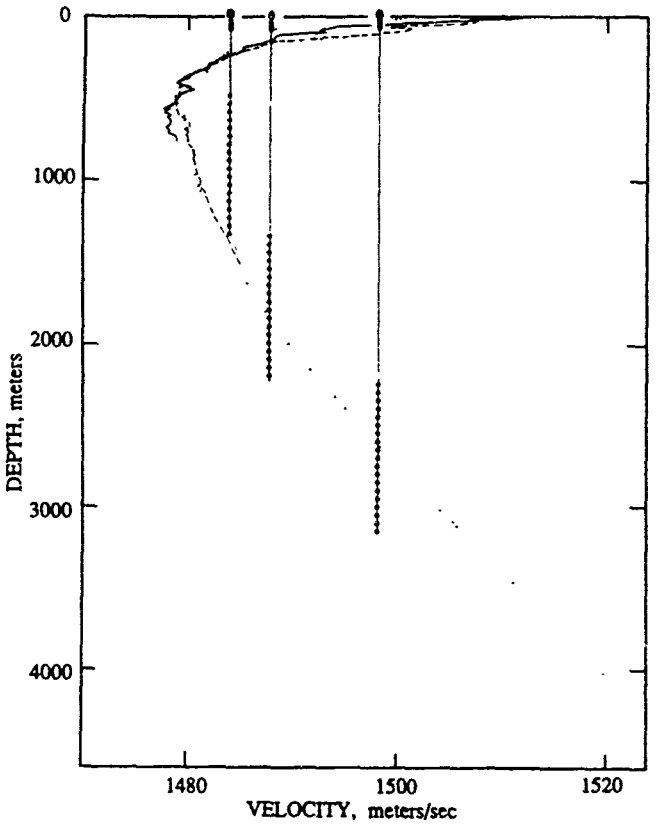

Fig. 6. Array deployment depths for the September 1987 sea test. The three curves represent (a) the historical sound speed profile (dotted) obtained from the National Oceanographic Data Center [12] for the experimental area and time of year (designated area 25C), (b) the sound speed (dashed) obtained from a conductivity, temperature, and depth (CTD) cast deployed from a surface ship approximately 40 km northwest of the array, and (c) the sound speed (solid) calculated with the Clay and Medwin [13] equation using the historical salinity data and an expandable bathymetric thermistor (XBT) deployed from *FLIP*.

but may contribute energy between 25 and 50 Hz at higher wind speeds. The bandwidth of the strum-contaminated noise increases with wind speed and decreases with depth. Preliminary analysis indicates that frequency–wavenumber filtering is effective in removing this noise source as the vibrational modes travel at velocities other than that of acoustic energy. In the band between 20 and 100 Hz the spectral amplitude was independent of wind speed. Shipping may be the dominant noise source for this band as the experiment was in an area of high shipping density. The characteristic spectral "hump" due to shipping noise was observed throughout the experiment. Narrow band 60 Hz harmonics are seen in the spectra and are generated either mechanically or electrically by *FLIP*. There was no evidence of 60 Hz lines during laboratory studies of the array self-noise. The 60 Hz harmonics are narrow band and do not degrade the broadband signal analysis.

A graphic display of the output of 120 acoustic channels recording an air gun source at a range of 500 km is shown in Fig. 8. In this plot, a compressive pressure field or positive voltage excursion is represented as a filled line, and a rarefactive pressure field or negative voltage is represented as an unfilled line. The air gun is seen as a series of impulsive arrivals that appear as both downward-propagating and upward-propagating wavefronts across the array. In addition, two modes of mechanical vibration (strum) are identified in Fig. 8. The first mode is a longitudinal vibration of the kevlar support cable, probably due to vertical motions of *FLIP* pulling on the support cable. This mode propagates with a phase velocity of 1800 m/s and appears as a downward-propagating transient in Fig. 8. The second mode is a transverse vibration of the kevlar support cable, probably excited by water currents. This mode propagates with a phase velocity of 40 m/s and appears as a series of shallow-dipping lines with an interference pattern every 75 m, corresponding to the spacing of the inline pressure cases.

The air-gun array is seen as a contaminant in the spectra of the ambient noise data in Fig. 9(a). Since the operating area of the air run array was shallow, the ocean bottom altered the arrival, part of which is coupled into the deep-sound channel by down-slope conversion and arrives at the array in a multipath structure at a variety of angles. The effect of the profiler is significant in the 125 to 250 Hz band where it dominates the spectra, clearly distorting the 10 dB/octave roll-off of the ambient noise. The profiler was extracted (Fig. 9(b)) by removing the visible signal from the array time series, padding

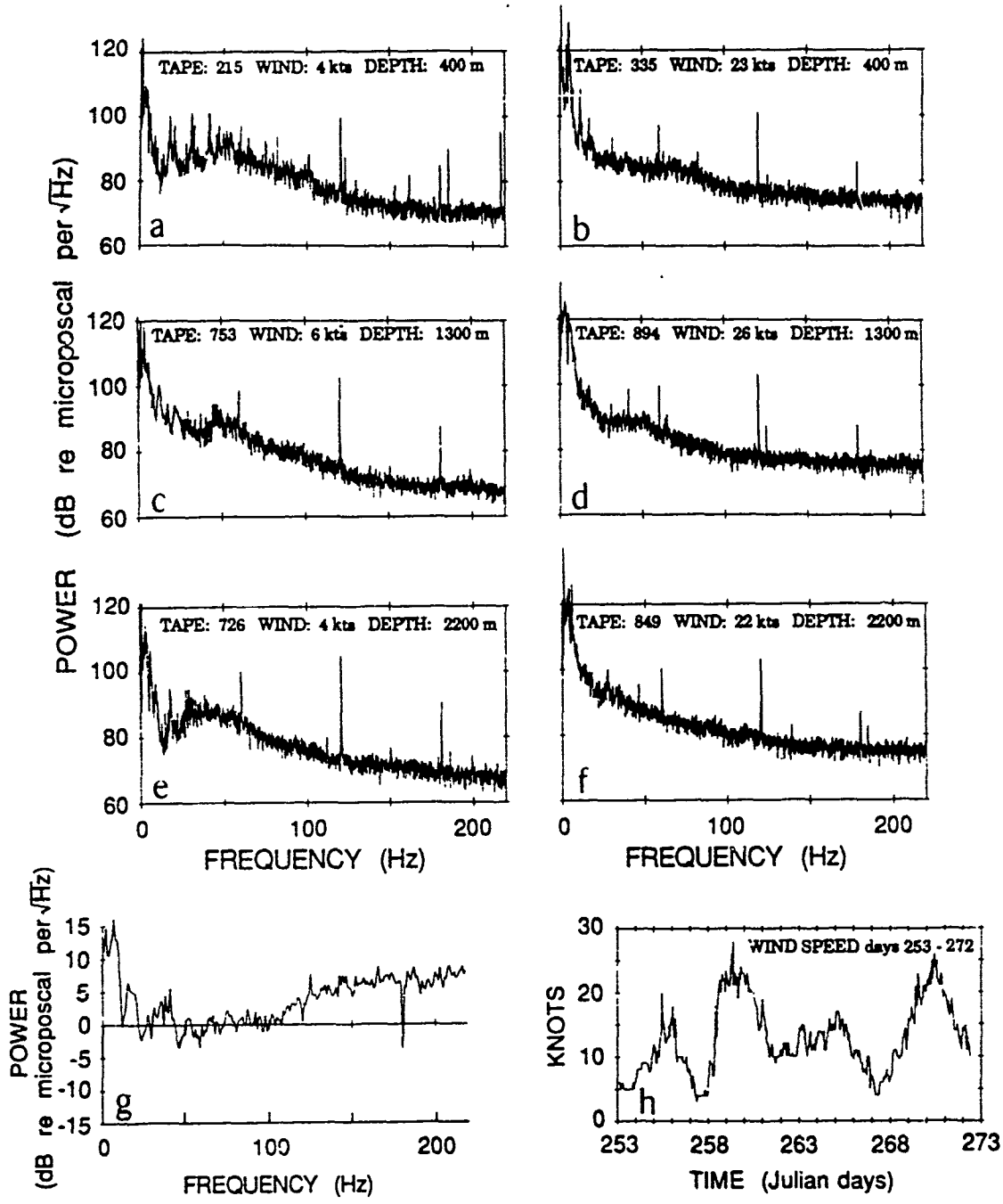

Fig. 7 Ambient Noise variation with respect to wind and depth. Depths indicated are nominal for the top of the array, the hydrophone shown is 675 m deeper. Data were extracted on different days to obtain similar environmental conditions. The narrow band signals are interference from equipment aboard *FLIP*. (a) Wind: 4 kts, Depth: 400 m, Jday: 257. (b) Wind: 28 kts, Depth: 400 m, Jday: 259 (c) Wind: 6 kts, Depth: 1300 m, Jday 267 (d) Wind: 26 kts, Depth: 1300 m, Jday: 270. (e) Wind: 4 kts, Depth: 2300 m, Jday: 267. (f) Wind 22 kts, Depth: 2300 M, Jday: 269 (g) Representative spectral difference with wind (h) Wind speed (kts) versus Julian Day (Jday)

TABLE II
AMBIENT NOISE SPECTRAL VAPIATION WITH WIND SPEED

Change in Spectral Level	Change in Wind	Frequency	Reference
dB//μPa/√Hz	kts	Hz	
+18	4-6 to 28-33	200	[1] Urick 1983
+9	10-40	200	[3] Burgess and Kewley 1983
+7	4-6 to 22-28	200	this paper 1988
+7	10-30	150	[11] Morris 1978
+5	18-28	177	[21] Shooter and Gentry 1981
+4	5-28	177	[22] Perrone 1969
0	6-22	200	[15] Hodgkiss and Fisher 1986
-4	low-high	165	[4] Wilson 1983

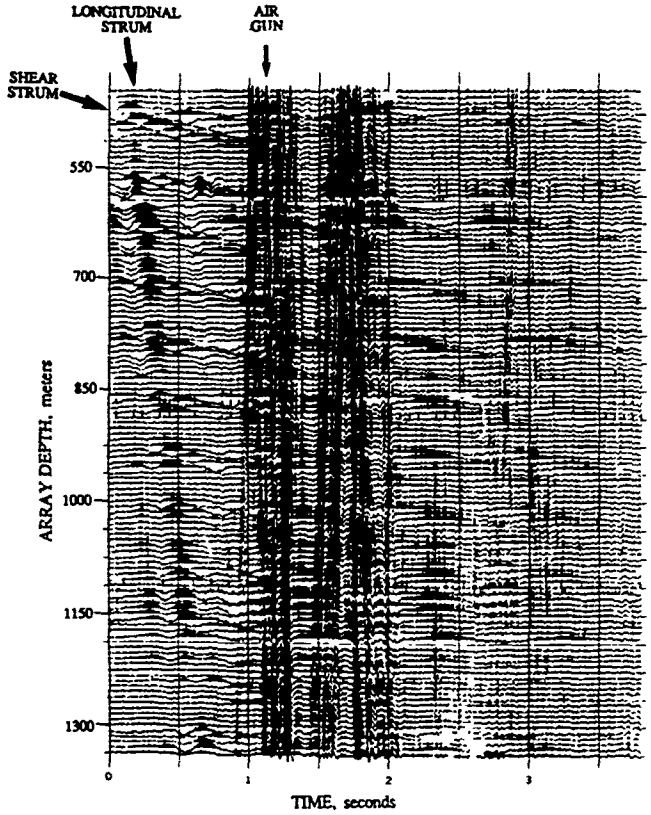

Fig. 8. Time series display of acoustic channels. A graphic display of the acoustic channels shows an air-gun source at a range of 300 miles as well as longitudinal and transverse (shear) strum modes. The time record displayed is 3.5 s. The array hydrophone depths span 400 to 1300 m.

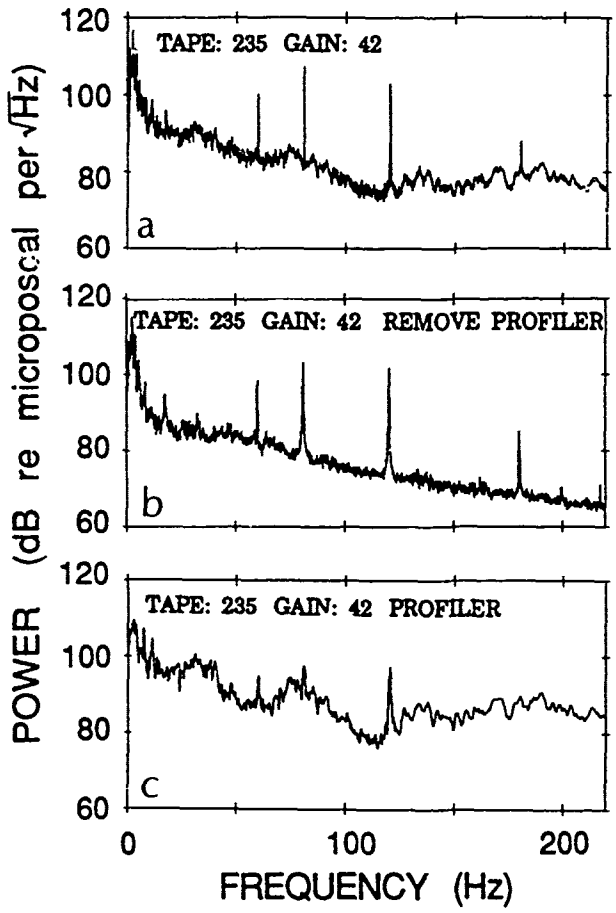

Fig. 9. Seismic profiler contamination. The effect of the air gun signal is seen to be clearly contaminating the ambient noise spectra. (a) Original data acquired at array channel 24. (b) Same data as (a) with profiler signal removed. (c) Profiler signature as seen at the array.

the remaining data to 8192 points, and producing the spectrum as described above with no overlapping. The profiler spectra in Fig. 9(c) was calculated from 800 data points and a rectangular window and shows the ambient noise spectra uncontaminated by the profiler.

IV. SUMMARY

This paper describes the low-frequency digital acoustic array designed and built at the Marine Physical Laboratory. A sea test has been conducted to verify the vertical deployment, telemetry, acoustic navigation, and ambient noise measurement capabilities of the array. Navigation of the array was conducted within an acoustic transponder net. Ambient noise spectra from single array elements were consistent with previous observations of shipping noise in the frequency band between 20 and 100 Hz. At frequencies above 100 Hz sea-surface noise generated by local wind and waves was observed. Current efforts are underway to investigate the vertical directional spectra of low-frequency noise measured by the array.

APPENDIX

Available array commands are listed below. The left-most hex number is the command byte s t by the data acquisition computer to the array. The last column indicates the type of command: Diagnostic, Initialization, or data Format.

APPENDIX
AVAILABLE ARRAY COMMANDS

41	DIAG 2 ON		memory test then full init	D
42	SHOW HWID		hwid pos swid cccc	D
43	DIAG 1 ON		analog data test	D
44	DIAG 1 OFF			D
45	SCAN ON		scans through phones	I
46	SCAN OFF		selects only one phone	I
47	SOFT INITIALIZE			D
48		OFF		I
49	AD RATE	5K		I
4A		10K		I
4B		20K		I
4C	NAV RCVR 0			I
4D	NAV RCVR 1			I
4E	ENABLE RAM PROGRAM			D
50-5F	SEL HYD N		N=0 through F	I
60		1	stage 1	I
61		5		I
62		10		I
63		20		I
64	VAR GAIN	5	stage 2	I
65		8		I
66		12		I
67		50		I
68		1000		I
69		6	send 5's (nav0) or A's (nav1)	F
6A		5	10 phones + nav	F
6B		4	2 nav words + 8 phones	F
6C	DATA FORMAT	3	10 phones	F
6D		2	test tape	F
6E		1	listen	F
6F		OFF		F
70-7F	NEW POSITION = N		N=0 through F	DI
80		OFF	get data from memory location	D
81		2000	(added sssa cccc) address, contents	D
82		2200		D
83		2400		D
84		2820		D
85		28D4		D
86		2900		D
87	DIAG 3	2940		D
88		2980		D
89		29C0		D
8A		----		D
8B		----		D
8C		2F00		D
8D		2FC0		D
8E		----		D
8F	INCREMENT ADDR IN DIAG 3 ABOVE			D
90	UPLINK OFF			D
91	UPLINK ON			D
92	STORED SINUSOID ON			D
93	STORED SINUSOID OFF			D
99	FULL RESET			D

ACKNOWLEDGMENT

The authors wish to thank F. N. Spiess, F. H. Fisher, W. S. Hodgkiss, F. V. Pavlicek, and R. C. Tyce for their help in the development of the MPL digital array. The captain and crew of the *FLIP* contributed to the sea-going operation.

REFERENCES

[1] R. J. Urick, *Principles of Underwater Sound*, 3rd ed. New York: McGraw-Hill, 1983.

[2] R. W. Bannister, R. N. Denham, K. M. Guthrie, D. G. Browning, and A. J. Perrone, "Variability of low frequency ambient sea noise," *J. Acoust. Soc. Amer.*, vol. 65, no. 5, pp. 1156-1163, 1979.

[3] A. S. Burgess and D. J. Kewley, "Wind-generated surface noise source levels in deep water east of Australia," *J. Acoust. Soc. Amer.*, vol. 73, no. 1, pp. 201-210, 1983.

[4] J. H. Wilson, "Site and frequency dependence of ambient noise in the Northeastern Pacific Ocean," *J. Acoust. Soc. Amer.*, vol. 73, no. 2, pp. 539-545, 1983.

[5] J. J. Lastinger, "Measurements on Norda/DTAG AQ-1 hydrophones," Underwater Sound Reference Detachment, Orlando, FL, Calibration Memo. 6891, 1982.

[6] G. M. Wenz, "Acoustic ambient noise in the ocean: Spectra and sources," *J. Acoust. Soc. Amer.*, vol. 34, pp. 1936-1956, 1962.

[7] M. S. McGehee and D. E. Boegeman, "MPL acoustic transponder," *Rev. Sci. Instr.*, vol. 37, pp. 1450-1455, 1966.

[8] C. D. Lowenstein, "Computations for transponder navigation," in *Proc. Nat. Marine Nav. Meet.*, 1966, pp. 305-311.

[9] F. N. Spiess, M. S. Loughridge, M. S. McGehee, and D. E. Boegeman, "Acoustic transponder system," *J. Inst. Navigation*, vol. 13, no. 2, pp. 154-161, 1966.

[10] B. J. Sotirin, F. V. Pavlicek, and J. A. Hildebrand, "Low frequency digital acoustic array," in *Current Practices and New Technology in Ocean Engineering—1988*, G. K. Wolfe and P. Y. Chang, Eds. New York: ASME, 1988, pp. 19-27.

[11] G. B. Morris, "Depth dependence of ambient noise in the Northeastern Pacific Ocean," *J. Acoust. Soc. Amer.*, vol. 64, no. 2, pp. 581-590, 1978.

[12] J. Churgin and S. J. Halminski, *Temperature, Salinity, Oxygen and Phosphate in Waters off the United States, Eastern North Pacific*, National Oceanographic Data Center, Washington, DC, vol. 3, 1974.

[13] C. S. Clay and H. Medwin, *Acoustical Oceanography: Principles and Applications*. New York: Wiley Interscience, 1977.

[14] M. J. Buckingham and S. A. S. Jones, "A new shallow-ocean technique for determining the critical angle of the seabed from the vertical directionality of the ambient noise in the water column," *J. Acoust. Soc. Amer.*, vol. 81, no. 4, pp. 938-946, 1987.

[15] W. S. Hodgkiss and F. H. Fisher, "Vertical directionality of ambient noise at 32° N as a function of longitude," Marine Phys. Lab., Scripps Instit. Ocean., La Jolla, CA, Tech. Memo 387, 1986.

[16] S. C. Wales and O. I. Diachok, "Ambient noise vertical directionality in the Northwest Atlantic," *J. Acoust. Soc. Amer.*, vol. 70, no. 2, pp. 577-582, 1982.

[17] D. G. Browning, N. Yen, R. W. Bannister, R. N. Denham, and K. M. Guthrie, "Vertical directionality of low frequency ambient noise in the south Fiji Basin," Naval Underwater Sys. Ctr., New London, CT, Tech. Doc. 6611, 1982.

[18] R. C. Tyce, "Depth dependence of directionality of ambient noise in the North Pacific. Experimental data and equipment design," SACLANTCEN, La Spezia, Italy, Doc. CP-32, 1982.

[19] V. C. Anderson, "Variation of the vertical directionality of noise with depth in the North Pacific," *J. Acoust. Soc. Amer.*, vol. 66, no. 5, pp. 1446-1452, 1979.

[20] E. H. Axelrod, B. A. Schoomer, and W. A. Von Winkle, "Vertical directionality of ambient noise in the deep ocean at a site near Bermuda," *J. Acoust. Soc. Amer.*, vol. 37, no. 1, pp. 77-83, 1985.

[21] J. A. Shooter and M. L. Gentry, "Wind generated noise in the Parece Vela Basin," *J. Acoust. Soc. Amer.*, vol. 70, no. 6, pp. 1757-1761, 1981.

[22] A. J. Perrone, "Deep-ocean ambient-noise spectra in the Northwest Atlantic," *J. Acoust. Soc. Amer.*, vol. 46, no. 3, pp. 762-770, 1969.

★

Barbara J. Sotirin received the B.S. degree in electrical engineering from San Diego State University, San Diego, CA, in 1980 and is currently a Ph.D. candidate in electrical engineering (applied ocean science) at the University of California, San Diego.

Her research interests include low frequency acoustic instrumentation, ocean ambient noise, and arctic acoustics.

★

John A. Hildebrand received the B.S. degree from the University of California, San Diego, in 1978 and the Ph.D. degree from Stanford University in 1983.

In 1983 he joined the Marine Physical Laboratory of the Scripps Institution of Oceanography, University of California, San Diego, where he is currently an Assistant Professor. His research interests include low frequency acoustics, ocean bottom seismology, and ocean bottom gravimetry.

Acoustic navigation of a large-aperture array

Barbara J. Sotirin and John A. Hildebrand
Marine Physical Laboratory, Scripps Institution of Oceanography, University of California, San Diego, La Jolla, California 92093

(Received 11 April 1989; accepted for publication 4 August 1989)

Acoustic travel time measurements were used to navigate the elements of a large-aperture (900 m) acoustic array. Array navigation system performance was evaluated during a vertical deployment in the northeast Pacific from the Research Platform FLIP. A network of bottom-moored acoustic transponders were interrogated from FLIP and their 12-kHz replies were detected by receivers at 75-m intervals along the array. A nonlinear least-squares algorithm was used to estimate FLIP and array element positions from the travel time measurements. The FLIP positions derived from this procedure agreed with positions obtained from global positioning system (GPS) satellite navigation to within a 10-m rms error. Navigated positions for FLIP were internally consistent with a 0.5-m mean rms error and standard deviation of 1.1 m, and, for an array element, were consistent with a 2.8-m mean rms error and standard deviation of 0.8 m. The resulting time series of array and FLIP motions were analyzed with respect to wind, tidal, and internal wave forcing functions. Wind and tidal forcing had the greatest influence on FLIP motion, whereas array motion was governed by FLIP movement, tides, and higher frequency sources. Low-frequency array motion, with periods on the order of hours, was a result of FLIP towing the array over a horizontal range of 300 m in response to the wind and the semidiurnal tidal oscillations; the array remained within a 30-m horizontal range of FLIP's position. Higher frequency array motion had apparent internal wave and surface-coupled components. The array shape was primarily straight and nearly vertical, to within approximately a 2° tilt, responding as a simple pendulum with small displacements.

PACS numbers: 43.30.Tg, 43.30.Pc

INTRODUCTION

Large-aperture arrays produce high-resolution directional information by coherently combining signals from individual array elements. Estimates of array shape and element position are required because of the dependence of signal phase on element location. Navigation of such an array in the ocean requires a known reference system in a spatially and temporally varying environment.

A 900-m, 120-element low-frequency acoustic array has been developed by the Marine Physical Laboratory.[1] The array is capable of being deployed either horizontally or vertically up to an ocean depth of 6000 m. Navigation of the array is an important part of its operational requirements, and the subsystem implemented to perform the navigation must meet design specifications. The position accuracy required is on the order of a a few meters, the duration of deployment is on the order of a few months, an operating range of up to 10 km must be viable, the size and cost of the system must be manageable, and the sampling rate must be sufficient to resolve array dynamics due to water currents, tides, wind, and internal waves.

Techniques commonly used in ocean positioning systems are based on mechanical, electromagnetic, or acoustic signals.[2] Mechanical positioning devices capable of the accuracy required include inertial systems, pressure sensors, tilt meters, measuring rods, and sound-velocity meters. The cost and size requirements of instrumenting a 900-m array with such sensors is prohibitive, although pressure sensors would be valuable for depth positioning in combination with an alternative method for lateral positioning. Electromagnetic systems are either surface systems whose signals are highly attenuated in water, but are useful in determining the position of a surface vessel [e.g., global positioning system (GPS)], or pulsed laser systems, which are currently under development and may eventually be effective within a 1-km range. The technique most easily adapted to a large-aperture array deployed in the water column is acoustic navigation. Such systems measure the travel time of acoustic energy between two points in the ocean, are capable of resolving a few meters over a 10-km range, and are cost effective and physically manageable. Based on these considerations, an acoustic navigation subsystem was implemented as an integral part of the array.

This paper describes the array acoustic navigation system and its operation during a vertical deployment from research platform FLIP in the northeast Pacific during September 1987. We describe the hardware system and acquisition of travel time measurements and associated errors, the nonlinear least-squares estimation of array spatial positions, and the analysis of FLIP and array time-varying positions during the deployment.

I. TRAVEL TIME MEASUREMENTS

Acoustic travel time measurements provide range information between the array and a set of fixed transponders. Ranges to three or more transponders are required to calculate FLIP position and array position and shape. The navigation hardware consisted of three bottom-moored acoustic

 0001-4966/90/010154-14$00.80 © 1990 Acoustical Society of America

transponders, two transmit/receive timing units mounted on FLIP (one used for FLIP navigation and the other used for array navigation), an interrogator/receiver located at the bottom of FLIP, and 12-kHz acoustic detectors distributed along the array. At a known time, an interrogation signal is transmitted from FLIP. This signal triggers a transponder reply, which is then detected by the array or the FLIP receiver systems. The travel times between the transponders, FLIP, and the array detectors determine array position and shape.

During the September 1987 experiment, three navigation transponders were moored in 4700 m of water distributed as a 1.4-nmi. equilateral triangle. FLIP's position was maintained in the middle of the transponder network by a three-point moor (Fig. 1). The transponders were deployed by a surface support ship operating a GPS satellite navigation receiver for absolute positional information. The transponders were equipped with anchors (175 kg) to secure them to the ocean floor and to constrain the horizontal movement during descent (sink rate of approximately 1 m/s). Once anchored, they were buoyed up above the anchor on 100-m lines with 130 kg of hard floats to limit horizontal movement and to insure a well-separated bottom bounce. They operate by detecting a unique interrogation frequency and answer with a 3-ms reply at 12 kHz with a source level of 190 dB *re*: 1 μPa at 1 m. The recognition delay time is 0.5–3 ms, depending upon the signal-to-noise ratio of the interrogation pulse.[3] Due to the proximity of FLIP, the absence of other local high-frequency ambient noise sources, and the manual control of the signal level on the interrogator, a constant delay time of less than 1 ms was assumed.

The interrogation pulse was sent from a transceiver mounted on the bottom of FLIP (90 m in depth). The pulse level was adjusted manually above the ambient noise for consistent transponder replies. The pulse was triggered by either a chart recorder to navigate FLIP or by an interrogation circuit to navigate the array. The chart recorder trace, set on a 1-s sweep rate, displayed the 12-kHz transponder reply amplitudes in a 500-Hz band with a transmit/receive delay time of 0.1 ms. Each transponder was interrogated individually to facilitate identification and transmitted a reply pulse once per second for 45 s. Since the FLIP transducer was also used as an interrogator for the array navigation system, only one system was operable at a time; consequently, the FLIP navigation data were recorded only once an hour during the sea test. Round-trip travel times for navigating FLIP were measured by hand from the chart recorder output with an estimated rms error of 2–3 ms.

The 900-m array was deployed vertically from FLIP with a 420-kg weight attached to maintain a nearly vertical orientation. The array navigation subsystem was composed of 12 hydrophones with 75-m spacing monitored by 12 individually programmable processors. Each of the 12 processors contained tuned navigation receivers designed to detect the 12-kHz transponder reply in a 200-Hz band with a -6-dB minimum signal-to-noise ratio. Once per minute the transceiver on FLIP sent out four continuous wave (cw) pulses: three transponder interrogation pulses at unique fre-

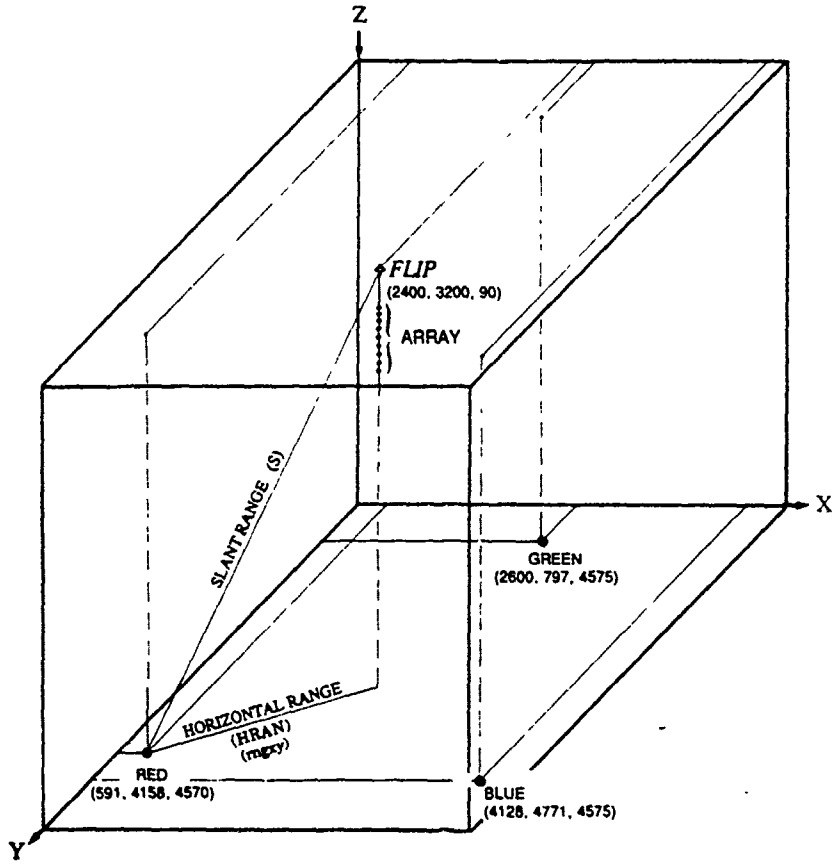

FIG. 1. Navigation overview. The navigation system consists of three bottom-moored transponders in an equilateral triangle about FLIP and the vertical array. The transponders are designated by color: red, green, and blue. The initial *xyz* coordinates of the transponders and of the FLIP interrogator are indicated.

quencies, followed by a 12-kHz pulse for depth ranging. The 12-kHz transponder replies (3 ms) and the 12-kHz depth ranging pulse from FLIP (10 ms) were recorded in series as a 1-bit output, every 0.4 ms, by each of the array navigation receivers.[4] The interrogation sequence clock was synchronized with the array time base and recorded every 128 ms.

To calculate the travel time, the time of the transponder return must be determined relative to the time of the interrogation. The signal that initiated the interrogation sequence was found by linear interpolation of the interrogation sequence clock. The leading edge of the return pulse was found by recreating each of the navigation receiver time series, and correlating these binary time series with a pulse replica that depended upon array receiver noise and level of detection. A 1-s time interval of the normalized correlation output from each array section is shown for each transponder in Fig. 2. The correlated arrival across the array of each transponder reply is evident, interference and noise are also evident. To reduce the chances of detecting a noise spike or multipath return rather than the direct transponder reply, a window was invoked, for each expected return, during which time the data were considered valid, as shown by the small ×'s in Fig. 2. The window was allowed to track the replies as the arrival time shifted with array movement. The travel time from the transponder to the array is the difference between the departure time of the interrogation pulse and the arrival time of the transponder reply at the leading edge of the correlated signal, minus the travel time from FLIP to the transponder and the constant system delay times.

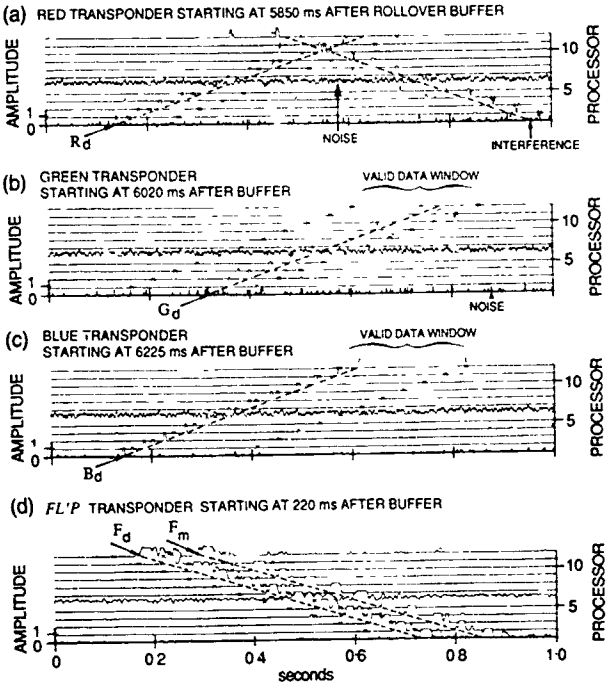

FIG 2 Travel time acquisition. The 12 array navigation receivers each detect four pulses during a 65 536-s navigation cycle. The normalized correlated receiver outputs are shown during a 1-s interval bracketing each detection. The top trace represents the output of the top receiver, followed in sequence by the deeper receivers. The first three panels, (a)–(c), represent the detected direct replies of the three transponders (shown as R_d, G_d and B_d), arriving at the deepest receiver first and traveling up through the water column to the shallower receivers. The last panel (d) shows the detection of the direct arrival F_d of the 12-kHz pulse transmitted from FLIP traveling down the array, with a surface reflection F_m arriving about 120 ms after the direct pulse. The small ×'s represent the valid data window. The start time is indicated at the top of each panel.

The accuracy of the travel time measurements from the bottom transponders to the array was dependent upon factors which affected all receivers similarly as well as factors which varied with each array receiver. The factors with similar effect were: (a) the ambient ocean noise in the 12-kHz band, which has a typical level of 30–40 dB//μPa/$\sqrt{\text{Hz}}$, and (b) the transponder performance, which introduced timing errors.[4] The factors that varied with receiver were (a) the drift in the array clock phase lock loop circuitry,[1] which introduces small sampling time errors, (b) the FLIP-to-transponder travel time measurement error (the resultant error in array-to-transponder range increases as depth decreases) of order 1.5 ms, and (c) the noise and detection threshold of the array receivers. The variation in receiver error[4] is confined for the most part to a mismatch in detection threshold due to the temperature sensitivity of the capacitors and high failure rate of the inductors in the tuned navigation filters. This variation was estimated at 2 ms during laboratory tests of the frequency sensitivity of the tuned filters and by examining the length of the transponder replies. Estimated accuracy for the array travel time measurements depends upon the receiver and the depth of the array, but is typically 2–3 ms. The accuracy of the depth measurements is affected by the ambient ocean noise, the transmitter and detector noise, the detection threshold, and the strength of the transmission. Measurement error in the travel times corresponding to array depth is estimated, by calculating the mean standard deviation in ten sample segments, to be < 1 ms.

II. POSITION ESTIMATION

In this section we determine where the three bottom transponders, the FLIP transceiver, and the array elements are in three-dimensional space using the travel times described in the previous section. The general problem of fitting model functions and parameters (spatial positions) to data (travel times) appears in many areas of applied science: as parameter estimation, regression analysis, inverse problems, filtering, process identification, and as an optimization problem in numerical analysis. Noise in the travel time measurements demands that sufficient data be collected to overdetermine the solution, requiring some kind of approximation method.

To approximate the solution, an optimization problem is defined to minimize differences between model predictions and actual measurements. The function relating predictions and measurements is determined by the problem structure and the error distribution. One approach is to minimize the differences with respect to a matrix norm. Analytically, the most viable choice is the l_2 norm resulting in the familiar least-squares solution. If the errors are independent and distributed normally with a constant standard deviation, then the l_2 norm coincides with the maximum-likelihood solution. The least-squares solution magnifies the effect of large errors, and if the error distribution contains many outliers, the l_1 norm solution as described by Gill *et*

al.[5] and implemented by Duckworth[6] is an attractive alternative. Although the l_1 solution is more robust in terms of outliers, these errors continue to affect the solution, and if possible, the source of the large errors should be identified and removed.

The navigation problem discussed here has been implemented in terms of the least-squares method. The transponder net was localized separately to allow accurate real-time array navigation. The FLIP travel time measurements used for the transponder localization are very consistent and possess no large errors, having been selected and verified by hand. *A priori* knowledge of array measurement errors did not justify deviation from the assumed normal distribution. In the remainder of this section, a general description of the least-squares formulation is followed by the specific details of implementation for the array navigation problem. The effect of specific types of errors are simulated, and results are presented.

A. Least-squares formulation

The FLIP, array, and transponder positions were estimated by a nonlinear least-squares method. The problem is to find the set of model parameters (spatial positions), given a set of measurements (travel times) plus noise. The least-squares estimator identifies a realistic set of parameters by minimizing the sum of the squared errors, with an error defined by the difference between the model estimate and the measurement. For the set of measured data v_k (travel times), and the set of parameters a_j (spatial positions) that determine the model estimate $\hat{v}_k(a_j; j = 1,N)$ (referred to as $\hat{\mathbf{v}}$ or $\hat{v}_k$), the least-squares formulation is written as

$$\underset{\mathbf{a}\in R^N}{\text{minimize}}\left(\mathbf{F}(\hat{\mathbf{v}};\mathbf{a}) = \sum_{k=1}^{M} \frac{(v_k - \hat{v}_k)^2}{\sigma^2} = (\mathbf{v}-\hat{\mathbf{v}})^T\mathbf{R}^{-1}(\mathbf{v}-\hat{\mathbf{v}})\right), \tag{1}$$

where the measurement errors are uncorrelated with identical variances σ^2 and $\mathbf{R}$ is $\sigma^2\mathbf{I}$. The error function $\mathbf{F}(\hat{\mathbf{v}};\mathbf{a})$ (designated as $\mathbf{F}$), is minimized when the gradient $\mathbf{g}$ of $\mathbf{F}$ with respect to the model parameters is zero:

$$\mathbf{g} = \frac{\partial \mathbf{F}}{\partial \mathbf{a}} = -2(\mathbf{v}-\hat{\mathbf{v}})^T\mathbf{R}^{-1}\frac{\partial \hat{\mathbf{v}}}{\partial \mathbf{a}} = 0. \tag{2}$$

In general, a closed-formed (one-step) least-squares solution exists, provided the set of equations is linear. For the array navigation problem, however, the nonlinear mapping from measurement space to parameter space necessitates an iterative implementation. One such implementation is to approximate the smooth nonlinear functions described by $\mathbf{F}$ with a linear form of the Taylor's series expansion about an initial position $\mathbf{a}_I$. In the immediate neighborhood of $\mathbf{a}_I$,

$$\mathbf{F}(\hat{\mathbf{v}};\mathbf{a}+h\mathbf{p}) = \mathbf{F}(\hat{\mathbf{v}};\mathbf{a}_I) + \sum_{j=1}^{N} hp_j \left.\frac{\partial \mathbf{F}}{\partial a_j}\right|_{\mathbf{a}_I}, \tag{3}$$

where h is a scalar, and $\mathbf{p}$ is a direction vector guiding the search for a minimum. In terms of the iteration step the notation may be written

$$F_{n+1} = F_n + h_n\mathbf{g}_n^T\mathbf{p}_n, \tag{4}$$

where $\mathbf{g}_n$ is the gradient of $\mathbf{F}$ at $\hat{\mathbf{v}}_n$. An acceptable minimum for $\mathbf{F}$ is obtained by calculating the estimate $\hat{\mathbf{v}}$ from an initial "best guess" for the parameters $\mathbf{a}_I$, then developing a prescription which improves this initial guess, updating the parameters until specified convergence criteria are satisfied. A typical prescription to search for this minimum is to calculate $\hat{\mathbf{v}}$ from $\mathbf{a}_I$, F_n from $\mathbf{v}$ and $\hat{\mathbf{v}}_n$, and complete the following steps:

(1) Compute a vector $\mathbf{p}_n$, which is the search direction.

(2) Compute a scalar step length h_n.

(3) Update the estimate of the parameters. Set $\mathbf{a}_{n+1} = \mathbf{a}_n + h_n\mathbf{p}_n$, followed by $n \leftarrow n+1$, such that the current error function is now F_n.

(4) Test for convergence. Calculate the forward problem, which determines current estimates $\hat{\mathbf{v}}_n$ of the measurements $\mathbf{v}$ from current estimates of the parameters $\mathbf{a}_n$. Evaluate F_n and F_{n-1} with respect to the convergence criteria. If the conditions for convergence are satisfied, the current value of $\mathbf{a}_n$ is considered the solution; if not, iterate by returning to step (1).

To implement this prescription, the choice of convergence criteria, search direction, and step length must be considered; particular choices relating to array navigation will be specified in the following section. In an optimization problem, the value at the minimum is generally not known, and convergence criteria must be developed to bound the number of iterations while insuring that the resulting solution is sufficiently close to the real minimum. Specific criteria are defined by evaluating the magnitude of the gradient, the magnitude of the squared error, and the relative decrease in squared error with respect to acceptable tolerances δ_i as follows:

$$\begin{aligned} &||\mathbf{g}_n|| < \delta_1, \\ &F_n < \delta_2, \\ &0 < F_{n-1} - F_n < \delta_3, \\ &\text{number of iterations} > 1/\delta_4. \end{aligned} \tag{5}$$

Combinations of the above criteria determine convergence. The rate of convergence depends on the specific minimization algorithm, the initial estimates, and the error surface. The resulting minimum point could be either global or local. In general, there are no sure methods for finding global minima; so the accuracy of the initial guess is important.

Consider the iterative step in the direction of search $\mathbf{p}_n$. In the univariate case, the only possible directions are positive or negative. As the number of dimensions increases, even to two, the number of possible directions is theoretically infinite. Search direction procedures are typically direct search methods or gradient search methods with the constraint that $\mathbf{p}_n$ be a descent direction. Iterative search procedures having the general form of Eq. (4) lend themselves easily to gradient search methods. To define the gradient search, if $\mathbf{g}_n$ is nonzero, there must exist a vector $\mathbf{p}_n$ such that $\mathbf{g}_n^T\mathbf{p}_n < 0$. If $\mathbf{p}_n$ is defined as $-\mathbf{g}_n$ and the gradient is nonzero, this direction is clearly a descent direction; the algorithm is recognized as the steepest descent method. It follows from Eq. (4) that, for any small positive step size h, $F_{n+1} < F_n$. Since $\mathbf{p}_n$ is in the direction of decreasing $\mathbf{F}$, con-

vergence is guaranteed provided h_n is chosen so that F is "sufficiently decreased" at each iteration. To be appropriate, h_n must be small enough to locate the minimum precisely and satisfy the immediate neighborhood constraint of Eq. (4), and at the same time large enough to search efficiently. The existence of guaranteed convergence of the algorithm does not imply that convergence will be achieved in an acceptable number of iterations A common method used to define h is to follow the steepest descent gradient for the current iteration to a minimum. This dictates that the next search direction be nearly orthogonal to the current direction $\mathbf{g}_n^T \mathbf{p}_{n+1} \rightarrow 0$. It has been shown that the directions generated by this method asymptotically converge to only two directions for many problems,[7] increasing the number of iterations immensely. This situation may be avoided by constraining the step size to be less than that required to reach the minimum in the current search direction. Although the rate of convergence of the steepest descent algorithm is known to be less than other methods,[5] the method is numerically stable and produces efficient results for the navigation problem considered here.

B. Implementation

We discuss implementation of the general nonlinear least-squares method described above for the transponder and array navigation. The ingredients required for a least-squares problem are: (1) the measurements v (travel time detected at the array and at FLIP), (2) the initial estimates of the model parameters a represented by FLIP, array, and transponder xyz positions; (3) the mapping function from measurement space to parameter space which calculates the estimates $\hat{\mathbf{v}}$ from the parameters a; and (4) the measurement errors σ. Although the general prescription is the same for the transponder localization and for the FLIP/array localization, there are differences in the implementation. In the following, the explicit inputs and implementation of the transponder localization are specified and the differences relating to FLIP and the array are discussed separately.

1. Transponder localization

The two-way travel times between FLIP and the transponders were used for transponder xy position estimation Normally, data from an extensive surface ship survey would be available for localizing the transponders.[8,9] Although such a survey was conducted during the experiment, the data were not complete due to extreme noise levels of the surface ship; instead data recorded by the FLIP navigation system were used. The FLIP data set defines a survey configuration that is not optimal; however, the extended time series and low errors of the FLIP measurements increase their reliability over the other available data sets The unconventional geometry of these measurements imparts a rotational symmetry to the problem, as FLIP was moored in the center of a roughly equilateral triangle defined by the transponder positions. This physical constraint limits the amount of independent xy information which is contained in the measurements and tends to destabilize the problem. Our results were achieved by choosing well-constrained initial estimates of the xyz positions described below, by fixing the z component during the xy iteration, and by perturbing the FLIP positions independently of the transponder positions. Although the discussion of the general least-squares method was described in terms of measured and estimated travel times, the actual implementation described here was in terms of horizontal ranges. Describing the implementation in terms of the variables introduced in Eqs. (1) and (2), the model parameters $a_j, j = 1,N$ are the x and y positions of the FLIP transceiver and the three bottom transponders, these x and y positions define the horizontal projection of the slant range from a specified transponder to FLIP which is designated $\hat{v}_k$, $k = 1,M$. The measured travel times are converted to horizontal projections designated v_k, $k = 1,M$, using the sound-speed profile and the fixed z components as shown below The number of horizontal projections, M, is 3 for the FLIP perturbations and 424 for the transponder perturbations

The conversion from the time domain to the space domain is dependent on the sound-speed profile between the specified depths. Assuming a constant sound speed and therefore a straight-line path, and expanding the v_k's for illustrative purposes, the measured travel time is related to the xyz position as

$$\text{measured travel time} = \tfrac{1}{c}\,(\text{slant range}),$$

$$\text{slant range} = \left[(x_t - x_r)^2 + (y_t - y_r)^2 + (z_t - z_r)^2\right]^{1/2}, \tag{6}$$

$$\text{horizontal projections} = \left[(\text{slant range})^2 - (\delta z)^2\right]^{1/2}$$

$$= \left[(x_t - x_r)^2 + (y_t - y_r)^2\right]^{1/2},$$

$$v_k = \hat{v}_k,$$

where c is the sound speed, x_t, y_t, z_t represent the transmitter position, and x_r, y_r, z_r represent the receiver position. Sound speed is not constant in the ocean environment, and a varying sound-speed profile refracts acoustic energy; however, under certain conditions the harmonic mean, defined below, may be used with minimal error To estimate the travel time differences due to refraction effects, the configuration parameters of the September experiment were specified and employed as inputs to the generic sonar model (GSM).[10] The GSM used generalized ray theory to calculate the ray path and travel time between a transmitter–receiver pair by assuming a sound-speed profile with layers of constant gradient. The simulation results are presented in Table I, which shows the travel time between an estimated transponder position and the array for a 12-kHz signal as a function of range, depth, and sound-speed profile The first column (right of the double vertical bar) represents the results generated by assuming a constant sound speed of 1500 m/s throughout the water column. The second column was calculated using Eq. (8) shown below, with historical values of temperature and salinity versus depth for the area covering the experiment site and at the same time of year.[11] The third column used the harmonic mean, calculated by numerical integration of the layered sound-speed profile over depth to estimate travel time which is then converted to speed

$$c = (z_T - z_0) \Big/ \int_{z_T}^{z_0} \frac{dz}{C(z)}. \tag{7}$$

The $C(z)$ profile used in the equation above is shown in Fig.

TABLE I. Sound-speed impact on travel time predictions

Horizontal range (m)	Receiver depth (m)	Travel time versus sound speed, depth, and range: 4573-m source depth, 12 kHz GSM travel time predictions using: Constant profile (1500 m/s) (s)	Historic profile (s)	Harmonic mean (s)	Deep ctd (s)
2000	90	3 2724	3.2740	3 2733	3.2733
2600		3.4546	3 4563	3 4556	3.4555
2000	400	3.0848	3.0839	3 0834	3 0833
2600		3 2774	3 2765	3 2759	3 2758
3000		...	..	3.4243	3.4241
5000		. .	...	4 3387	4.3382
10000		...	...	7.2181	7.2152
2600	1600	2.6325	2.6184	2.6175	2.6174
2600	2800	1.0972	1.0726	1.0717	1 0716

3 and was calculated using the Unesco equations[12] relating conductivity to practical salinity, sound speed to salinity, temperature and pressure, and pressure to depth. The conductivity, temperature, and pressure measurements were obtained from a surface ship on Julian day 267 at 2243 GMT within 1 nmi. of the FLIP location. Sound-speed profiles in the ocean are typically very stable below the thermocline

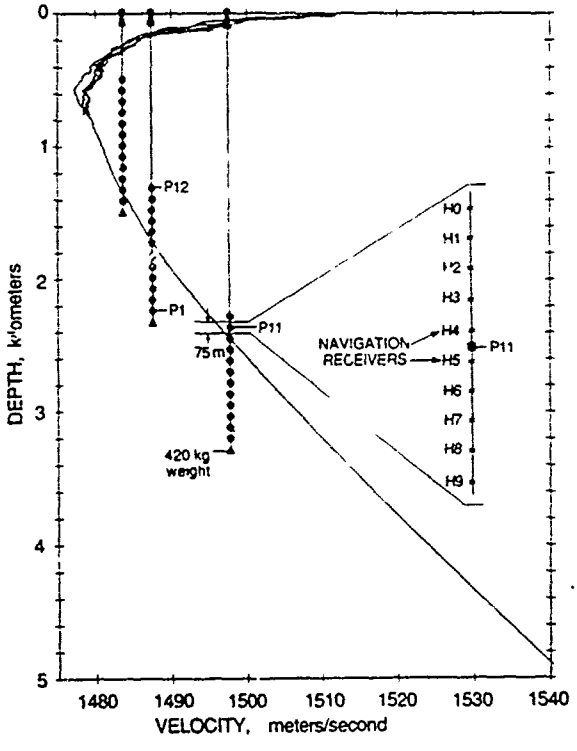

FIG. 3. Array navigation receivers and sound-speed profiles. The array was deployed at three nominal depths during the September 1987 experiment. The sound-speed profile is used in the conversion from travel times to spatial position. This profile was calculated from CTD data (0–4900-m depth) and is shown with three profiles calculated from XBT data (0–700-m depth) chosen to illustrate the variation in sound speed in the upper ocean layer. The navigation data from one receiver per array section (H5) were recorded during the experiment.

over the time period of the sea test. The diversity in temperature at the surface, however, imparts temporal variations in the sound-speed profile. Temperature measurements were acquired from expendable bathythermograph (XBT) casts deployed from FLIP twice a day throughout the experiment. Temperature data were converted to sound speed and decimated to maintain compatibility with program inputs. This conversion utilized historical salinity data[11] and was implemented by means of the following equation[13]:

$$c = 1449.2 + 4.6T - 0.055T^2 + 0.000\,29T^3 + (1.34 - 0.10T)\,(S - 35) + 0.016z, \quad (8)$$

where c = sound speed (m/s), T = temperature (°C), S = salinity (ppt), and z = depth (m). The maximum difference in the harmonic mean due to time variation in surface temperatures was about 1.5 m/s (0.1% of the mean speed). This affects the predicted travel time from a transponder to a receiver at 90 m by about 3 ms (5 m). An error in the sound-speed correction of the measurements translates into a larger array element rms error, but does not substantially affect the estimated position due to the nearly equilateral triangle system configuration. Due to possible inaccuracies in the absolute XBT measurements, and the robust nature of the system configuration to errors in sound speed, the profile was considered constant over time and equal to the CTD calculations. The fourth column in Table I incorporates refraction effects due to changes in the sound-speed profile $C(z)$ described above. The predictions generated by the GSM indicate that, for the geometrical configuration of the September experiment shown in Fig. 4, the error in travel time by assuming a straight-line path with a constant average sound speed is 0.1 ms; therefore, using the harmonic mean of the sound-speed profile introduces a negligible error (0.15 m) in the array positions.

GPS satellite positions at FLIP and the surface ship during transponder deployment provided the initial estimates of the transponder xy positions to within tens of meters. The element weather that prevailed during the deployment and the negative buoyancy of the transponders (sink rate of ≈ 1 m/s) constrained the final transponder positions. Initial

transponder depths were estimated by subtracting the transponder anchor line length from the echo-sounding depth measured at FLIP. The assumption that the seafloor is flat in the immediate area of FLIP was corroborated by bottom-mounted Swallow floats deployed approximately 2 nmi from FLIP. Preliminary Swallow float depth estimates were within 15 m of the depth measured at FLIP.[14]

Once the ingredients for the least-squares method have been accumulated, the *xy* positions are adjusted until the root-mean-squared (rms) error satisfies the convergence criteria described below. This is accomplished in several steps by first maintaining constant transponder positions and perturbing the FLIP positions to minimize errors, then holding the current FLIP positions constant while perturbing the transponder positions to minimize errors, then examining the mean-squared error of each FLIP position to determine (via a user parameter) whether it should be preserved as usable contributor, and, finally, repeating the entire procedure until the convergence criteria are satisfied. The perturbation adjustment is calculated with the search direction **p** defined as the negative gradient. The step size is a constant (1.5 m) unless the rms error is less than 1 m, at which time the step size begins to decrease, as the minimum is approached, the step size is recalculated as a function of the percent change in iterated rms error. The convergence criteria are defined as follows: an absolute rms error less than 0.15 m, a 0.15% change in the iterated rms error, or a maximum of 30 iterations. A typical number of loop iterations required for the convergence of the September data set were 3 for each inner loop and 5 for the entire procedure, the repetition factor depending on the user parameters. A detailed description of the software implementation and its usage is documented.[4]

The transponder depths were iterated manually by minimizing the magnitude and dispersion of rms error across the array. Increasing rms errors across the array was shown by the simulations in the following section to be an indication of potential transponder depth error. The FLIP database used to navigate the transponders was sampled during tidal peaks to discern whether there was any transponder movement due to tidal forces. No appreciable difference was observed, and transponder movement is assumed to be negligible.

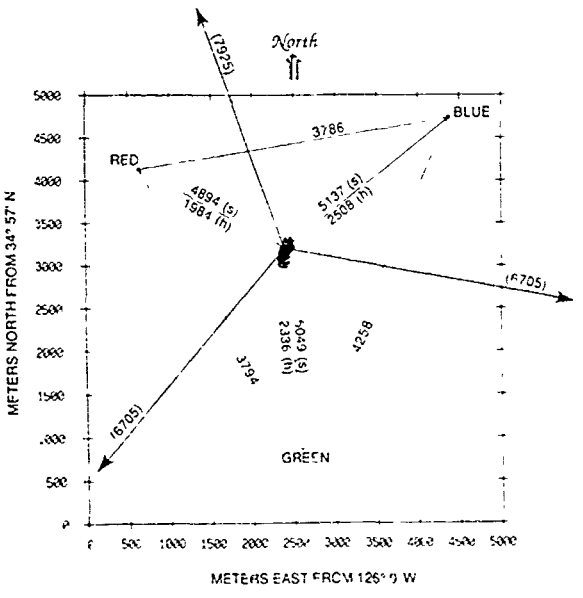

FIG. 4. Spatial configuration for navigation during the September 1987 sea test. The estimated positions of FLIP and the three bottom transponders (red, green, and blue, measured hourly over 18 days) are shown in plan view. The FLIP mooring lines are represented by arrows, and the slant range (*s*) and horizontal projection of the slant range (*h*) are indicated in meters from an arbitrary FLIP *xy* position (2400, 3200). Transponder baseline distances are indicated in meters.

2. FLIP and array element localization

The localization procedure for FLIP and the array is essentially the same as just described for the transponders. With the transponder positions known, the FLIP and array element navigation may be calculated in real time.

The initial *xy* positions for FLIP and the array elements were estimated from GPS positions after FLIP was moored (Julian day 255). Because FLIP's position was maintained by a three-point moor, the same initial *xy* position was used for each FLIP position throughout the test. If the initial *xy* position must be estimated without GPS, or if the receiver is not moored, a geometric estimate may be obtained from the transponder slant ranges. The depths of the array elements were measured to within 1.5 m by the 12-kHz transmitter mounted on the bottom of FLIP. The 12-kHz signal was received by each navigation receiver without exception, however, there were indications of slight interference in the variability of the arrival time of the resulting correlated output. The array was deployed under 420 kg of tension to maintain verticality and constrain the depth parameter. A 1.5-m error in array depth, because this input is a fixed parameter in an equilateral configuration, translates into less than 0.5 m of error in the *xy* positions of the array, but changes the rms error by as much as 2.5 m.

The noise in the travel times measured at the array is greater than the noise in the hand-picked data measured at FLIP. To improve the data quality, various averaging, thresholding, and interpolation schemes were incorporated in the processing software. Should a receiver not detect a return, or if the detected return is not within specified thresholds for range and depth variability, various interpolation/extrapolation software options may be specified. Prior to the least-squares iterations, the data may be smoothed with a running average filter. The travel time measured at the array represents the time from FLIP to the transponder to the array. Therefore, to acquire the transponder-to-array travel time required by the least-squares procedure, the FLIP-to-transponder travel time (measured at FLIP once an hour) is interpolated and subtracted from the travel time measured at the array (approximately once per minute).

C. Simulations

Simulations were conducted to examine the array position sensitivity to errors in the transponder and FLIP positions. The spatial configuration shown in Fig. 4 simulates the September sea test; FLIP is centrally located in the transponder network (identified by colors), and the array is di-

rectly under FLIP. The transponders, FLIP, and the array are initially assigned to known positions with slant ranges as shown. Individual transponder positions were perturbed, and the resulting array shape and relative errors were examined. These tests were conducted first with the array in a vertical orientation; that is, the array element xy positions were identical to those of FLIP, and then with the array straight but tilted 2° vertically at 225° azimuth. Zero mean Gaussian random errors ($\sigma^2 = 3$ m) were added to the array travel times with no appreciable changes. The final simulation configuration perturbed the FLIP position. Because the array measures travel times of rays which originate at FLIP, errors in the FLIP parameters map into array positional errors.

The simulations provide an understanding not only of the error magnitudes but also of their dispersion across the array. With a + 25-m perturbation in the x or y transponder positions, the effect on the initially vertical array is a horizontal translation in the direction of the transponder with no relative array positional errors. If an error is introduced in the z transponder position, the array is translated and tilted. Figure 5(a) shows the effect on the array as the blue transponder is perturbed by 100-m errors individually in x, y, and z, and finally simultaneous 100-m errors in x, y, and z. Figure 5(b) shows the effect of transponder depth errors. Each transponder depth was increased and decreased individually by 10 and 25 m. The dot in the center of the figure is the navigated FLIP and array positions with no input errors; with a decrease in transponder depth, the input slant range appears to be too long, and the array is translated in a direction away from the transponder (notated by O's on the plot) and tilted slightly. An increase in transponder depth operates similarly except in a direction toward the transponder (notated by ×'s on the plot). The results of the simulations for the positive perturbations with an initially straight vertical array are compiled in Table II. The columns indicate which parameter has been perturbed and the amount of the perturbation, the translation and percent change in range calculated for the FLIP position, system tilt, and position rms [$\sqrt{F}$ in Eq. (1)]. The rms error is shown as a single number if the difference in error across the array was less than 0.1 m; when two numbers are shown, they indicate the error at FLIP and the bottom element of the array. By examining the FLIP translation and rms error for the x and y perturbations in Table II, it is clear that the x position is controlled by the red and blue transponders, and the y position is controlled by the green and blue transponders (Fig. 4). The difference in rms error between the three transponders reflects the percent deviation from original slant range. The dispersion in rms error was used to iterate the transponder depth. This can be seen, for example, in the results of the red depth perturbation which yields an rms error at FLIP of 18.13 m, monotonically decreasing to 13.48 m at the bottom of the array. The array and FLIP positions are more sensitive to errors in transponder depth (60%–70% of perturbation) than to errors in transponder horizontal (xy) position (< 35% of perturbation). To demonstrate this sensitivity dichotomy, with FLIP at a known position x,y from a transponder, the FLIP translation T_z due to an error δ_z in transponder depth, and the translation T_{xy} due to errors δ_x and δ_y in transponder xy position are

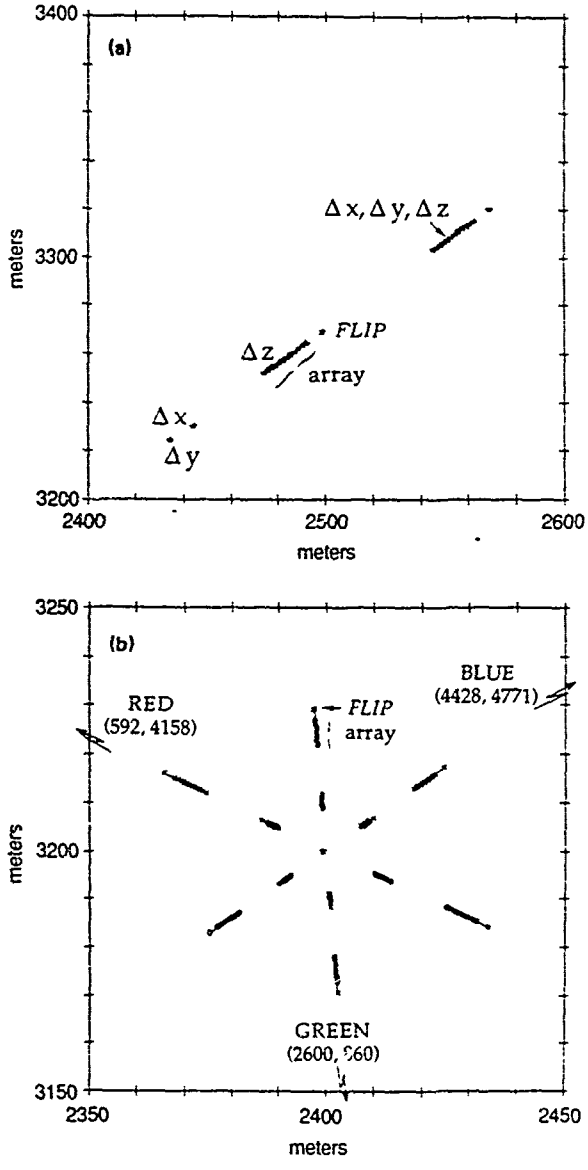

FIG. 5. Error simulation results. The effect of errors in the transponder positions on the shape and position of FLIP and the array are shown in plan view. (a) Effect on the FLIP and the array as the blue transponder is perturbed in x, y, and z. (b) FLIP and array positions as a function of transponder depth error.

$$T_z = h - s\sin\{\cos^{-1}[(d+\delta_z)/s]\}, \tag{9}$$

$$T_{xy} = h - [(x-\delta x)^2 + (y-\delta y)^2]^{1/2}, \tag{10}$$

where h and s are the horizontal and slant ranges, respectively (Fig. 4), d is the difference in depth between the base of FLIP and the transponder, x is the component of h in the $\hat{x}$ direction, and y is the component of h in the $\hat{y}$ direction. FLIP is constrained by the experimental configuration to move approximately along the line defined by the horizontal projection of the slant range between the perturbed transponder position and FLIP (Fig. 5). To quantify these translational errors, a δ_z of + 25 m in the red transponder depth

TABLE II Navigation error simulations

Perturbation (m)	% change in slant range	% change in horizontal range projection	Array tilt (deg)	Translation from initial position (m)	rms error (m)	% of original perturbation
		FLIP and array position with errors in transponder positions				
Red $X + 25$	0.1323	0.7780	0.000	15.802	7 11	28.4
Green	− 0 0693	− 0.3095				
Blue	− 0 0724	− 0 2940				
Red	0 0110	0 0640	0.000	1 498	0.78	3 1
Green $X + 25$	− 0.0124	− 0 0550				
Blue	0 0012	0 0049				
Red	0 0576	0 3333	0 000	14.161	6 45	25.8
Green	0.0636	0 2832				
Blue $X + 25$	− 0 1360	− 0.5463				
Red $Y + 25$	− 0 0638	− 0.3663	0.000	7.540	3.83	15 3
Green	0.0383	0 1708				
Blue	0.0296	0 1198				
Red	− 0.0669	− 0.3880	0.000	15 849	8.73	34.9
Green $Y + 25$	0.1468	0.6636				
Blue	− 0.0879	− 0.3567				
Red	0.0454	0.2627	0.000	11 149	5.01	20.0
Green	0 0499	0.2223				
Blue $Y + 25$	− 0 1069	− 0 4304				
Red $Z + 25$	− 0 3083	− 1.8163	0.482	37.199	18.13, 13.48	72 5, 53 9
Green	0 1778	0 7907				
Blue	0 1624	0.6567				
Red	0.1405	0 8112	0 375	29.320	16.63, 12.39	66.5, 49.6
Green $Z + 25$	− 0.2689	− 1.2156				
Blue	0 1489	0 6022				
Red	0 1225	0.7076	0 382	30 631	14.46, 10.76	57.8, 43 0
Green	0 1419	0.6311				
Blue $Z + 25$	− 0 2901	− 1 1915				
		FLIP and array positions with errors in FLIP slant ranges				
Red + 25	0 3561	2 0453	0.424	41.936	19 04, 15 73	76 2, 62.9
Green	− 0.1865	− 0 8346				
Blue	− 0.1855	− 0.7543				
Red	− 0.1454	− 0.8450	0.315	33.396	18.28, 15.20	73.1, 60.8
Green + 25	0.3122	1.3848				
Blue	− 0.1780	− 0.7236				
Red	− 0 1279	− 0 7432	0 315	34.034	16 08, 13.51	64.3, 54.0
Green	− 0 1577	− 0 7054				
Blue + 25	0.3284	1 3250				

of Eq. (9) resulted in a 58-m FLIP xy position translation, and a δ_x of + 25 m in the red transponder x position of Eq. (10) resulted in a FLIP xy position translation of only 22 m, illustrating that FLIP position is more sensitive to errors in transponder depth than to errors in transponder xy position.

An error in transponder position, when the array is tilted, will distort the vertical and azimuthal array orientation as well as impart a horizontal translation. A tilted array will show a horizontal translation comparable to the initially straight array, but with azimuthal and vertical rotations. The vertical angular change is similar to that of the straight array for depth perturbations and small but noticeable for horizontal perturbations. The azimuthal angular change is larger for both horizontal perturbations (0.3° tilt) and depth perturbations (14° tilt).

An error in a FLIP slant range also translates into an array positional error. An error which increases the slant range moves FLIP away from the transponder and the array closer. It also induces a tilt in the array making the bottom closer to the no-error position than the top, with a corresponding decrease in rms error from the top to bottom of the array. Table II shows the results of the simulation for + 25-

m errors in the three transponder slant ranges to FLIP. A transponder slant range error δ_s before iteration creates a translation error:

$$T_s = h - \sqrt{h^2 - 2\delta_s s - \delta_s^2}, \tag{11}$$

where h and s are defined above. An error δ_s of $+25$ m in the red transponder slant range of Eq. (11) yields a translation error T_s of 62.3 m prior to iteration.

These simulations quantify the mapping of errors in slant ranges to errors in xy positions. The adjustment direction is dictated by the measurement direction (horizontal range direction) not the model parameters (xy directions) or the error direction. The positions of FLIP and the array are more sensitive to errors in transponder depth and FLIP slant range than to errors in transponder horizontal position. This sensitivity is attributed to the constraint of fixed array depth (negligible measurement errors) necessitating an assignment of the error to the horizontal projection. These errors are magnified and dispersed across the array. It was this dispersion that was used as a criteria for convergence during the transponder depth iteration.

III. DATA ANALYSIS

The motions of FLIP and the array are analyzed to determine the navigation accuracy, the extent of movement, and possible forcing functions driving the system. The data consisted of the GPS satellite positions acquired at FLIP, estimated FLIP positions spanning a period of 18 days with 1-h samples, and estimated array element positions at a nominal depth of 850 m spanning a 24-h period. The GPS positions acquired aboard FLIP provide an independent verification of the estimated FLIP positions derived using the least-squares method (Fig. 6). The GPS positions in latitude and longitude were converted to meters from the least-squares origin by calculating the local radius of the earth as follows[15]:

$$x_{\mathrm{GPS}} = r_{\mathrm{pos}}\,\delta(\mathrm{lat}), \quad y_{\mathrm{GPS}} = r_{\mathrm{pos}}\cos(\mathrm{lat})\,\delta(\mathrm{long}), \tag{12}$$

where

$$r_{\mathrm{pos}} = r_{\mathrm{eq}}\,[1 - f\sin^2(\mathrm{lat})], \qquad f = \frac{r_{\mathrm{eq}} - r_{\mathrm{polar}}}{r_{\mathrm{eq}}}$$

and where x_{GPS} is the E–W distance, y_{GPS} is the N–S distance, r_{pos} is the earth's radius at the position latitude, $\delta(\mathrm{lat})$ is the difference in latitude between the position and the origin, $\delta(\mathrm{long})$ is the difference in longitude, lat is the latitude of the position, r_{eq} is the earth's equatorial radius, and r_{polar} is the earth's polar radius. The observed 10-m rms deviation between the GPS and navigated FLIP positions is reassuring. FLIP positional errors are independent and distributed normally at a χ^2 0.05 level of significance with zero mean and a standard deviation of 1.1 m. Array positional errors may deviate from a normal distribution, depending on the nature of the transponder and receiver errors; however, considering a receiver with low errors, a Gaussian distribution of 2.9-m mean and 0.81-m standard deviation may be compared at a 0.05 level of significance. Receiver detection threshold mismatch, tuned filter drift, sound-speed errors,

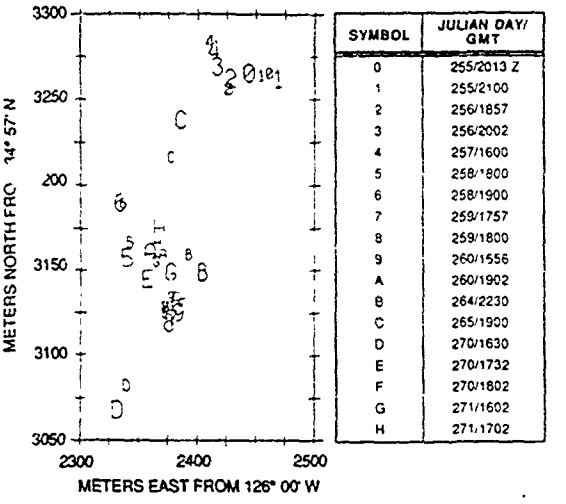

FIG 6. Comparison of GPS satellite and acoustic navigation FLIP GPS positions are compared to those estimated by the least-squares navigation. The large symbols represent the GPS positions, while the corresponding small symbols represent the estimated FLIP positions. A bias correction, attributed to drift of the transponders during deployment, of 24 5 m was added to the N–S estimated positions and 1 2 m to the E–W estimated positions.

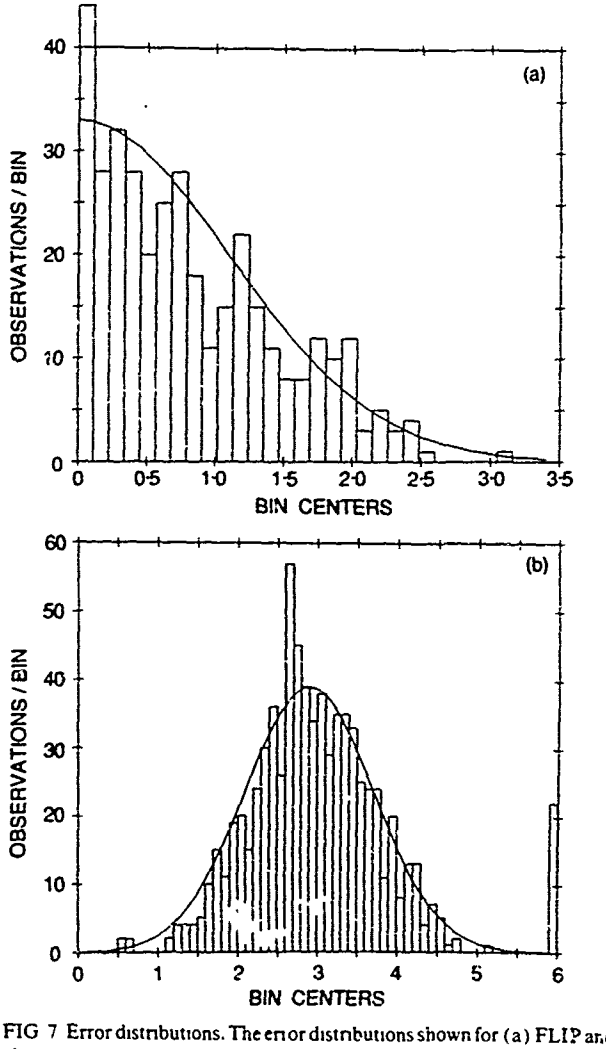

FIG 7 Error distributions. The error distributions shown for (a) FLIP and (b) array navigation receiver No 8 are independent as illustrated by a runs test and Gaussian at a 0.05 level of significance The high transponder errors shown in the 6-m bin of (b) are due to transponder detection of multipath propagation

the FLIP position, as described earlier, contribute to the mean. FLIP and array error distributions are shown in Fig. 7.

The motion of FLIP (Fig. 8) is primarily controlled by the local wind field, the tides, and the tension on the mooring lines. The low-frequency movement of FLIP is driven by the local wind, primarily from the north during the entire experiment. The wind speed has a high negative correlation with FLIP N–S positions and, to a lesser extent, with FLIP E–W positions. This is expected as a northerly wind would tend to push FLIP toward the south. At 35° N latitude the tidal cycle is semidiurnal and appears as a prominent component in the FLIP time series. The tidal component in the E–W displacement lags 2 h behind the N–S component, producing a clockwise rotation. This rotation is also seen in the calculated tidal velocity ellipse (Fig. 9), which lags the displacement by 90°. The tidal velocity ellipse, which includes contributions from both the barotropic and baroclinic modes, is comparable to simultaneous estimates of the current field recorded by current meters deployed at 50 and 100 m below the water surface from FLIP. Although the current meter measurements are relative to FLIP, the tidal component is four times as strong as the constrained FLIP component and leads in phase due to FLIP's massive structure and mooring line effects.

The motion of the array (Fig. 10) is controlled by the tides, the motion of FLIP, and possibly by internal waves or higher frequency surface motion that is unresolved in the FLIP data set. The longest period movement of the array was on the order of days and was driven by FLIP's response to the wind. This is inferred by the fact that the top array position was normally within a 30-m horizontal slant range of FLIP which traveled over 300 m during the 18 days (within 20 m in Fig. 11). The tidal cycle is evident as a 12-h oscillation in the 24-h time series and as the 0.083-cycles/h peak in the spectrum (Fig. 12).

Higher frequency array oscillations appear in the expanded time series in Fig. 10(c) and (d), but are not stationary over the 24 h, and all but disappear from the spectrum during the averaging process. Although the sample-to-sample motion of the array is on the same order as the errors, the errors are independent and Gaussian, therefore, we believe the fluctuations which occur with periods from 15 or 20 min to 2 h are due to array motion. Modeling the array as a simple pendulum where the center of mass is derived from four component parts (uplink wire, array, kevlar, and weights), the natural period of oscillation is just over 1 min. The damped natural period for a velocity of 5 cm/s is 7 min with a damping coefficient of slightly less than critical. These periods do not coincide with the 0.3–2-h periods seen in the array data, therefore, the high-frequency motions must be due to environmental forcing functions. We believe it to be a combination of two processes, the coupling of the array to the surface and the array response to low-order modes of the internal wave field. The motion whose periods are from tens of minutes to many hours (Vaisala frequency in the N Pacific is about 20 min near the surface) and whose horizontal velocities of 1–2 cm/s are reasonable for a constrained internal wave response[16] where typically horizontal currents are about 5 cm/s and horizontal current spectra is

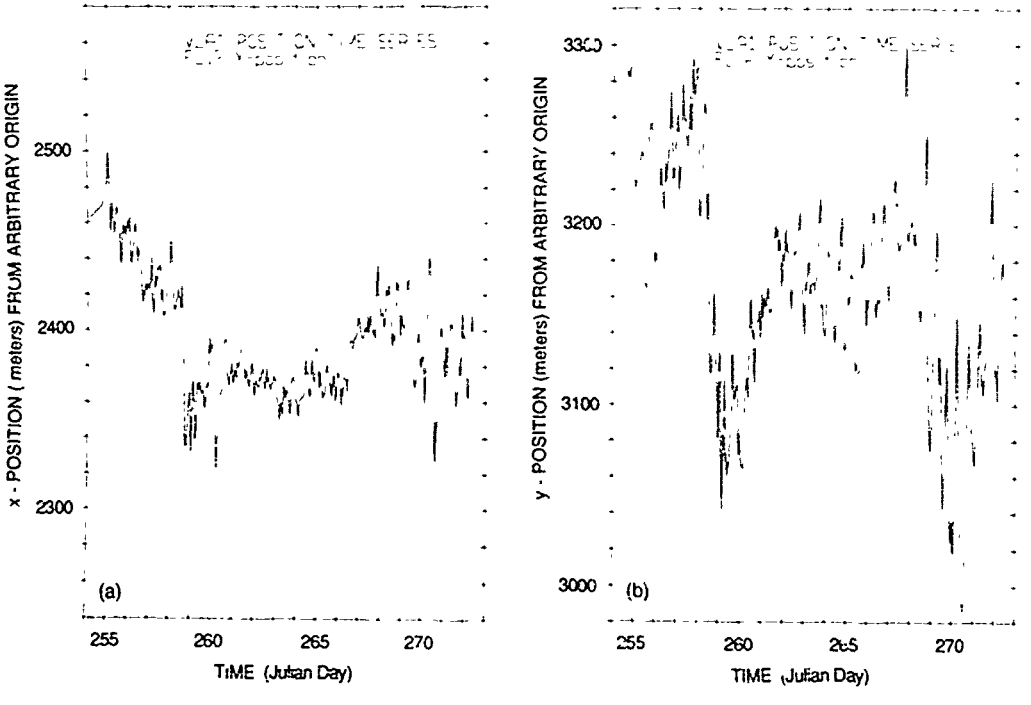

FIG. 8. FLIP position time series. The FLIP positions are estimated approximately every hour and plotted over the 18-day experiment. The (a) x positions, increasing toward the east, and the (b) y positions, increasing toward the north, are plotted on the same relative vertical scale, but with different origin

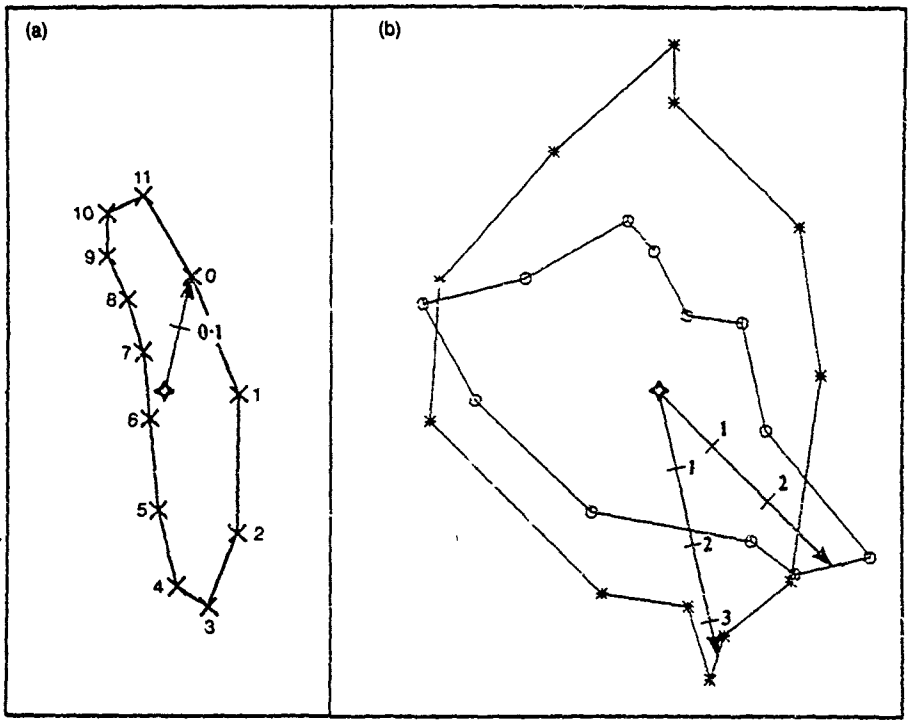

FIG. 9 Tidal current ellipse (a) The current ellipse estimated from FLIP positions was calculated by finite differencing the 18-day time series, low-pass filtering the resulting hourly estimates, and then averaging 12-h segments The tips of the current vectors were plotted from a common origin every hour. The 0 GMT vector is marked in cm/s. (b) Current meter data collected from FLIP represent 12-h segment averages (O) over 13 days at 43 m and (*) over 20 days at 90 m. Mean velocities of 7.5 cm/s E, 0.64 cm/s N at the 43-m site, and 7.2 cm/s E, −0.91 cm/s N at the 90-m site were removed.

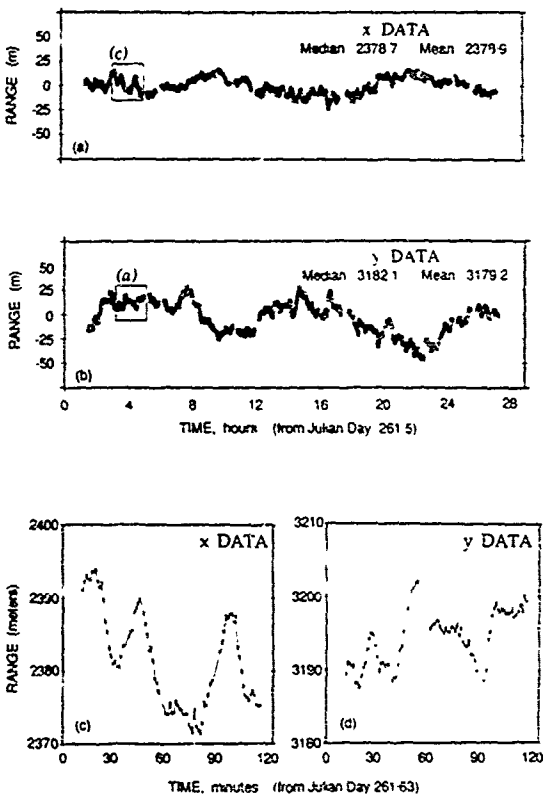

FIG. 10. Array position time series. The estimated positions for the array section 8 navigation receiver are plotted relative to the median value. In (a) range increases toward the E, and in (b) toward the N The area identified by a box in (a) and (b) is expanded in (c) and (d) to illustrate this high-frequency motion.

dominated by the lower-order modes.[17] The motion spectrum does not show a peak at the local inertial frequency,[18] nor an ω^{-2} energy dependency between the inertial frequency (0.048 cycles/h) and the Väisälä frequency common in internal wave energy spectra.[19] This characteristic shape is apparently filled in by the coupled response to surface-generated motions.

The array shape during the experiment is modeled to first order as linear, but slightly tilted from vertical. The array shape plotted approximately every 3 min over the first hour of data shown in Fig. 10(c) and (d) is illustrated in Fig. 11, where the horizontal deformation has been exaggerated for clarity, extending 50 m in the horizontal compared to 1600 m in the vertical. These data show a linear array with receiver position deformations within the rms error estimated by the least-squares procedure[4]; and with a deviation of less than 5 m across the array aperture, the array maintains a vertical orientation to within 0.5°. Array shape snapshots every 5 h over a longer period of time (20 h) show that the array follows FLIP to within a 30-m horizontal range (Fig. 13). The change in array depth due to such a 30-m deviation, assuming a linear cable, is only 1 m, which is not significant. The array tilt from vertical is within about 1°, considering the maximum deviation (15 m) shown across the aperture. The linear pendulumlike response is particularly apparent in the 2-min snapshots as the array responds to the motion of FLIP and the internal wave field. Although the time sequence of the individual estimates is not legible, the crossing uplink lines indicate small-scale array oscillations, through which the linear shape is maintained. It is evident that the array exhibits a more active response (presumably due to

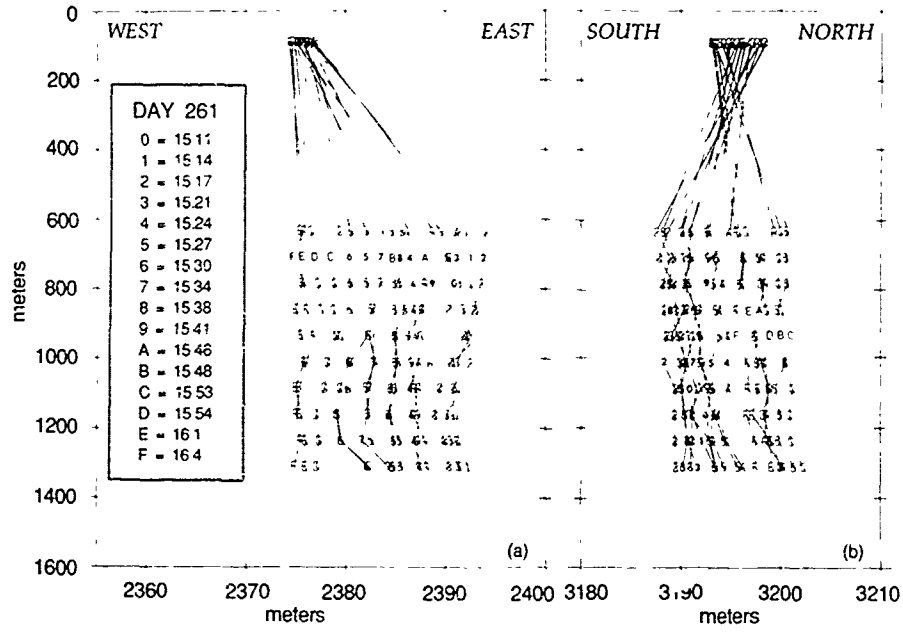

FIG 11 Array shape over 1 h The positions of the ten deepest navigation receivers are shown over a 1-h period The top two receiver positions were deleted due to their large errors (Ref 4) The two views are (a) East–West versus depth, and (b) North–South versus depth The snapshots are spaced at approximate 3-min intervals and represent a subset of the data shown in Fig 10(c) and (d)

internal waves) than FLIP by examining the extent of FLIP motion compared to that of the array during the same time period. The array moves over four times the E–W distance covered by FLIP during the hour plotted in Fig 11

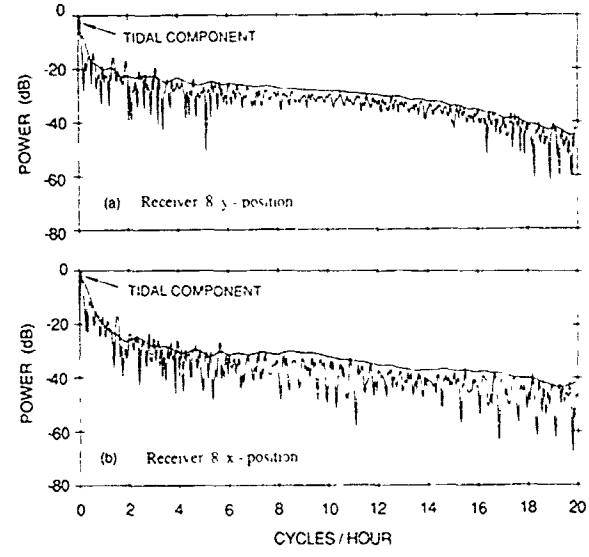

FIG 12 Spectrum of array motion For receiver (a) x position and (b) y position, the smooth curve is an averaged 1024-pt spectrum of 15, 50% overlapped, Kaiser–Bessel windowed ($\alpha = 2.5$) 128-point time series plotted on a relative scale A single spectrum was computed similarly over the entire time series and plotted on the same relative scale with 0 039-cycles/h resolution for more accurate identification of the narrow-band spectral components

IV. CONCLUSION

The least-squares method was implemented to convert measured travel time data to spatial positions for FLIP and a 900-m vertical array by assuming a harmonic sound speed and normally distributed errors. Navigated FLIP positions (mean = 0.5 m, $\sigma = 1.1$ m) agree with positions obtained from GPS satellite navigation to within an rms error of 10 m. A mean error as small as 2.8 m with a standard deviation of 0.8 m was obtained for array element position; however, each receiver displayed a unique error distribution due to variations in the array detectors. Array positions were found to be particularly sensitive to errors in FLIP position and transponder depth. This was demonstrated by simulation to be a result of the optimization constraints. Iteration of array depths and incorporation of a more accurate sound-speed correction has shown promising preliminary results by reducing the mean rms array element error to less than 1 m, while leaving the estimated positions within 0.2 m of the positions presented here. The navigated positions are tied to an absolute frame of reference using transponder GPS locations, and the absolute positions are substantiated by the GPS positions at FLIP and the high negative correlation between FLIP's N–S component and the wind speed. FLIP's position was driven by the winds and tides, but was constrained to approximately a 300-m range by a three-point mooring The array position was driven by tidal motions at a semidiurnal period, and apparently by internal waves and coupled surface-wave motion at higher frequencies. Array high-frequency motions were up to a factor of 4 larger than FLIP motions, although the array normally maintained a vertical orientation to within a tilt angle of 2° and remained within a 30-m range of FLIP.

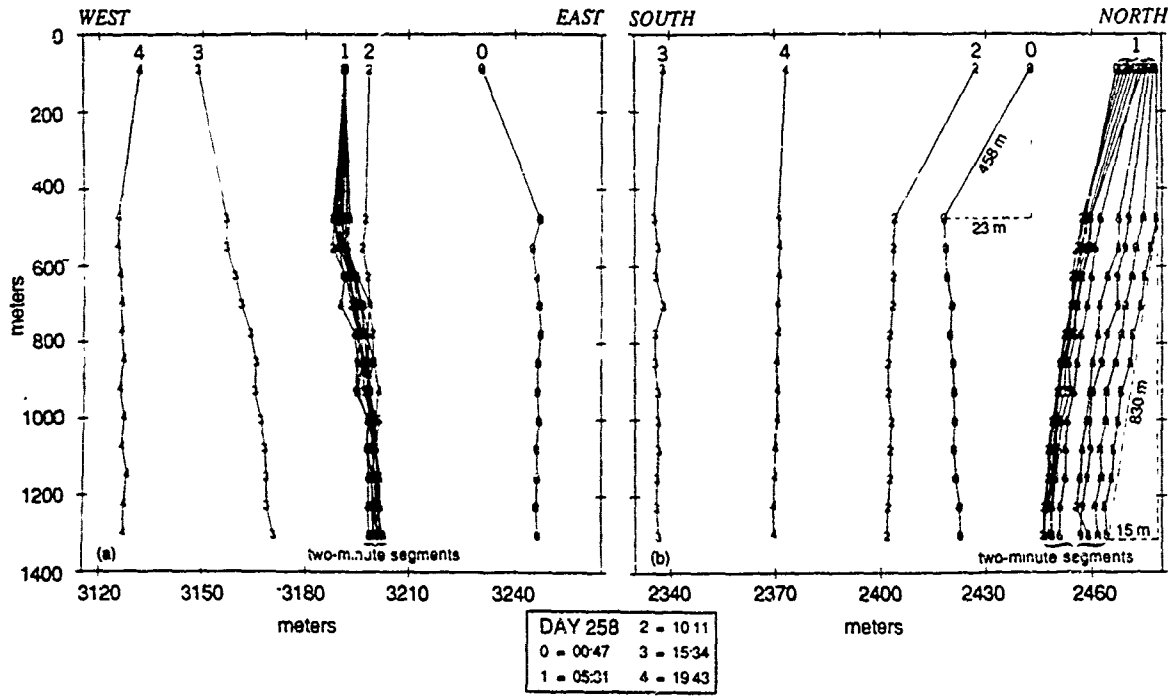

FIG. 13 Array shape over 20 h. The positions of the 12 navigation receivers are shown at 5-h intervals over a 20-h period The two views are (a) East–West versus depth and (b) North–South versus depth. Snapshots every 2 min are shown beginning at 5:31 GMT over a 24-min period.

ACKNOWLEDGMENTS

The authors are indebted to C. de Moustier for his review of the manuscript and W. Hodgkiss, S. Flatte, K. Watson, and G. D'Spain for their valuable suggestions. We thank F V Pavlicek for engineering expertise, E. Wolin, P. Henkart, R. Curner, C. Lowenstein, and R. Lawhead for software support, A. Aja, D. Ensberg, and P. Scott for their assistance in data processing, and J. Griffith for her illustrative talents. The captain and crew of the research platform FLIP contributed to the sea-going operation. This work was supported by the Office of Naval Research under Contract N00014-87-K-0225 and N00014-87-C-0127.

[1]B. J. Sotirin and J A Hildebrand, "Large aperture digital acoustic array," IEEE J. Ocean. Eng. OE-13, 271–281 (1988).

[2]F. N. Spiess, "Panel on Ocean Bottom Positioning and National Research Council Committee on Geodesy," in *Seafloor Referenced Positioning: Needs and Opportunities* (National Academy, Washington, DC, 1983), p 15.

[3]D E. Boegeman, private communication (1988).

[4]B. J. Sotirin and W S. Hodgkiss, "Navigation software for the MPL vertical line array," MPL TM-409, Marine Physical Laboratory, Scripps Institution of Oceanography, University of California, San Diego, CA (March 1989).

[5]P. E. Gill, W. Murray, and M. H. Wright, *Practical Optimization* (Academic, Orlando, Fl, 1981), p 100

[6]G L. Duckworth, "A robust algorithm for tracking of drifting acoustic arrays in the arctic," Signals, Systems and Computers, 21st ASILOMAR Conference Proceedings, Pacific Grove, CA (2–4 Nov. 1987).

[7]H. W Sorenson, *Parameter Estimation—Principles and Problems* (Dekker, New York, 1980), pp. 45, 225

[8]F. N. Spiess, "Analysis of possible sea floor strain measurement system," Mar Geod. 9 (4), 385–398 (1985)

[9]W Smith, W. M. Marquet, and M. M Hunt, "Navigation transponder survey: design and analysis," in *Oceans 75 Record* (IEEE, San Diego, CA, Sept. 1975), pp. 563–567

[10]H Weinberg, "Generic sonar model," NUSC TD-5971D, Naval Underwater Systems Center, New London, CT (1985)

[11]J. Churgin and S. J. Halminski, "Temperature, salinity, oxygen and phosphate in waters off the United States, Eastern North Pacific," National Oceanographic Data Center, Washington, DC (1974), Vol 3

[12]N. P. Fofonoff and R. C. Millard Jr., "Algorithms for computation of fundamental properties of seawater," Technical Paper 44, Unesco Division of Marine Sciences, Paris, France (1983).

[13]C. S. Clay and H. Medwin, *Acoustical Oceanography Principles and Applications* (Wiley Interscience, New York, 1977), p. 3.

[14]W. S. Hodgkiss and G. L. D'Spain, private communication, (1988)

[15]R. A. Stacey, *Physics of the Earth* (Wiley, New York, 1976), p. 74

[16]C. Garrett and W. Munk, "Internal waves in the ocean," in Annu. Rev Fluid Mech. (Annual Reviews Inc., 1979), 339–369

[17]R. Pinkel, private communication (1989)

[18]W. Munk, "Internal waves and small-scale processes," in *Evolution of Physical Oceanography* (MIT, Cambridge, MA, 1981), pp 264–291.

[19]J-H Hu and P P. Niiler, "NEPAC current meter and XBT data for circulation in NE Pacific thermocline," SIO Ref. No 87-4, Scripps Institution of Oceanography, University of California, San Diego, CA (Feb. 1987).

J-OE/13/4//24726

Flip II

Frederick H. Fisher

Reprinted from
IEEE JOURNAL OF OCEANIC ENGINEERING
Vol. 13, No. 4, October 1988

FLIP II

FREDERICK H. FISHER, SENIOR MEMBER, IEEE

(*Invited Paper*)

Abstract—After 26 years of operations at sea with the Research Platform FLIP, a 355-ft-long craft which has a draft of 300 ft in the vertical position, planning is underway for a larger, more capable FLIP II that can operate in seas with waves of up to 80 ft and survive more severe seas. As our research in acoustics extends to studies of ambient noise and propagation at lower frequencies, recent deployments of large aperture (900 m), multi-element (120) arrays tax the space and facilities on FLIP. Future plans include deployment of 240 element, 3500 m arrays as well as large, powerful sound sources that further tax the limits of current capabilities.

The original FLIP, while designed to work in 30-ft waves with no more than a 18 percent heave response, has survived 80-ft swells (22 s period) with only minor damage. Research requirements for greater laboratory and deployment capabilities to make possible joint multi-disciplinary/group operations and the need to work in regions with worse weather cannot be met with the current FLIP nor is it economically or structurally feasible to modify it to do so. Along with a brief description of FLIP, this paper lists the variety of research conducted from FLIP in both the Pacific and Atlantic Oceans and whether it was in drifting or moored deployments in deep water. While originally built for acoustic research, it has also been used for physical oceanography, meteorological, and biological studies. A recent workshop on research platforms highlighted the needs of several different scientific communities for a larger, more capable FLIP-type vessel with a minimal air and water column profile that can work in severe weather.

The purpose of this paper is to invite the interest and attention of the scientific and engineering communities regarding the design and potential uses of a larger FLIP II. Current thinking centers around 420-ft-long, 30-ft-diameter hull with a smaller water plane diameter of 20 ft. All weather deployment capability of submersibles from the bottom of FLIP II (draft 340 ft) is considered. Preliminary design efforts have been initiated with a naval architect.

I. Introduction

AFTER 26 years of operations, the U.S. Navy's deep draft (300 ft) Research Platform FLIP (FLoating Instrument Platform) [1] shown in Fig. 1 is continuing to provide a unique stable platform from which to conduct research at sea without suffering the violent motions that accompany storms and rough weather. In fact, because of the deep draft and long heave period of 27 s, those working on FLIP during the sea-state six conditions can enjoy charcoal broiling outdoors. The stability minimizes adverse effects on deployed instrumentation as well as fatigue for those personnel on board. It also makes possible experimental research that can be done in no other way.

Manuscript received July 15, 1988; revised September 26, 1988. This work was supported by the Office of Naval Research under Contracts N00014-80-C-0220 and N00014-87-C-0127.

The author is with the Marine Physical Laboratory, Scripps Institution of Oceanography, University of California, San Diego, San Diego, CA 92152.

IEEE Log Number 8824726.

The 355-ft-long spar buoy, designed by the Marine Physical Laboratory (MPL) of the Scripps Institution of Oceanography for acoustic research [1], [2], has been operating for 26 years since it was launched June 22, 1962, at the Gunderson Brothers Engineering Company in Portland, Oregon. The low heave response (max. 18 percent at 17 s) in heavy weather and its low tilt fluctuations [2] more than met the stability requirements for the immediate acoustic research objectives. In addition, the design was intended to make FLIP a platform that would be useful for other types of research and that, in fact, has been the case (as seen in Table I).

The unique characteristics of a FLIP-type platform (stability, low profile in water and air column, ease of mooring in deep ocean) have attracted the attention of scientists in several different disciplines who are interested in a larger, more capable FLIP II. Physical oceanographers, meteorologists, biologists, and marine physicists studying acoustic propagation and ambient noise in the ocean participated in the Platform Workshop held at the MPL on June 29–30, 1988. Their specific needs were spelled out in considerable detail regarding requirements for a larger FLIP. The workshop was instigated by recent requests to participate in research in more northernly waters and by the need to carry increasingly larger scientific parties with correspondingly larger amounts of equipment.

For example, at MPL we have been studying ambient noise and acoustic propagation in the ocean over the last two decades, making use of vertical arrays of hydrophones deployed from FLIP in three-point moors, most recently with a 900 m, 120-element array, as shown in Fig. 2. For studying low-frequency ambient noise and propagation we need to use large hydrophone arrays to provide the resolution to separate multipaths and to study the differences between local and long distance sources of ambient noise, man-made or natural. The three-point mooring assures a minimal flow noise around hydrophones and a maximum verticality of the arrays. In order to pursue these studies in regions which are more subjected to storms, and with larger and larger arrays to study lower frequencies, we find a recurring need for a larger, more capable replacement for FLIP.

A second major area of research at MPL which utilizes FLIP has been the study of internal wave propagation in the upper ocean. This work was initially performed using both fixed and vertically profiling temperature sensors. These were mounted on horizontal booms rigged from FLIP to provide a 30 m horizontal array. The profiling system obtained data from the surface down to 400 m on a 2-min-cycle time. The

0364-9059/88/1000-0174$01.00 © 1988 IEEE

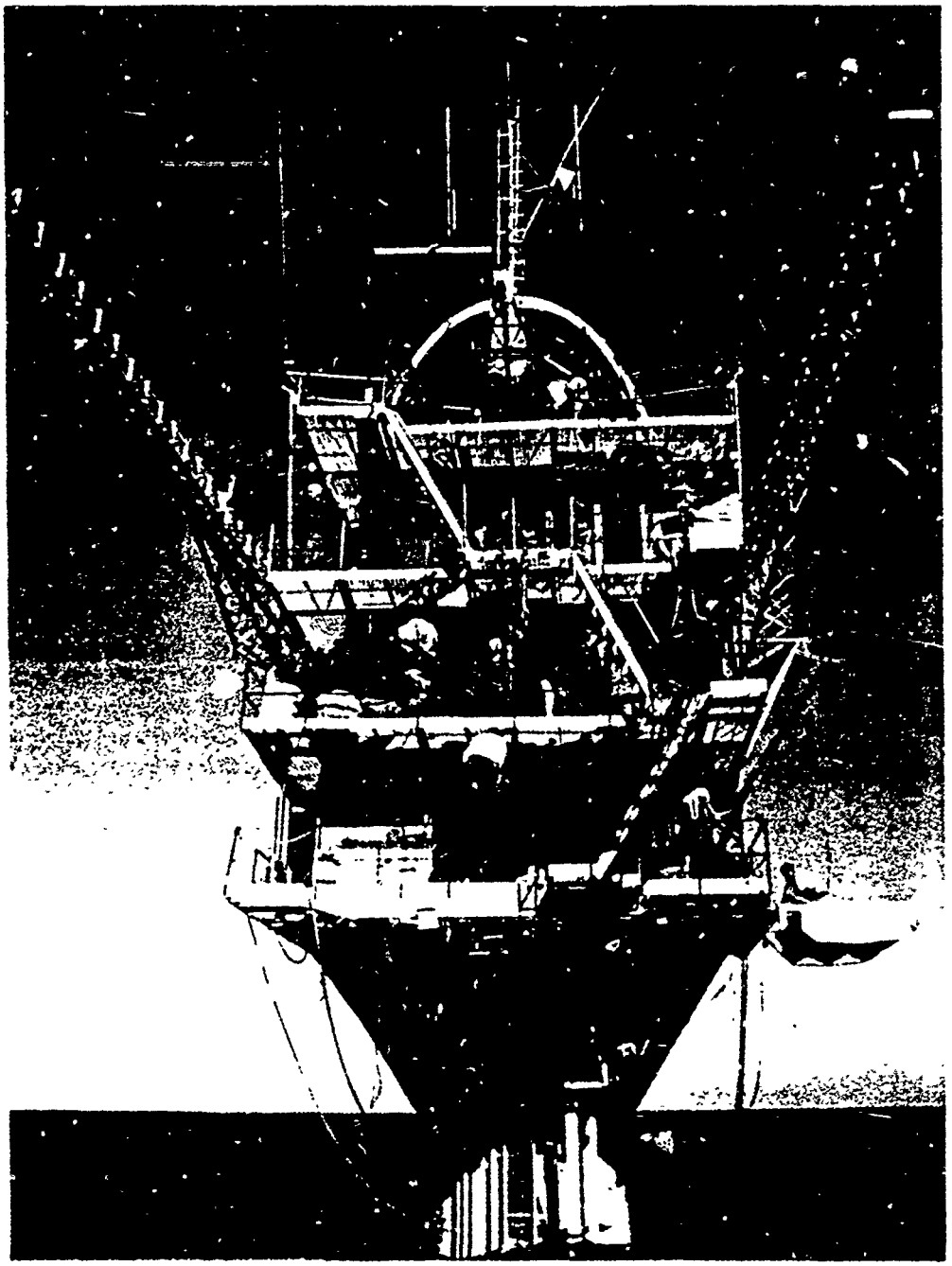

Fig. 1. FLIP at a draft of 295 ft with booms not yet folded out. Boston Whaler, on starboard side, is used to transfer equipment and people.

original profiling system was developed in 1969 and has been extensively upgraded several times. At present, electrical conductivity is sensed, as well as temperature and depth, enabling the estimation of the oceanic salinity and density fields. On a recent cruise, PATCHEX (1986), ten-thousand density profiles were obtained over a three-and-a-half week period.

The profiling system has now been augmented by MPL-developed Doppler sonars. Scattering high-frequency sound off zooplankton in the sea, the sonars are capable of sensing ranges in excess of 1.5 km, with a 1 cm/s precision and a 10 m range resolution. Along with the narrow beam deep-sea sonars, a new generation of fan-beam devices is being developed to scatter from the underside of the sea surface. These devices can measure surface wave propagation as well as lower frequency surface currents with a precision unattainable by conventional means.

The Doppler acoustic work, as well as analogous radar sensing programs, place a premium on the pitch/roll stability of FLIP, rather than the heave response. It does little good to construct narrow beam systems and then mount them on a gyrating platform. Increased tilt stability will be a design objective of the new platform.

Meteorological experiments making use of FLIP exploring

TABLE I
TYPES OF RESEARCH UTILIZING FLIP

Project	*Principal Investigator*	*Project*	*Principal Investigator*
OCEAN ACOUSTICS/UNDERWATER SOUND		PHYSICAL OCEANOGRAPHY	
Phase and amplitude fluctuations	F. H. Fisher	Storm generated waves	W H Munk
Crustal anisotropy	G. G. Shor	Internal waves by thermistor yo-yos	R Pinkel K. Zalkan
Ambient noise	V. C. Anderson F. N. Spiess G. B. Morris R. C. Tyce F. H. Fisher W. S. Hodgkiss J. A Hildebrand	Internal waves by doppler sonar	R Pinkel
		Langmuir circulation by doppler sonar	R. Pinkel J. Smith
		Sea surface slope distribution	R Pinkel
Sea surface noise	V. C. Anderson	Wave direction using FLIP	P. Rudnick
Sound propagation	F. N Spiess J. Northrop G. B. Morris F. H. Fisher N. Booth D. A. Ramsdale W. S. Hodgkiss J. A. Hildebrand	Mixed layer dynamics/air-sea fluxes (MILDEX)	R A Weller
		Langmuir cell, Ekman circulations (MILDEX)	R. A. Weller
		VMCM measurements	R. A. Weller R. Pinkel
		Ocean optics (ODEX)	J. J Simpson
Bottom-bounce propagation	F. H. Fisher	Ocean waves (OWAX)	C. Friehe J. J. Simpson
Coherent recombination of multipaths	W. S. Hodgkiss R. Brienzo	Ocean natural resources	R. Yoder
Attenuation in sediments	R Brienzo	Radar backscatter from waves	(u)
Biological acoustic scattering & taxonomy	P. Greenblatt	Surface wave directional spectra (BOMEX)	R Davis L. Regier
Sound absorption as function of pressure	H. Bezdek	Winding profiling between wave peaks (BOMEX)	(u)
Acoustic backscatter from surface waves	S. McConnell H. Medwin	Air turbulence, MET surface waves (POLE)	R. Davis C. Friehe J. Simpson L. Regier C. Paulson
Point versus planar scattering from density layers	V. C. Anderson G. T. Kaye		
Doppler current meter (10 MHz)	P. Rudnick	Turbulence and microstructure	R. B. Williams
High-frequency (90 kHz) echo sounder	F. Fisher		
Design & development of high-resolution	R. Pinkel		

air–sea interactions have also been an on-going effort, most notably in the Barbados Oceanographic Meteorology Experiment (BOMEX) in the Atlantic Ocean in 1969. For this experiment, wind tunnel tests conducted by Prof. E. Mollo-Christensen at the Massachusetts Institute of Technology showed that the wind profile is altered by less than 1 percent at a distance of 30 m from the centerline. However, as seen in Fig. 3, it was only possible to support the servo-controlled wind profiler (constant height above water) at a distance of about 15 m from the center of FLIP. A larger FLIP would make it possible to extend a hydraulic boom farther away from the hull for sensors requiring minimum flow contamination. Reduced difficulties in holding a given heading during such work, as well as working in rougher weather, will be possible on a larger FLIP.

Other notable air–sea interaction experiments are POLE (1974), MILDEX (1983), GDEX (1984), and PATCHEX (1986). In 1982, Dr. B. Weller of the Woods Hole Oceanographic Institution measured vertical velocities in excess of 15 cm/s in the mixed layer, associated with particularly intense Langmuir cell activity. This was a first sign of the enormous efficiency of Langmuir cells in mixing momentum from the wave zone into the interior of the mixed layer. More detailed studies of the cells themselves occurred in MILDEX. A new experiment, SWAPP (1990), is planned to investigate the interaction of surface waves and Langmuir cells. Multiple laboratories and greater power on a larger FLIP would make it possible to plan extended multi-disciplinary experiments, featuring simultaneous operation of oceanographic and meterological sensors as well as radars.

At this point it is appropriate to emphasize FLIP's utility as a platform from which to test new instruments and develop new observational techniques. As a result of FLIP's extreme economy of operation it is not necessary to convene planning

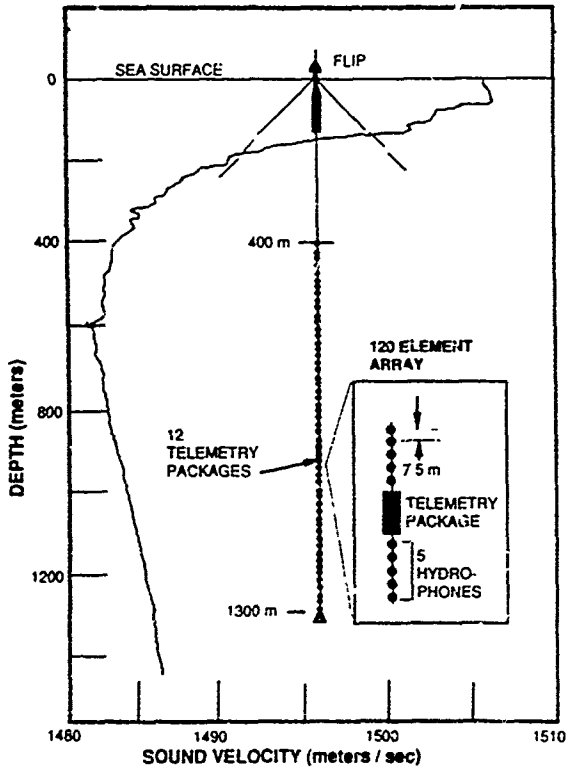

Fig. 2. Schematic of FLIP in three-point moor with vertical array deployed. Sound velocity profile is also shown.

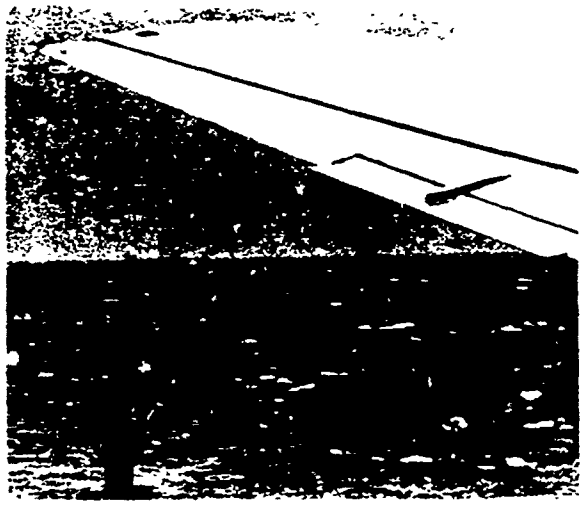

Fig. 3. FLIP in Atlantic Ocean participating in the Barbados Oceanographic Meteorological Experiment (BOMEX). Note vertical servo controlled wave following wind profiling staff.

meetings, coin acronyms, and appoint steering committees to justify funding sufficient to leave the dock. Early evaluation of sonic anemometers and hot-film sensors for meteorology, the vector measuring current meter (VMCM), volume, and surface scattering Doppler sonars were all performed from FLIP. Without this inexpensive source of access to the deep sea, our understanding of the performance limits of these devices would have been more difficult to obtain. A larger FLIP will have increased test capabilities for multiple research groups, thereby facilitating intercomparison experiments.

The ability to moor FLIP in deep water, originally developed to reduce flow and strum noise on hydrophone arrays, has made it possible for Dr. Pinkel to extend Doppler sonar ranges. Prior to this, the range was limited by noise from a hydraulically driven orientation motor to keep FLIP on a constant heading while operating in the drifting mode. In a moor, however, there are such heading variations as weather and current changes which lead to the requirement on a larger FLIP to be able to maintain a constant heading within a few degrees while in a three-point moor.

Some of the operations have included the mooring of FLIP in deep water, 2000 fathoms and deeper, in one-, two- and three-point moors, a technique developed at MPL and refined over the years to become a routine operation [3], [4]. For these moorings, 10 tons of surplus anchor chain and a 750 lb Danforth anchor with specially modified flukes and palms are deployed for each leg of a 1.5-inch-diameter power braid with a scope of about 1.5:1.

Although designed originally for operating in waves of up to 30 ft, it has survived 80 ft blue water swells with a period of 22 s, the null heave response period of FLIP [5]. The peak swells struck FLIP during the night and came to within 2 ft of the upper platform, as shown schematically in Fig. 4. No injuries and only minor damage was incurred during the high waves.

In the most recent operation with a large-aperture vertical array, 120 elements uniformly spaced over 900 m, the acoustic navigation of the array was included through the use of transponders on the bottom which were surveyed in with the GPS satellite navigation system [6]. This involved the same techniques originally developed for the Deep Tow operations at MPL [7]. During a recent operation in June, 1987, with FLIP moored in 2400 fathom water, the watch circle diameter for FLIP in winds of up to 30 knots was only 20 m.

With a crew of five to six and with scientific parties of up to twelve, FLIP is towed to its station since it has no propulsion

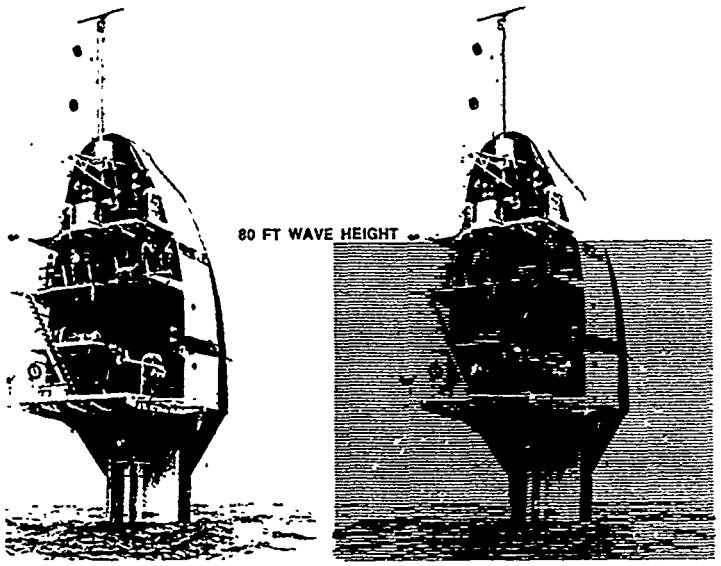

Fig. 4. FLIP in vertical position and with a 80 ft wave superimposed. The high waves came to within 2 ft of the uppermost platform at night. There was minimal damage to FLIP. R. Hasse took movies of waves the following day.

of its own other than a 60 hp orientation motor for the vertical position. With funding support from the U.S. Navy, costs to the user are about $1,400/day exclusive of towing, mooring, and harbor tug costs. For Navy-related research, it is sometimes possible to obtain sea-going tug services from 7,200 hp T-ATF-type fleet tugs such as the USNS *Navajo* and USNS *Narragansett*.

To the greatest extent possible the design of FLIP II will be to keep operating costs within the same range as those quoted above. Because of the larger structure, however, added costs will be incurred. For example, the current cost of a three-point moor (about $23 300) may be larger for FLIP II, whose diameter may be 50 percent greater (30 ft) and whose length may be about 20 percent longer (420 ft) in order to provide the necessary stability and workspace spelled out in the Platform Workshop Report [8].

A brief discussion of mooring FLIP at sea is presented below, along with future plans for mooring FLIP jointly with the Ocean Research Buoy (ORB), also developed at MPL, in order to deploy horizontal and vertical arrays simultaneously in a pseudo-Mills cross to study directional properties of ambient noise.

II. Review of FLIP Development

The need for a stable platform arose from the problem of measuring the effects on long-range sound propagation of horizontal variability in the ocean. At that time, in the late 'fifties, long range meant around 30 nmi. In much the same way that fluctuations in the atmosphere make the stars twinkle (optical scintillation), temperature and salinity fluctuations in the ocean cause acoustic scintillation. If temperature and salinity gradients exist over substantial regions, they will cause bending or refraction of sound waves in the ocean. Just as a stable platform is necessary for a telescope, it was necessary to make use of a stable platform to make similar measurements in the ocean.

Initial attempts were made to do this using the Navy Electronics Laboratory's (NEL) research submarine, USS *Baya* (AGSS-318). Using a 5 kHz sound source at a depth of 300 ft at the convergence zone range of about 30 nmi, hydrophones on the two 50 ft wings of the *Baya* were used to listen to the 5 ms pulses and measure the acoustic fluctuations in phase and amplitude. With the *Baya* at a depth of 300 ft, F. Hale and H. Westphal of NEL (now Naval Ocean Systems Center (NOSC)) showed the author how to find convergence zones where the propagation loss can be as low as 70 dB at 30 nmi and 80 dB at 100 nmi [9].

To measure refraction effects, however, was more difficult. This led to flying 1100 cuft Kytoons from the sound source ships (USS *Rexburg* or USS *Marysville*, also with NEL) at altitudes of 1000 ft, with a 200 W/s xenon flash pulsing at 1 pps. Launching the balloons from the forward gun tub was difficult enough in 25- to 30-knot winds at around 30°N and 120°W. However, to get a good bearing with the scope comparable to the accuracy of our acoustic data proved virtually impossible.

Time for working on our experiment was very limited because this was only one of several on board, which meant that if nothing leaked we might acquire a few minutes of data at best since the submarine had to keep way on for control and the zone was only a nautical mile or so wide. At a depth of 300 ft, for the 5 ms pulse it was possible to separate multipaths so that the direct path, the desired one for measurement, was unambiguously clear.

In January, 1960, I reported my complaints to Dr. F. N. Spiess, Director of the MPL, under whose cognizance I was attempting to do these experiments. He responded immediately by saying that A. Vine of the Woods Hole Oceanographic Institution had long been advocating the upending of a submarine in order to make a stable platform for ocean research. After quickly determining that submarine design didn't really lend itself to operating in a vertical mode, we proceeded to investigate the building of such a platform with the 300-ft depth and a diameter of 20 ft as our contraints (the

depth in order to separate accustic multipaths at ranges of 2000 yd, and the diameter to permit berthing at the NEL pier).

Dr. F. Rudnick showed how to improve the heave response period from 18 s for a cylinder of uniform cross section (same as for a 300 ft pendulum) to 27 s by a 60 percent reduction in the water plane area (12.6 ft diameter), as shown in Fig. 5. Dr. Rudnick's heave calculations were verified with the heave response tests conducted in the Lockheed missile test tank on a 1/25 scale model with an abrupt transition at mid-draft. Subsequent measurements in the ocean showed that the heave response of FLIP agreed with the theory as shown in Fig. 6.

For a spar buoy of constant cross section, the resonant period is given by the pendulum formula in which the draft of the buoy is the length. If one modifies the pendulum formula to account for the reduced area, it can be generalized to the ratio of the total displacement in the vertical to the spring constant of the water plane area

$$T = 2\pi\sqrt{[W/gk]} \qquad (1)$$

where W = displacement in tons, k = spring constant of water plane area (tons/ft), and g = gravitational acceleration (ft/s/s).

Using Rudnick's theory, we selected an area reduction of 60 percent, with the transition to begin above the 150 ft draft for the full-scale FLIP. This gave a period of $T = 27$ s, well away from the spectrum of wave energy in the ocean; the present configuration has a null heave response at 22 s. Using (1), a value of the parameter of W/k equal to or exceeding 591 will keep T at 27 s or greater.

The original configuration of FLIP, after working with the naval architects Rosenblatt and Sons and subsequently with Glosten and Associates, is shown in Figs. 7 and 8. Model tests with 1/100, 1/25, and 1/10 scale models were used to test responses to waves and to work out the transition procedures for going from horizontal to vertical and back. After testing five different hull configurations with the 35 ft sheet metal model in El Capitan Lake (near San Diego), we felt that we knew how to operate a full-sized FLIP.

If the definition of an expert is one who has made all the mistakes that there are to make (and doesn't repeat them), then this is how we acquired our expertise in flipping. The first hull configuration had a D-shaped cross section in the reduced water plane area, the rationale being to provide a straight keel for faster towing. This hull shape turned upside-down during flipping because the center of buoyancy in the reduced cross section was below the center line. A spline-shaped reduced area rolled-over 90°, and a clumsy configuration of 40 controlled rectangular tanks rolled-over nearly 45°. Finally, we went to a simple cylindrical configuration very similar to the configuration shown in Fig. 6, with some ballast in the horizontal keel to insure roll stability during flipping.

The only trouble remaining was plunging. That is, even though the model flipped in the right way, letting the water freely enter the tanks indicated that the full-scale FLIP would plunge 40 ft in going to the vertical. Attempts to throttle the flow in one of the model tanks (Tank 3 of FLIP) resulted in the collapsing of the sheet metal. Finally, with a rather battered model (reinforced by 1 × 1/8 in steel straps) we convinced

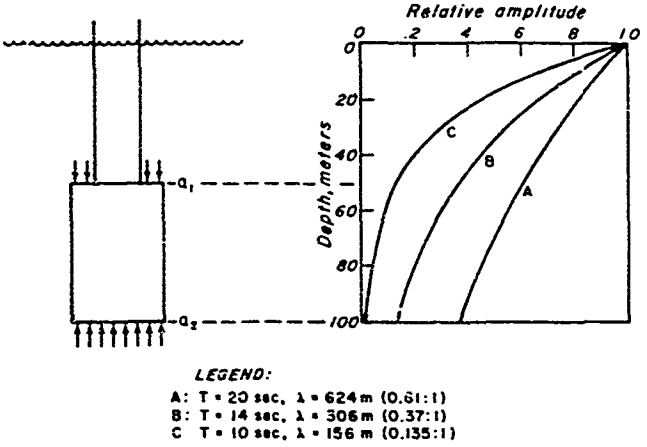

Fig. 5. Schematic showing decay of wave motion with depth for different frequencies in deep water and how corresponding pressure variations affect a spar buoy with area reduction as shown. A large pressure on a small area at depth a_1, will exert a downward force that, at a particular frequency, can be opposed by a smaller pressure on a larger area at depth a_2.

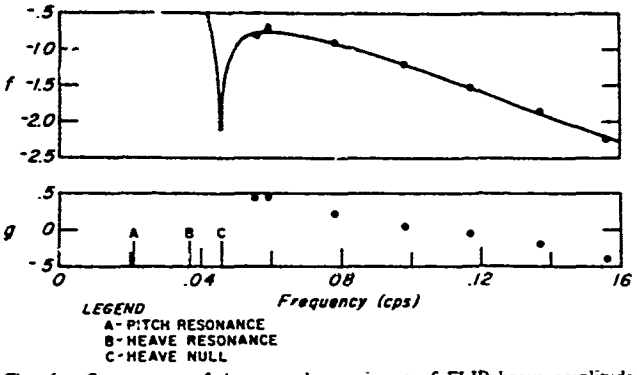

Fig. 6. Comparison of theory and experiment of FLIP heave amplitude response of $f = \log (A_{FLIP}/A_{surface})$ and measured FLIP horizontal amplitude response $g = \log (x_{FLIP}/X_{surface})$.

ourselves that we knew how to do the flipping operation successfully by making Tank 3 a hard tank with a reinforced flat section with small holes between the top and bottom sections (viewed in the horizontal). In this way, we could take on enough water to start going to the vertical and therefore minimize the plunging by throttling the increase of ballast as Tank 3 experienced the increasing differential pressure of up to 90 psi.

All of the testing of the model was documented only on 16 mm film without any technical paper backup. In going through each evolution of hull design, I would report back and confer with Dr. Spiess before going on to the next configuration. At the conclusion of these tests, the battered and rusting model was left in the vertical position at our calibration barge in El Capitan. It eventually rusted through and sank.

Having satisfied ourselves with the flipping procedure and the reduced area configuration, the next step was to come up with plans to be submitted to shipyards for bidding.

It was around this time that I placed the name FLIP on the 1/100 scale model shown in Fig. 9 as a noun and a verb. No better name for it came forth by launching time and we ultimately made the acronym stand for FLoating Instrumentation Platform.

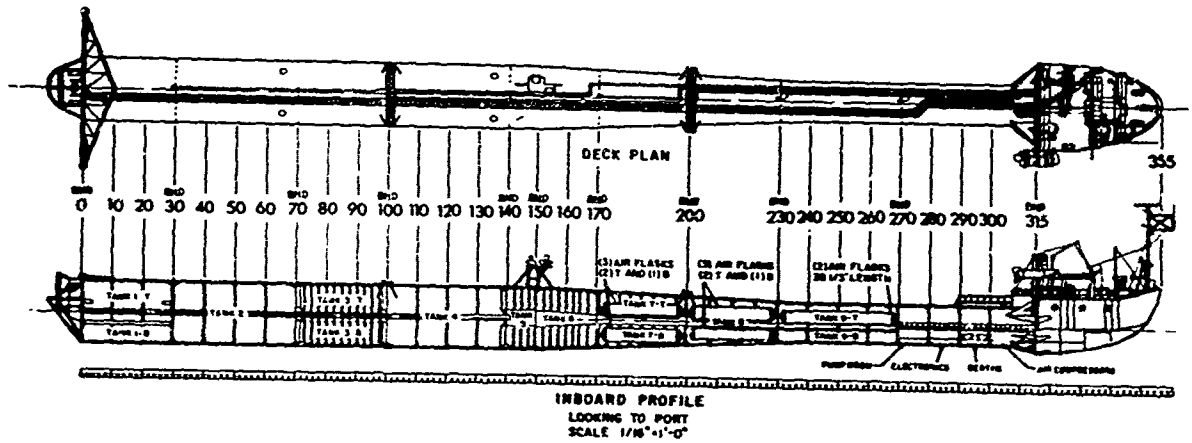

Fig. 7. Schematic of FLIP's hull and tanks.

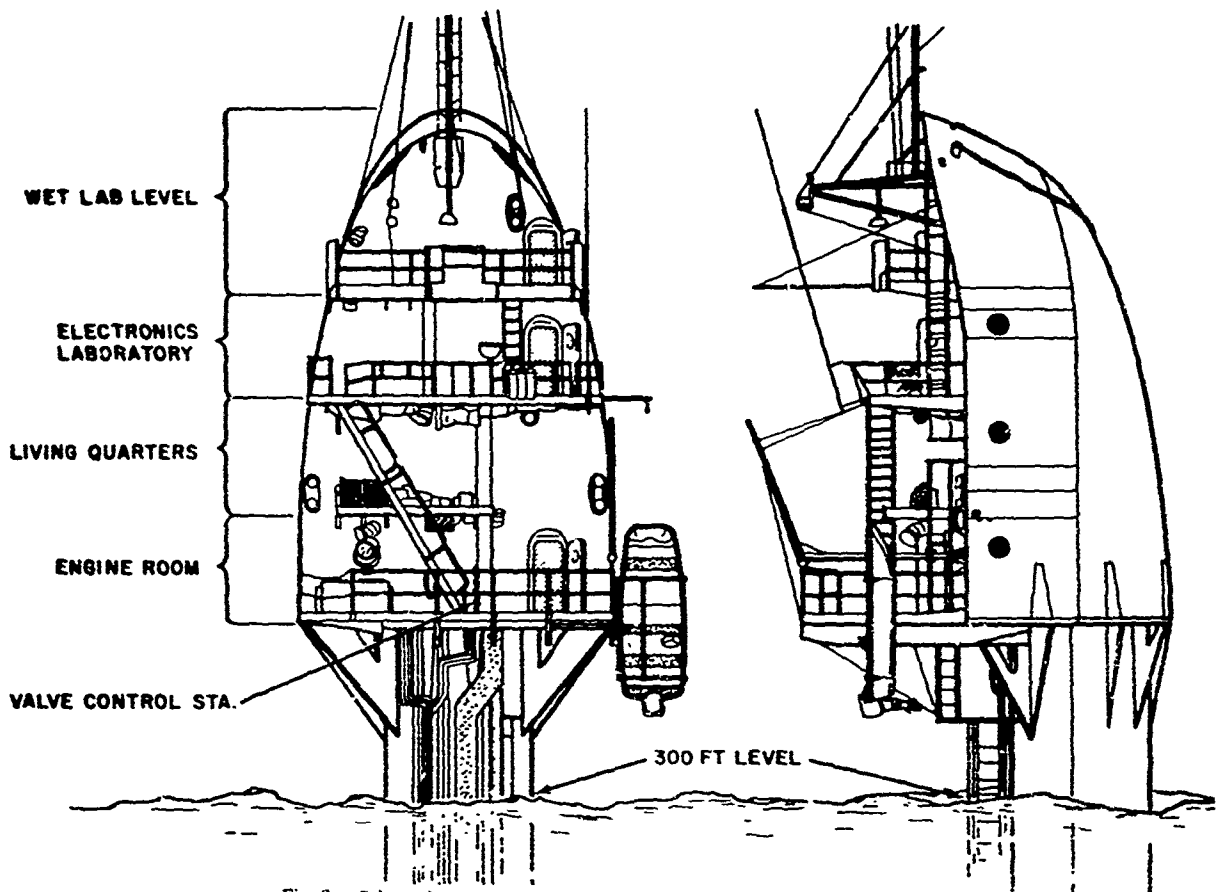

Fig 8. Schematic showing deck arrangements in vertical position with about 500 sq ft per deck.

The living quarters aboard FLIP suffer from the fact that Dr. Spiess and I originally envisioned going to sea aboard the tug that towed FLIP and then transferring to it prior to the flipping and conducting experiments, relying on C rations and cots for our amenities. Our resident inspector, Cdr. E. Bronson, USN (Ret.), at the Gunderson Brothers Engineering Co. where FLIP was built in 1962 was also FLIP's first officer-in-charge and overcame our lack of foresight and imagination regarding living quarters, gradually evolving a way for the crew (5–6 in number) and scientific party (8 members reasonably comfortable, more on occasion) to live aboard FLIP without going stir crazy. Excellent food and the ability to charcoal broil on the patio in sea-state 6 help immensely in making life tolerable aboard FLIP.

Riding aboard FLIP actually saved it on its first major expedition in 1963, when it was to be an island between Hawaii and Alaska for an experiment to measure storm-generated waves from the South Pacific, from a series of island based stations [11]. As it was being towed to a station, 30 to 35 ft waves were encountered and caused a rupture in

what is the engine room deck in the vertical position (due to a design constraint for which I was responsible). Bronson flipped to the vertical and had the rupture welded shut. They were close enough to the station so that they remained in the vertical for the duration of the experiment to measure the small millimeter size waves from the South Pacific storms. From this same experiment, Rudnick [12] showed how the determination of wave direction could be facilitated by using a spar buoy platform such as FLIP.

Air-conditioning and thermal and sound insulation were added after an operation in Hawaii in 1966 in which, at breakfast one morning, my feet, shod in tennis shoes, began to feel as if they were burning. The galley deck, directly above the engine room in which an air cooled 3-71 generator was running, measured 135°F with a thermometer.

For the electronics laboratory we did build a full-scale wooden mock-up in which we had twelve 6-ft-high standard relay racks in four bays. We flipped this mock-up on land to make sure we'd be able to load it in the horizontal and work with it in the vertical. Actually, this was not very visionary because it was colored by the experience of loading 19-in racks aboard submarines. The hatch diameter dictated taking them aboard one at a time, which is how we first loaded FLIP. The possibilities for wiring damage, etc., become nearly infinite in taking apart working equipment on shore and reassembling it on-board FLIP in another orientation. Dr. Rudnick and E. Squier designed portable frames that could hold assembled bays of three 6-ft relay racks as integral units which could be loaded through new hatches to accommodate large gear. These loading frames have wheels on two sides and are rotated before being loaded aboard FLIP and are bolted into position on their sides before going to sea.

The point of the foregoing narrative is to emphasize that Dr. Spiess and I felt that we had a satisfactory, if not optimal, approach to a stable manned platform that in addition to satisfying our immediate acoustic needs would be useful for other scientific projects. By not working out the details regarding living and working aboard FLIP, it made possible an evolutionary and practical approach dictated by the types of operations and the habitability needs.

We now feel that there is a large enough community of users and a large base of experience upon which we can draw to do a better job of designing a FLIP II for research in more inclement conditions where increased capability and habitability are critical. Improved habitability will also be the key in attracting other users who have enjoyed the amenities available on the larger oceanographic vessels. For example, the chief scientist on FLIP shares a four-bunk compartment (with about 12 × 8 × 7 ft dimensions) next to the galley, head, and lounge (a real euphemism), with only thin aluminum partitions separating the compartments. When I go to sea on FLIP I am constantly reminded by my own and my vocal shipmates' experiences about the deficiencies in habitability.

While there already exists a growing community of users and prospective users of FLIP who have an idea of what they would like to do at sea, it is hoped this paper will stimulate further interest and thinking in the design and use of this type of platform.

III. Workshop Recommendations

To get an indication of the FLIP II requirements from those who have used FLIP and from prospective users, the Stable Platform Workshop was sponsored by the Marine Physical Laboratory at the end of June, 1987. The focus of the workshop was to be the consideration of a new, larger, and more capable FLIP for future work. Besides recommendations for a new FLIP, the workshop came up with several additional recommendations for different platforms according to a variety of needs [8].

For those who require a stable platform with a small waterplane area and minimal cross section in the water as well as air, a larger version of FLIP is necessary. Representatives of the marine-oriented disciplines of biological optics, air-sea interactions, marine-air boundary layer studies near the interface and up to the cloud base, surface wave studies, air-sea flux measurements, physical oceanography, acoustics, biology, and submersible operations attended the workshop. *In situ* biological sampling and analysis without the normal large time delays in making port calls can be done on a stable platform such as a larger FLIP with appropriate laboratory facilities. A larger, more habitable FLIP also makes it possible for longer term stations.

A number of very specific requirements were spelled out for FLIP II, mostly focusing on increased stability, greater payloads, more power, low acoustic, electromagnetic, and environmental contamination, greater endurance, and heavy weather operating capability. Requirements unique to particular experiments are shown in part, along with requirements common to many experiments, in Table II. For a more complete treatment, the Platform Workshop Report should be consulted.

None of the requirements has been translated into payload or stability requirements, let alone cost. The present FLIP is limited to about a 12 ton payload and a moment of 264 ft tons. What this means is that we cannot mount two heavy-duty winches on FLIP, each weighing about 6 to 7 tons. As a result of substantial modifications to FLIP since it was launched, the ballast in the horizontal keel has been increased from 70 to 200 tons and we have now reached our limits on improving its capabilities. The addition of weight to the superstructure that remains out of the water in the vertical has reduced its stability in the vertical.

It will take a great deal of planning to come up with a satisfactory FLIP II that can meet a major fraction of the requirements stemming from the workshop. The possibility of providing a deep launch and recovery capability for small submersibles—manned, autonomous, or tethered—has been discussed for some time and was also at the workshop. This capability could be realistic for a FLIP II and would mean that such operations would be less vulnerable to weather. A launch and recovery cradle that would go through the surface on tracks would be required.

Another possibility for improved capability by reducing noise for personnel and experiments is to enclose the generator engines as has been done for the *Alliance*, the new NATO research ship at the SACLANT Undersea Research Center at La Spezia, Italy. In order to find out if the main engines are

TABLE II
REQUIREMENTS FOR A NEW FLIP
(FROM THE PLATFORM WORKSHOP REPORT [REFERENCE 8])

COMMON REQUIREMENTS

1. Greater rough water operating capability: 60 ft waves, weather 100+ ft waves.
2. Reduced tilt response.
3. Increased electrical power to 1000 Kw.
4. Multuple separate laboratory .paces.
5. Weather-proofed platforms and winches.
6. Heavier winches (10 ton+) and booms (vertical and horizontal) above water and booms below the surface for simultaneous multiple sensor and sampler deployments.
7. Continued capability for mooring. singly/jointly.
8. Improved habitability.
9. Safer rough weather personnel/equipment transfers.
10. Environmentally controlled computer space
11. Instrumentation for and access to data for platform motion (pitch, roll, accelerations, heading, position, speed).
12. Stable (minimal roll and pitch), quiet platform with minimal acoustic contamination in water and air
13. Fixed heading keeping ability, drifting mode or in moor.

REQUIREMENTS UNIQUE TO EXPERIMENTS
(Partial listing)

Marine Air Boundary Layer up to Cloud Base

1. Balloon launching area and hanger for tethered balloon (approximately 15 ft long) and/or kytoon. Winch for tethered balloon or kytoon.
2. Helium bottle storage area.
3. Mounting platform for doppler radar (dome up to 3 m diameter) and other remote sensors or accomodations for van housing these instruments.

Near Surface Structure of Marine Air Boundary Layer

1. Vertical tower, reaching up to 50 m above surface. Good access to lower 10 m without being subject to flow distortion (as in BOMEX experiment)
2. Wind tunnel studies (as Mollo-Christensen did for BOMEX).
3. Mounting area, vertical window for acoustic, laser and radar sounders.

Air-Sea Flux Measurements

1. Low aerodynamic drag and weather vaning shape.
2. Surface wave sensing capability.
3. Low radio frequency contamination of radiometric, hot film, and other sensitive instruments.
4. Stability better than present FLIP to permit eddy correlation measurements and other direct measurements such as that of insolation without correcting for platform motion.

running, one literally has to feel the acoustic enclosure to see if it is warm.

IV. Mooring Operations with FLIP/FLIP II

Over a period of nearly twenty years, MPL has developed the capability for placing FLIP into tight three-point moors on a routine basis in 2500 fathom water. The need for transitioning from single-point moors to three-point moors arose from strum and flow noise contamination of acoustic data from hydrophones suspended below FLIP. The mooring operations for FLIP have been discussed in detail by Bronson [3], [4]. With respect to a larger FLIP, one of the desirable characteristics would be its ability to self-moor or to be able to carry enough line so that either more deck space would be available aboard the tug or that a wider variety of ships could be used for towing.

For a tight three-point moor, about 80 tons of gear are loaded aboard the tug that tows FLIP to its station. Each leg of the moor requires three reels of 1.5-in mooring line, each 6000-ft long, a 2000-ft leader of similar line, 10 tons of surplus anchor chain stored in an anchor chain bin, a 750 lb Danforth anchor with augmented flukes and palms, and a shear link assembly to permit recovery of the line but not the chain or anchor. As seen in Fig. 10, where the anchor chain is flaked out on deck, there is not room for much else. By going to anchor chain bins we leave some deck space for other activities, such as towing sound sources and deploying acoustic navigation transponders.

Even with the large Navy tugs there is little room left after all the mooring gear, etc., are lashed down on the fantail. Commercial tugs or mud boats of 5000 hp and at least 185-ft lengths are generally satisfactory. Currently, the possible use of Kevlar mooring lines is being explored to cut down on deck space needs

The possibility of carrying its own mooring lines provides several advantages for a larger FLIP. Single mooring lines without sections joined by shackles would speed-up mooring and recovery times. There would be a substantial decrease on deck loading and space requirements for the tow ship; about 30 tons and around 640 sq ft for the ten reels of 1.5-in nylon line of a 80 000# breaking strength. These lines could be stored in separate tanks without requiring reels. The present nylon lines we use are strong enough so that they could be used to moor a new FLIP of the dimensions discussed here. The only feature required to accomplish this would be to use acoustic command links to release the anchor/anchor chain assembly upon termination of the moor, a requirement that doesn't tax the state of the art. This would make it possible to recover the two downwind legs simultaneously as long as the current and wind are in the same direction so that there would be no danger of fouling.

In general, we now use either a commercial tugboat or, if Navy services are available for Navy projects, we use fleet tugs, T-AFT's operated by the Military Sealift Command. The 7200 hp T-AFT's can tow FLIP as fast as 10–11 knots in calm seas; for rough seas tow speeds as low as 2 knots are required, depending on the FLIP hull stress (monitored on line) and other considerations. A larger hull with a 50-percent

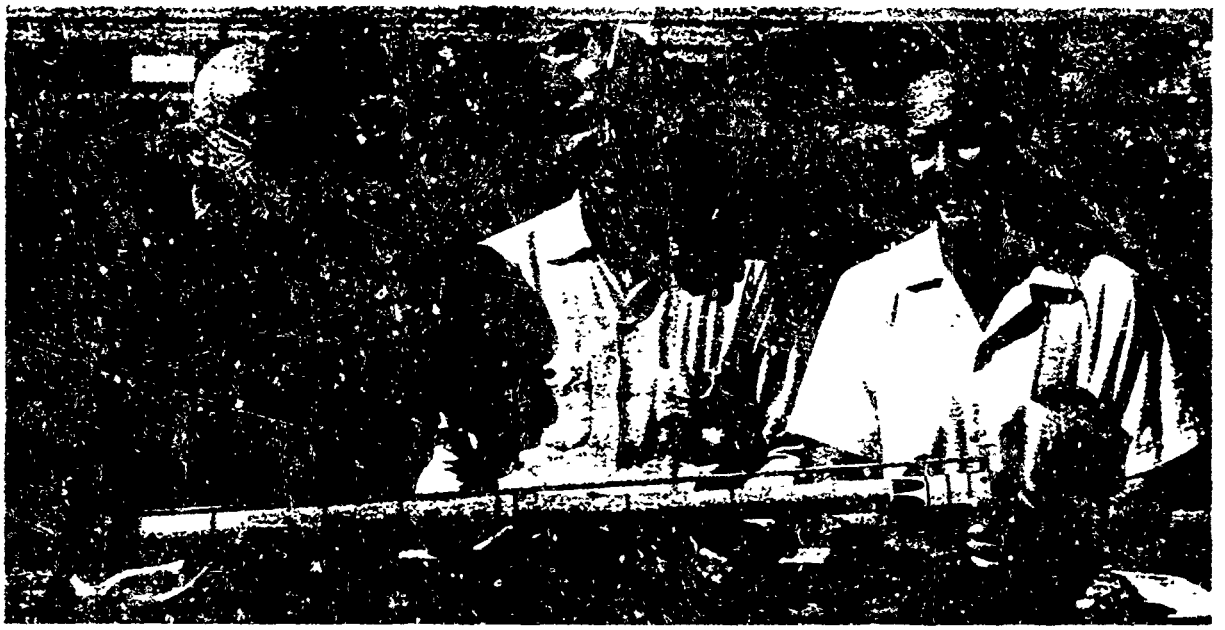

Fig. 9. P. Rudnick, F. H. Fisher, F. N. Spiess, designers of FLIP, holding the first model of FLIP made from a Louisville slugger bat by M. Crouch of MPL.

increase in diameter means that stiffness will be increased by over three times, which in turn means that faster tows in rough seas can be achieved without exceeding stress limits on the hull and that a more comfortable ride for the crew will be possible. The high L/D ratio of 30 to 1 in the narrow section of FLIP means that it shimmies when it is slammed by waves, something that would be reduced greatly with a larger FLIP.

At one time, it was planned to deploy the MPL residual noise horizontal array connected to FLIP using the tugboat to launch the array and the anchor/crown line at the bitter end of the array. This proved to be too difficult to do safely, even in modest seas and with modest winds inside the Southern California bight, let alone out in the open ocean. At Dr. V. Anderson's suggesting a joint mooring of FLIP and ORB, it now seems feasible and safe to deploy the 1500-m-long, 200 element residual noise array horizontally at the sound channel axis depth of about 750 m. The mooring configuration is shown schematically in Fig. 11. The idea would be to tow FLIP and ORB in tandem from the tug and at the experiment site to place FLIP into a three-point moor first. ORB would pay out a tether mooring line to the downwind side of FLIP and either drift downwind to location or use thrusters to maneuver into position. At the proper distance from FLIP, depending on how long a horizontal array is to be deployed and at what depth, the tug would pick up the two mooring lines from ORB, attach the anchors and chains, and complete the five-point moor. A simpler method would be to put FLIP and ORB into independent three-point moors if the tether between them proved troublesome; for example, should traffic go between them.

Once the joint moor is completed, a wire or other messenger from FLIP is used to deploy the horizontal array stored on-board ORB; the array is monitored electrically from the topside electronics on ORB during deployment so that leaks or other defects can be corrected. Weights at both ends of the array are used to provide tension over the array in order to keep it reasonably straight and to keep it below the tether line to prevent fouling. Depth gages in the array as well as acoustic navigation will be used to monitor the position of the array. Real-time data on element position will be incorporated in the array data processing to permit beamforming.

For this type of operation a new and larger FLIP would make it possible to store, deploy, and record both the horizontal and vertical arrays in one location and analyze in real time the data from both through the same system.

With a larger FLIP it may be possible to operate in conjunction with a research ship tethered at varying distances from it. To save on fuel, this was actually done with the R/V *Horizon* during the 1963 expedition for Dr. Munk.

V. Typical Operating Costs

With the support subsidy of FLIP/ORB from NAVSEA, as with the research submarine *Alvin*, the costs to a user are about $1300–1400 per day for either platform. There are officers-in-charge for each platform and four other crewmen; that is, we have one crew and two captains so that only one platform can go to sea at a time unless other temporary help is needed for simultaneous deployment of both platforms.

These costs are in addition to harbor and ocean-going tug services, which vary according to the market. Currently, harbor tugs are about $3500 per operation and ocean tug services can be up to $6000 per day or else be essentially free if the project is a Navy task for which Navy T-ATF's are available. If mooring is required, costs for a three-point moor in deep water is about $23 000, including the cost for 30 tons of anchor chain, three shear link assemblies, amortization of mooring lines, and augmentation of flukes and palms of three 750 lb Danforth anchors. Currently, as mentioned above,

Fig 10. Mooring gear on deck of tugboat. About 80 tons of chain, mooring line, etc , are necessary for a three-point moor in deep water.

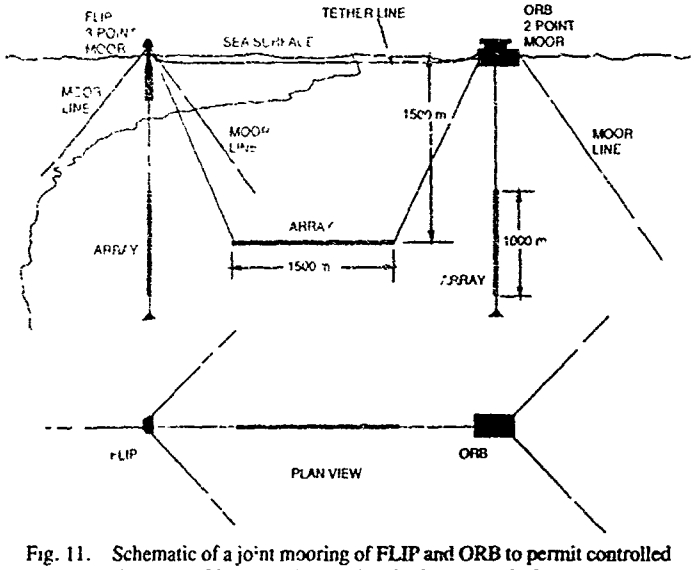

Fig. 11. Schematic of a joint mooring of FLIP and ORB to permit controlled deployment of horizontal array in addition to vertical arrays.

about 80 tons of deck gear must go on the tug in order to do a deep water three-point moor. Costs for other gear aboard the tow ship (winches, cranes, sound sources, etc.) would be in addition to the above.

A larger FLIP might require larger anchors and possibly more chain in order to withstand 1 knot currents and high winds. The underwater cross section would be increased by about 70 percent for the dimensions discussed in the next section. Fortunately, the anchor chain bins and anchors would still not require much deck space aboard the tug, even for the increased load for a new FLIP.

VI. Current Planning

We are focusing our thinking on a new FLIP that could meet the requirements set forth in Table II and which could also be berthed in the same area used for FLIP. With a length of 420 ft and a maximum diameter of 30 ft, it seems that most of the requirements could be met. For operating high-resolution

doppler sonars with a very narrow beam, Dr. Pinkel would like to reduce the tilting motion of FLIP II to about half the motion we experience on FLIP in sea-state 5 and 6.

We are investigating costs and designs for FLIP II in conjunction with Glosten and Associates. As we become more interested in low-frequency acoustic research requiring larger arrays and in doing joint deployments of vertical and horizontal arrays, especially in more inclement conditions, a larger platform becomes necessary. Physical oceanographers have found the stability and size of FLIP to be highly desirable and, for many of the same reasons as for the acoustic community, find that a larger platform is necessary. At this point, therefore, we invite the interest of other scientists and engineers who wish to consider the use of a larger version of FLIP and their submitting comments and suggestions regarding its design.

Acknowledgment

The author is grateful to Dr. F. N. Spiess, Dr. W. S. Hodgkiss, and Dr. R. P. Pinkel for their helpful comments.

References

[1] F. H. Fisher and F. N. Spiess, "FLIP—Floating instrument platform," *J. Acoust. Soc. Amer.*, vol. 35, pp. 1633–1644, 1963.
[2] P. Rudnick, "FLIP—An oceanographic buoy," *Science*, vol. 146, pp. 1268–1273, 1964.
[3] E. D. Bronson, "Three-point anchoring in the deep ocean," *Proc. US Naval Inst.*, vol. 101, pp. 101–103, 1975.
[4] E. D. Bronson, "Deep anchoring FLIP," *Mar. Tech. Soc. J.*, vol. 3, pp. 42–44, 1971.
[5] P. Rudnick and R. W. Hasse, "Extreme Pacific waves," *J. Geophys. Res.*, vol. 76, pp. 742–744, 1971.
[6] B. Sotirin and J. A. Hildebrand, "Large aperture digital acoustic array," *IEEE J. Oceanic Eng.*, this issue, pp. 271–281.
[7] F. N. Spiess, M. S. Loughridge, M. S. McGehee, and D. E. Boegeman, "An acoustic transponder system," *J. Inst. Navigation*, vol. 13, pp. 154–161, 1966.
[8] C. B. Bishop and F. H. Fisher, "Stable research platform workshop," Marine Phys. Lab., Scripps Inst. Ocean., San Diego, CA, SIO Rep 87-29, 1988.
[9] F. E. Hale, "Long-range propagation in the deep ocean," *J. Acoust. Soc. Amer.*, vol. 33, pp. 456–464, 1961
[10] P. Rudnick, "Motion of a large spar buoy in sea waves," *J. Ship Res.*, vol. 11, pp. 257–267, 1967.
[11] F. E. Snodgrass *et al.*, "Propagation of swell across the Pacific," *Phil. Trans. Roy. Soc. London*, vol. A259, pp. 431–497, 1966.
[12] P. Rudnick, "Wave directions from a large spar buoy," *J. Mar. Res.*, vol. 27, pp. 7–23, 1969.

★

Frederick H. Fisher (SM'70) obtained the B.S. and Ph.D. degrees in physics from the University of Washington, Seattle, in 1949 and 1957, respectively, and also was a midshipman at the U.S. Naval Academy, Annapolis, MD, from 1945 to 1947.

He is a Research Oceanographer and Deputy Director at the Marine Physical Laboratory (MPL), Scripps Institution of Oceanography, University of California, San Diego. After arriving at MPL in 1955 to do his thesis for the University of Washington, he has been there continuously except for a postdoctoral stint at the Acoustics Research Laboratory at Harvard University, 1957–1958, and a year at the University of Rhode Island, 1970–1971, where he was Professor and Chairman of the Physics Department. His scientific interests center around acoustics in the ocean, including propagation and ambient noise as well as the physical chemistry of chemical sound absorption, especially at high pressure.

He is a Fellow and former President of the Acoustical Society of America and currently serves as one of its representatives on the Governing Board of the American Institute of Physics. He is the current editor of the IEEE JOURNAL OF OCEANIC ENGINEERING.

ONR/MPL GENERAL DISTRIBUTION LIST

Chief of Naval Research
Department of the Navy
Arlington, Virginia 22217-5000
Code 12, 122(2), 125
1121, 112, 1122,
1123, 1125, 1125 OA,
1125 GG, 23

ONRDET
Stennis Space Center
Bay St Louis, Mississippi 39529-5004
Code 125

Commander
Naval Sea Systems Command
Washington, D. C. 20362
Code 63DB, 933A

Commanding Officer
Naval Ocean Research and
Development Activity
Stennis Space Center
Bay, St. Louis, Mississippi 39529-5004
Code 100, 110, 300, 330,
200, 220, 240, 250, 270,
320, 360, 350

Commander
U.S. Naval Oceanographic Office
NSTL Station
Bay St. Louis, Mississippi 39522-5004
Atten: Bill Jobst

Assistant Secretary of the Navy
(Research Engineering & Systems)
Department of the Navy
Washington, D. C. 20350

Defense Advanced Res Proj Agency
TTO - Tactical Technology Office
1400 Wilson Boulevard
Arlington, Virginia 22209-2308
Atten: John N. Entzminger

National Oceanic & Atmospheric
Administration
Ocean Engineering Office
6001 Executive Boulevard
Rockville, Maryland 20852

Commander
Space and Naval Warfare
Systems Command
Washington, D. C. 20360-5100
Code PMW-180T, PMW-180-5

Commander
Naval Ship Res. & Dev. Center
Bethesda, Maryland 20084

Executive Secretary
Naval Studies Board
National Academy of Sciences
2101 Constitution Avenue, N.W.
Washington, D.C. 20418

Director
Strategic Systems Proj Ofc.
Department of the Navy
Washington, D. C. 20361
Code NSP-20

Commander
Naval Ocean Systems Center
San Diego, California 92152
Code 00, 01, 16, 94,
54, 541, 605, 71, 72, 701

Commander
Submarine Development Group ONE
139 Sylvester Road
San Diego, California 92106

Commanding Officer
Civil Engineering Laboratory
Naval Construction Battalion Center
Port Hueneme, California 93043
Code L40, L42

Commanding Officer
Naval Underwater Systems Center
Newport, Rhode Island 20844
Atten E L Sullivan

Officer in Charge
Naval Underwater Systems Center
New London Laboratory
New London, Connecticut 06320
Code 900, 905, 910, 930, 960

Director of Research
US Naval Research Laboratory
Washington, D. C. 20375
Code 2620, 2627, 5000, 5100, 5800

Officer in Charge
Naval Surface Warfare Center
10901 New Hampshire Avenue
White Oak Laboratory Detachment
Silver Spring, Maryland 20903-5000
Attn E232 Tech Library

Commanding Officer
Naval Coastal Systems Laboratory
Panama City, Florida 32401

STOIAC
Battelle Columbus Laboratories
505 King Avenue
Columbus, Ohio 43201

Commander
Naval Air Systems Command
Washington, D. C. 20361
Code 370

Commanding Officer
US Naval Air Development Center
Attention: Bruce Steinberg
Warminister, Pennsylvania 18974

Director
Defense Documentation Center
(TIMA), Cameron Station
5010 Duke Street
Alexandria, Virginia 22314

Institute for Defense Analyses
1801 North Beaugard Street
Arlington, Virginia 22311

Superintendent
US. Naval Postgraduate School
Monterey, California 93940

Chief Scientist
Navy Underwater Sound Reference Div.
US. Naval Research Laboratory
P O. Box 8337
Orlando, Florida 32806

Supreme Allied Commander
U.S. Atlantic Fleet
ASW Research Center, APO
New York, New York 09019
Via: ONR 100 M, CNO OP092D1,
Secretariat of Military,
Information Control, Comm Stee

Director
Institute of Marine Science
University of Alaska
Fairbanks, Alaska 99701

Director
Applied Physics Laboratory
Johns Hopkins University
Johns Hopkins Road
Laurel, Maryland 20810
Atten J R. Austin

Director
College of Engineering
Department of Ocean Engineering
Florida Atlantic University
Boca Raton, Florida 33431

Director
Marine Research Laboratories
c/o Marine Studies Center
University of Wisconsin
Madison, Wisconsin 53706

Director
Applied Research Laboratory
Pennsylvania State University
P.O. Box 30
State College, Pennsylvania 16802

Director
Applied Physics Laboratory
University of Washington
1013 NE 40th Street
Seattle, Washington 98195

Director
The Univ. of Texas at Austin
Applied Research Laboratory
P.O. Box 8029
Austin, Texas 78712

Director
Lamont-Doherty Geological Observatory
Torrey Cliff
Palisades, New York 10964

Director
Woods Hole Oceanographic Institution
Woods Hole, Massachusetts 02543

Director
Inst. of Ocean Science Engineering
Catholic University of America
Washington, D.C. 20017

National Science Foundation
Ocean Sciences Division
Washington, D C. 20550

Office of Naval Research
Resident Representative
c/o Univ. of California, San Diego
Mail Code Q023
La Jolla, California 92093

University of California, San Diego
Marine Physical Laboratory
Branch Office
La Jolla, California 92093